AFRPL-TR-72-88

AD 748415

NUMERICAL ANALYSIS OF NONLINEAR LONGITUDINAL COMBUSTION INSTABILITY IN METALIZED PROPELLANT SOLID ROCKET MOTORS

VOLUME I: ANALYSIS AND RESULTS

by

Jay N. Levine and F. E. C. Culick

TECHNICAL REPORT, AFRPL-TR-72-88
JULY 1972

ULTRASYSTEMS, INC.
FORMERLY DYNAMIC SCIENCE
2400 Michelson Drive
Irvine, California 92664

D D C
RECEIVED
SEP 21 1972
B

"APPROVED FOR PUBLIC RELEASE; DISTRIBUTION UNLIMITED."

Reproduced by
NATIONAL TECHNICAL
INFORMATION SERVICE
U S Department of Commerce
Springfield VA 22151

AIR FORCE ROCKET PROPULSION LABORATORY
UNITED STATES AIR FORCE
EDWARDS, CALIFORNIA

ACCESSION for
NTIS White Section ☑
DDC Buff Section ☐
UNANNOUNCED ☐
JUSTIFICATION
BY
DISTRIBUTION/AVAILABILITY CODES
Dist. AVAIL. and/or SPECIAL
A

"When U. S. Government drawings, specifications, or other data are used for any purpose other than a definitely related Government procurement operation, the Government thereby incurs no responsibility nor any obligation whatsoever, and the fact that the Government may have formulated, furnished, or in any way supplied the said drawings, specifications or other data, is not to be regarded by implication or otherwise, or in any manner licensing the holder or any other person or corporation, or conveying any rights or permission to manufacture, use, or sell any patented invention that may in any way be related thereto."

UNCLASSIFIED

Security Classification

DOCUMENT CONTROL DATA - R & D

(Security classification of title, body of abstract and indexing annotation must be entered when the overall report is classified)

1. ORIGINATING ACTIVITY *(Corporate author)* Ultrasystems, Inc. (Formerly Dynamic Science) 2400 Michelson Drive Irvine, California 92664	2a. REPORT SECURITY CLASSIFICATION Unclassified 2b. GROUP

3. REPORT TITLE

NUMERICAL ANALYSIS OF NONLINEAR LONGITUDINAL COMBUSTION INSTABILITY IN METALIZED PROPELLANT SOLID ROCKET MOTORS
VOLUME I: ANALYSIS AND RESULTS; VOLUME II: COMPUTER PROGRAM USER'S MANUAL

4. DESCRIPTIVE NOTES *(Type of report and inclusive dates)*

5. AUTHOR(S) *(First name, middle initial, last name)*

Jay N. Levine
F. E. C. Culick

6. REPORT DATE July 1972	7a. TOTAL NO. OF PAGES 255	7b. NO. OF REFS 70
8a. CONTRACT OR GRANT NO. F04611-71-C-0060 b. PROJECT NO. 5730 c. d.	9a. ORIGINATOR'S REPORT NUMBER(S) Technical Report AFRPL-TR-72-88 9b. OTHER REPORT NO(S) *(Any other numbers that may be assigned this report)*	

10. DISTRIBUTION STATEMENT

"Approved for public release; distribution unlimited."

11. SUPPLEMENTARY NOTES	12. SPONSORING MILITARY ACTIVITY Edwards Air Force Base Edwards, California

13. ABSTRACT

The primary objective of the current effort was the development and solution of a nonlinear analytical longitudinal instability model, which would allow all of the various governing phenomena to be accounted for in a coupled manner. The two primary elements of the current instability analysis are a method of characteristics solution of the two phase flow in the combustion chamber of the motor, and a coupled calculation of a transient burning rate. The transient burning rate analysis presented, herein, is a unique and interesting development. It is based on an extension of the most popular, linear, harmonic combustion response model. The current method allows the calculation of propellant burning response to a pressure disturbance of arbitrary waveform, for all time, including the period immediately following the initiation of the disturbance. The analysis also includes a model for velocity coupled response. Therefore, for the first time, the nonlinear effects of velocity coupling on the growth of pressure waves in a combustion chamber can be computed.

The instability solution, itself, begins with the calculation of the steady state two-phase flow in the motor. The flow in the combustion chamber is calculated by numerically integrating the equations of motion. The nozzle flow is found using the constant fractional lag approximation. The steady state conditions are then perturbed and the subsequent wave motion in the motor is calculated numerically, using the method of characteristics. The nature of the engine response is dependent upon the interaction the various gain and loss mechanisms in the engine, which are, in turn, a function of the propellant burning response, the size and amount of particulate matter present, the magnitude and shape of the initial disturbance and the geometrical configuration of the motor.

The instability model is currently subject to the following limitations. Only motors with cylindrically perforated grain were considered. The gasdynamic flow was assumed to be one-dimensional and the particles in the gas stream were taken to be of uniform size and inert. The nozzle flow is assumed to be quasi-steady.

A series of instability solutions have been calculated, wherein some of the main parameters such as particle size, burning rate constants, and initial disturbance waveform and magnitude have been varied, in an attempt to qualitatively assess the behavior and validity of the present model. From all appearances, the behavior of the model is quite realistic and limited comparisons with data have been quite encouraging.

DD FORM 1 NOV 65 1473

UNCLASSIFIED

Security Classification

14. KEY WORDS	LINK A ROLE	LINK A WT	LINK B ROLE	LINK B WT	LINK C ROLE	LINK C WT
Combustion instability						
Solid propellant combustion						
Nonlinear						
Metalized propellant						
Two phase flow						
Velocity coupling						
Transient burning rate						
Oscillatory burning						

NUMERICAL ANALYSIS OF NONLINEAR LONGITUDINAL COMBUSTION INSTABILITY IN METALIZED PROPELLANT SOLID ROCKET MOTORS

VOLUME I: ANALYSIS AND RESULTS

TECHNICAL REPORT, AFRPL-TR-72-88
JULY 1972

Prepared by: Jay N. Levine
F. E. C. Culick

ULTRASYSTEMS, INC.
FORMERLY DYNAMIC SCIENCE
2400 Michelson Drive
Irvine, California 92664

"APPROVED FOR PUBLIC RELEASE; DISTRIBUTION UNLIMITED."

AIR FORCE ROCKET PROPULSION LABORATORY
UNITED STATES AIR FORCE
EDWARDS, CALIFORNIA

ic

FOREWORD

The present report is part of a two volume set which describes a nonlinear solid rocket motor instability analysis and computer program. Volume I contains the analytical basis for the computer program and a discussion of the results obtained to date: Volume II of the set describes the computer program and serves as a user's manual.

This investigation is entitled NUMERICAL ANALYSIS OF NONLINEAR LONGITUDINAL COMBUSTION INSTABILITY IN METALIZED PROPELLANT SOLID ROCKET MOTORS. The two volumes are additionally subtitled as follows:

Volume I - Analysis and Results

Volume II - Computer Program User's Manual

This investigation was sponsored by the

Air Force Rocket Propulsion Laboratory
Director of Laboratories
Edwards, California 93523
Air Force Systems Command, United States Air Force

under contract number F04611-71-C-0060 with Robert J. Schoner as technical monitor. Jay N. Levine of Ultrasystems (formerly Dynamic Science) was program manager.

This technical report has been reviewed and is approved.

Paul J. Daily, Lt. Col. USAF
Chief, Technology Division

TABLE OF CONTENTS

		Page No.
	FOREWORD	iii
	ABSTRACT	iv
	NOMENCLATURE	vi
1.	INTRODUCTION	1-1
2.	BACKGROUND AND SURVEY OF EXISTING EXPERIMENTAL AND ANALYTICAL RESULTS	2-1
	2.1 Finite Amplitude Waves in a Closed Resonant Tube	2-1
	2.2 Experimental Results for Longitudinal Waves in Solid Propellant Rocket Motors	2-6
	2.3 Analytical Work on Longitudinal Instabilities	2-13
	2.4 Nonlinear Analyses of Instabilities in Liquid Rocket Motors	2-16
3.	EQUATIONS OF MOTION	3-1
	3.1 Discussion of the Mathematical Model	3-1
	3.2 Conservation Equations	3-3
	3.3 Nondimensional Equations	3-6
	3.4 Characteristic Equations	3-8
4.	RESPONSE FUNCTION FOR TRANSIENT BURNING	4-1
	4.1 Linear Response to Harmonic Pressure Oscillations	4-1
	4.2 Linear Response to an Arbitrary Change of Pressure	4-11
	4.3 Velocity Coupled Response	4-16
5.	BOUNDARY CONDITIONS	5-1
	5.1 Head End - $x = 0$	5-1
	5.2 End of the Grain - $x = 1$	5-1
6.	INITIAL CONDITIONS--STEADY STATE SOLUTION	6-1
	6.1 Steady State Equations in Conservation Form	6-1
	6.2 Nondimensional Equations	6-2

TABLE OF CONTENTS (Continued)

		Page No.
7.	NUMERICAL SOLUTION	7-1
	7.1 Method of Characteristics	7-1
	7.2 Interpolation	7-16
	7.3 Transient Burning Rate Analysis	7-18
	7.4 Steady State Solution	7-26
8.	ANALYSIS OF LINEAR STABILITY	8-1
	8.1 Numerical Example	8-11
9.	NUMERICAL RESULTS	9-1
	9.1 Waves in a Closed End Tube	9-2
	9.2 Effect of Burning Rate Parameters--A and B	9-3
	9.3 Effect of Initial Disturbance Wave Form	9-9
	9.4 Effect of Particle Size	9-13
	9.5 Effect of Initial Disturbance Amplitude and Drag Law	9-15
	9.6 Velocity Coupling	9-18
10.	SUMMARY AND CONCLUSIONS	10-1
	10.1 Summary and Conclusions	10-1
	10.2 Recommendations for Future Work	10-4
11.	REFERENCES	11-1
	APPENDIX A. THE TRANSIENT BURNING RESPONSE--SOME SPECIAL CASES	A-1

ABSTRACT

The primary objective of the current effort was the development and solution of a nonlinear analytical longitudinal instability model, which would allow all of the various governing phenomena to be accounted for in a coupled manner. The two primary elements of the current instability analysis are a method of characteristics solution of the two phase flow in the combustion chamber of the motor, and a coupled calculation of a transient burning rate. The transient burning rate analysis presented, herein, is a unique and interesting development. It is based on an extension of the most popular, linear, harmonic combustion response model. The current method allows the calculation of propellant burning response to a pressure disturbance of arbitrary waveform, for all time, including the period immediately following the initiation of the disturbance. The analysis also includes a model for velocity coupled response. Therefore, for the first time, the nonlinear effects of velocity coupling on the growth of pressure waves in a combustion chamber can be computed.

The instability solution, itself, begins with the calculation of the steady state two-phase flow in the motor. The flow in the combustion chamber is calculated by numerically integrating the equations of motion. The nozzle flow is found using the constant fractional lag approximation. The steady state conditions are then perturbed and the subsequent wave motion in the motor is calculated numerically, using the method of characteristics. The nature of the engine response is dependent upon the interaction the various gain and loss mechanisms in the engine, which are, in turn, a function of the propellant burning response, the size and amount of particulate matter present, the magnitude and shape of the initial disturbance and the geometrical configuration of the motor.

The instability model is currently subject to the following limitations. Only motors with cylindrically perforated grain were considered. The gas-dynamic flow was assumed to be one-dimensional and the particles in the gas stream were taken to be of uniform size and inert. The nozzle flow is assumed to be quasi-steady.

A series of instability solutions have been calculated, wherein some of the main parameters such as particle size, burning rate constants, and initial disturbance waveform and magnitude have been varied, in an attempt to qualitatively assess the behavior and validity of the present model. From all appearances, the behavior of the model is quite realistic and limited comparisons with data have been quite encouraging.

NOMENCLATURE

A	-	burning rate parameter, Eq. (4-14)
A_b	-	admittance function
A_n	-	nozzle admittance function
a	-	gas only, sound speed
a_F	-	sound speed based on P_F and T_F
B	-	burning rate parameter, Eq. (4-32) also, fractional lag parameter, Eq. (5-6)
B_v	-	burning rate parameter for velocity coupling
C	-	ratio of solid to gas specific heats, C_s/C_p
$\tilde{C}$	-	constant in steady state burning rate, Eq. (3-5)
C_D	-	particle drag coefficient
C_k	-	erosive burning constant, Eq. (3-5)
C_m	-	see β_1
C_p	-	specific heat of gas at constant pressure
C_s	-	specific heat of solid particles
C_v	-	specific heat of gas at constant volume
C_1, C_2, C_3, C_4	-	defined in Eq. (7-34)
D_p	-	port diameter
E	-	normalized surface activation energy, $E_w/R_o\overline{T}_w$ also, integral defined by Eq. (8-16)
E_w	-	activation energy of surface reaction
e	-	internal energy
F_p	-	particle-gas interaction force per unit volume, Eq. (3-8)
f	-	frequency also, as defined by Eq. (8-14)
G	-	defined by Eq. (7-8)
g	-	defined by Eq. (6-17)
H	-	defined by Eq. (4-20)
h	-	enthalpy
h_{11}	-	defined by Eq. (8-12)
K	-	fractional lag constant, Eq. (5-3)
K'	-	chamber fractional lag constant, Eq.(7-44)
k	-	thermal conductivity, also complex wave number

k_s	-	thermal conductivity of the solid particles
L	-	length of the grain, also fractional lag constant, Eq. (5-4)
L'	-	chamber fractional lag constant, Eq. (7-44)
ℓ	-	perimeter of the grain
M	-	Mach number, also number of points on initial line
M_b	-	Mach number at burning surface
m	-	particle mass, also surface mass flux
Nu	-	Nusselt number
n	-	pressure exponent in steady state burning rate
n_v	-	constant in velocity coupled analysis, Eq. (4-75)
n_w	-	exponent of pressure dependence of surface reaction rate
P	-	pressure
P_{ref}	-	reference pressure in steady state burning rate
P_F	-	chamber pressure
Pr	-	Prandtl number
p	-	pressure, also used for Laplace transform variable
p_{11}	-	defined by Equation (8-10)
Q_f	-	heat release per unit mass
Q_p	-	particle-gas heat transfer rate per unit volume, Eq. (3-14)
Q_w	-	heat of reaction for processes at burning surface
q	-	see γ
R	-	gas constant, also normalized throat radius of curvature
R_o	-	universal gas constant
R_b	-	response function, Eq. (4-35)
Re	-	Reynolds number based on particle diameter and particle-gas relative velocity
RHS	-	right hand side of a characteristics compatibility relation
r	-	linear burning rate
S_b	-	area of burning surface
s	-	dimensionless Laplace transform variable, $= i\kappa\omega/\bar{r}^2$
T	-	temperature
T_F	-	adiabatic flame temperature
t	-	time
t_c	-	defined by Eq. (7-33)
u	-	axial velocity
u_t	-	threshold velocity
W	-	defined by Equation (4-28)

w	-	reaction rate divided by gas density
x	-	axial distance
α	-	growth constant
α_p	-	particle damping constant
$\hat{\alpha}_p$	-	defined in Eq. (8-35)
β_1	-	particle to gas weight flow ratio
β_2	-	ratio of particle to gas mass burning rates, w_p/w
γ	-	ratio of gas specific heats, C_p/C_v
δ	-	a small increment in time
δ'	-	equal to $t_c\delta$
ϵ_1, ϵ_2	-	convergence criteria for characteristics calculations, also used in velocity coupling analysis (Eq. 4-72)
κ_s	-	thermal diffusivity of the propellant
Λ	-	defined by Eq. (4-27)
λ	-	complex function of frequency, Eq. (4-8)
μ	-	viscosity
ξ_s	-	equals $\bar{r}x/\kappa_s$
ρ	-	density
ρ_F	-	density based on P_F and T_F
ρ_m	-	density of the metal oxide particles
ρ_s	-	density of the solid propellant
σ	-	particle radius
σ_1, σ_2	-	defined by Eq. (4-62)
τ	-	nondimensional time, $\bar{r}^2 t/4\kappa_s$, also used in Section 2 to denote period of oscillation
τ_v	-	characteristic relaxation time for particle velocity, Eq. (3-1)
τ_T	-	characteristic relaxation time for particle temperature, Eq. (3-1)
Φ	-	defined by Eq. (5-10)
φ	-	phase angle
Ω	-	nondimensional frequency, Eq. (4-9)
ω	-	mass burning rate, per unit length, per unit cross-sectional area, Eq. (3-4); also occasionally used for angular frequency

Subscripts

e	-	end of the propellant grain
f	-	flame
g	-	gas
ℓ	-	for the ℓth mode of oscillation
p	-	particle
o	-	initial or stagnation value
t	-	at the nozzle throat
w	-	at the burning surface of the propellant

Superscripts

$(\ )^*$	-	in Sections 3, 5 and 6 only, denotes a dimensional variable
$(\ )'$	-	denotes fluctuation
$\bar{(\ )}$	-	in Section 4 denotes steady state variable, in Section 5 denotes an "equivalent" gas value, in Section 7 denotes an average quantity
$(\ )^+$	-	pertaining to a right running characteristic
$(\ )^-$	-	pertaining to a left running characteristic
$(\ )^{(r)}$	-	real part of

1. INTRODUCTION

Solid propellant rocket motors are often subject to chamber pressure oscillation during the course of their firing. The existence of these fluctuations is indicative of the existence of a coupling mechanism, or mechanisms, between the combustion at the surface of the propellant and the gasdynamic flow in the chamber. When the rate at which energy is supplied to the flow, by this coupling, exceeds the rate at which energy is lost through the various dissipative mechanisms that exist, the chamber pressure oscillations are amplified. They may grow to such amplitudes that the oscillating acceleration of the vehicle may produce failure of the equipment or even failure of the motor.

Of the various unstable motions observed in solid propellant rocket chambers, longitudinal combustion instability is currently the most troublesome. The axial, or longitudinal, mode of combustion instability occurs in the frequency range intermediate between the very low frequencies of bulk, or L*, instabilities, and the high frequencies associated with the tangential, or transverse, instability modes. Unlike transverse mode instabilities, which are very often eliminated by the addition of powdered aluminum to propellant formulations; the existence of a remedy of comparable simplicity for longitudinal instabilities has not yet been demonstrated.

Efforts to deal with the problem of longitudinal instability, most logically, have begun with experimental, and analytical, investigations designed to shed light on the governing physical phenomena. Both laboratory scale experiments, and full scale firings, have identified the existence of numerous, complex, mostly nonlinear, processes which actively play a role in determining the stability characteristics of a rocket motor. As a result of this complexity, investigators attempting to predict these disturbances have, in the past, been almost universally forced to linearize the equations governing the various phenomena. Attempts to solve more realistic nonlinear models have been made, but, only by focusing on one of the many processes at a time. In view of this, the primary objective of this program was the development and solution of a nonlinear analytical model for describing longitudinal mode instability, which would allow all the various processes to be accounted for in a coupled manner. A second

analyses of the burning rate response to harmonic disturbances. The formulation of the boundary and initial conditions for the problem is discussed in Sections 5 and 6. The numerical methods employed in solving the governing equations are discussed in Section 7; while in Section 8, a linear stability analysis is developed, for the purpose of comparison with the nonlinear numerical results.

Time has limited the number of instability solutions which could be obtained during the course of the present investigation. However, as shown in Section 9, the calculated results are quite interesting, and exhibit all the proper qualitative trends. The nonlinear analysis described herein appears to have the potential to lead the way to greater understanding of longitudinal combustion instability, and to the realization of more accurate quantitative predictive capability.

A further discussion of the conclusions that can be drawn from the present study may be found in Section 10. At the end of the report, in Appendix A, the behavior of the transient burning rate model is examined for some special cases.

2. BACKGROUND AND SURVEY OF EXISTING EXPERIMENTAL AND ANALYTICAL RESULTS

2.1 Finite Amplitude Waves in a Closed Resonant Tube

The problem of acoustic waves in a closed tube is of course a very old one. Only those recent works concerned with finite amplitudes are cited here. In simplest form, the experimental apparatus consists of a rigid tube closed at one end and fitted with a piston at the other. All reported experimental results, and all but one of the analyses give information only about the waves after limiting amplitude has been reached.

A periodic motion can be excited in the tube at any frequency, but the most interesting behavior occurs when the piston oscillates with a frequency at or near one of the resonant frequencies of the tube. It has long been known (see Ref. 1 and other works cited there) that as the amplitude is increased, the wave motion in the tube changes from a simple sinusoidal motion in both space and time, into one having both a continuous and a discontinuous part. At sufficiently high amplitude, one or more weak shock waves propagate to and fro. The appearance of weak "discontinuities" is a consequence of the nonlinear convective effects and the dependence of the speed of sound on temperature.

Analyses of the steady wave motion as a weak shock embedded in a continuous periodic motion have been given by Saenger and Hudson (Ref. 1) and Betchov (Ref. 2). Subsequently, Chester (Ref. 3) discussed in more detail the relative importance of the mechanisms involved and produced a single solution valid over a range of frequencies near resonance. He showed, in agreement with Betchov, that the effects of heat conduction and viscous forces provide small corrections to the inviscid solution but are not required to limit the amplitude of the motion.

In Ref. 4, Coppens and Sanders analyzed the motion in terms of the generation of harmonics. Their results are not carried far enough, explicitly, to apply to a discontinuity. They also quote measurements which, as do other experimental observations, show an important feature, namely the appearance of harmonic distortion of the waverform at quite modest amplitudes. For example, when the amplitude of the fundamental mode is approximately one percent of the ambient pressure, the amplitude of the second

harmonic is already fifteen percent of the amplitude of the first harmonic. A discontinuity is apparent when the amplitude is one-tenth of the ambient pressure. This is a general result for acoustic waves in resonant tubes--nonlinear behavior is obvious at these low amplitudes.

On the other hand, in solid propellant motors, quite clean sinusoidal motions, with very little harmonic content, are often observed to amplitudes as high as 20% or more of the average pressure. The explanation for this has not been definitely established, although it must evidently rest on the behavior of the combustion processes.

The stability of wave motions in a rocket motor is a primary problem. It is then necessary to examine the transient growth of waves from some specified initial disturbance. The corresponding problem for waves in a resonant tube has been treated in only one work, Ref. 5. Perhaps the main reason for this is that the situation arises only for a self-excited oscillating system, and hence is not of interest when waves are driven by external means. The computation of Ref. 5 does not include the influence of combustion or mean flow, and hence shows only the transient development of the weak discontinuity. Numerical results were reported for a finite-difference calculation and for the method of characteristics.

As an aid to interpreting later results for the behavior of nonlinear waves in a motor, it is useful to sketch an idealization of the motions in a resonant tube. Measurements of pressure are usually made at the end of a chamber, but it is also interesting to see the distribution of pressure along the chamber as it varies in time. Three cases will be examine: a purely sinusoidal oscillation at the fundamental frequency, a weak shock, and the sum of these two. These are shown in Figures 2-1 to 2-3, with the distribution of pressure shown for every eighth cycle. The position of the shock wave relative to the sinusoidal oscillation has been chosen such that it arrives at one end just as the sinusoidal pressure at that end is a maximum. This will not in general be true in actual cases, owing to the influence of energy losses, average flow and, of course, strongly nonlinear effects. Also, for the example shown here, the shock is assumed to be sufficiently weak that it propagates always at constant speed equal to the sound speed for the standing wave; the period of both motions is T.

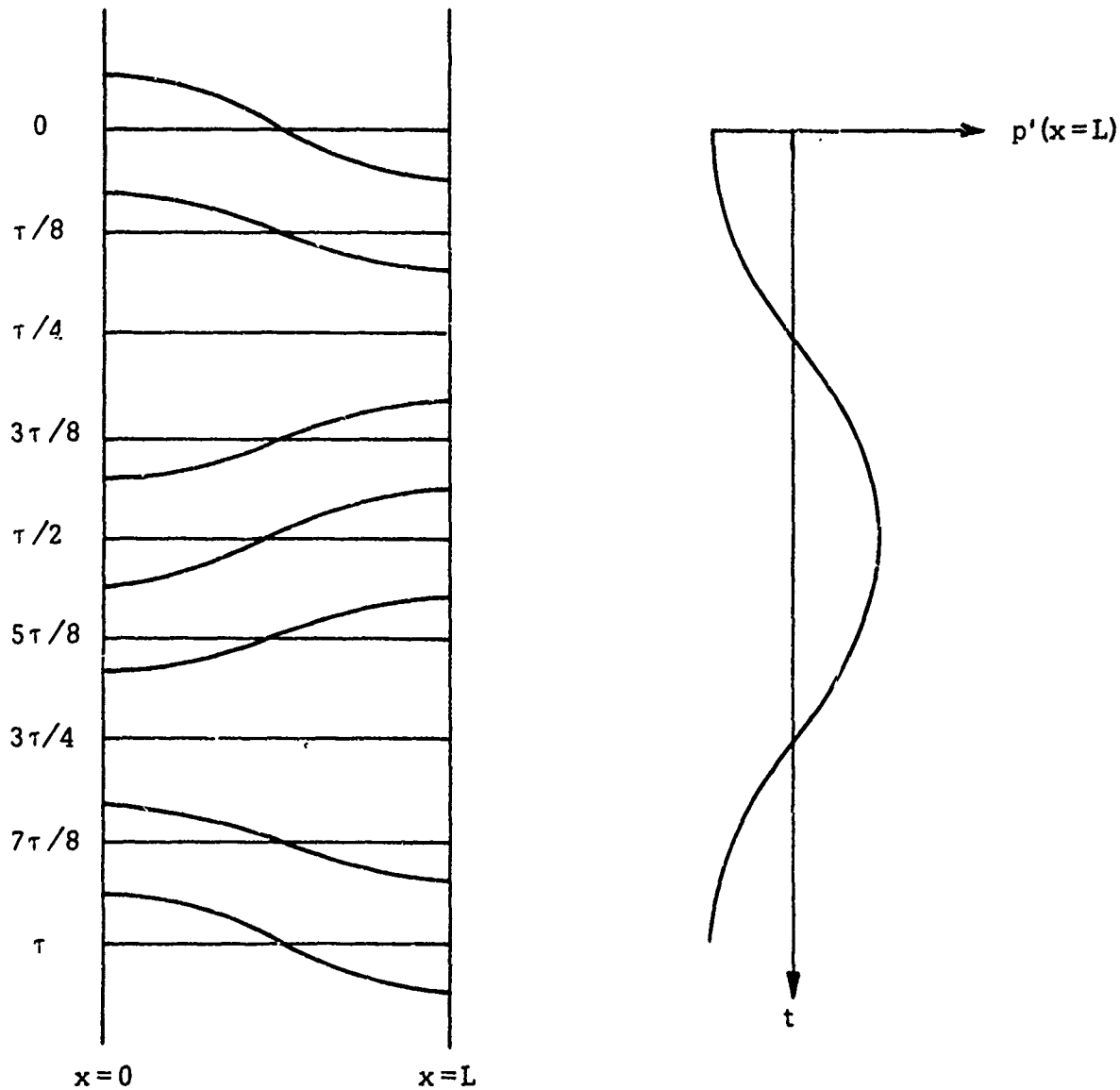

Figure 2-1. Distribution of Pressure Along the Chamber and Pressure at x = L for a Sinusoidal Standing Wave

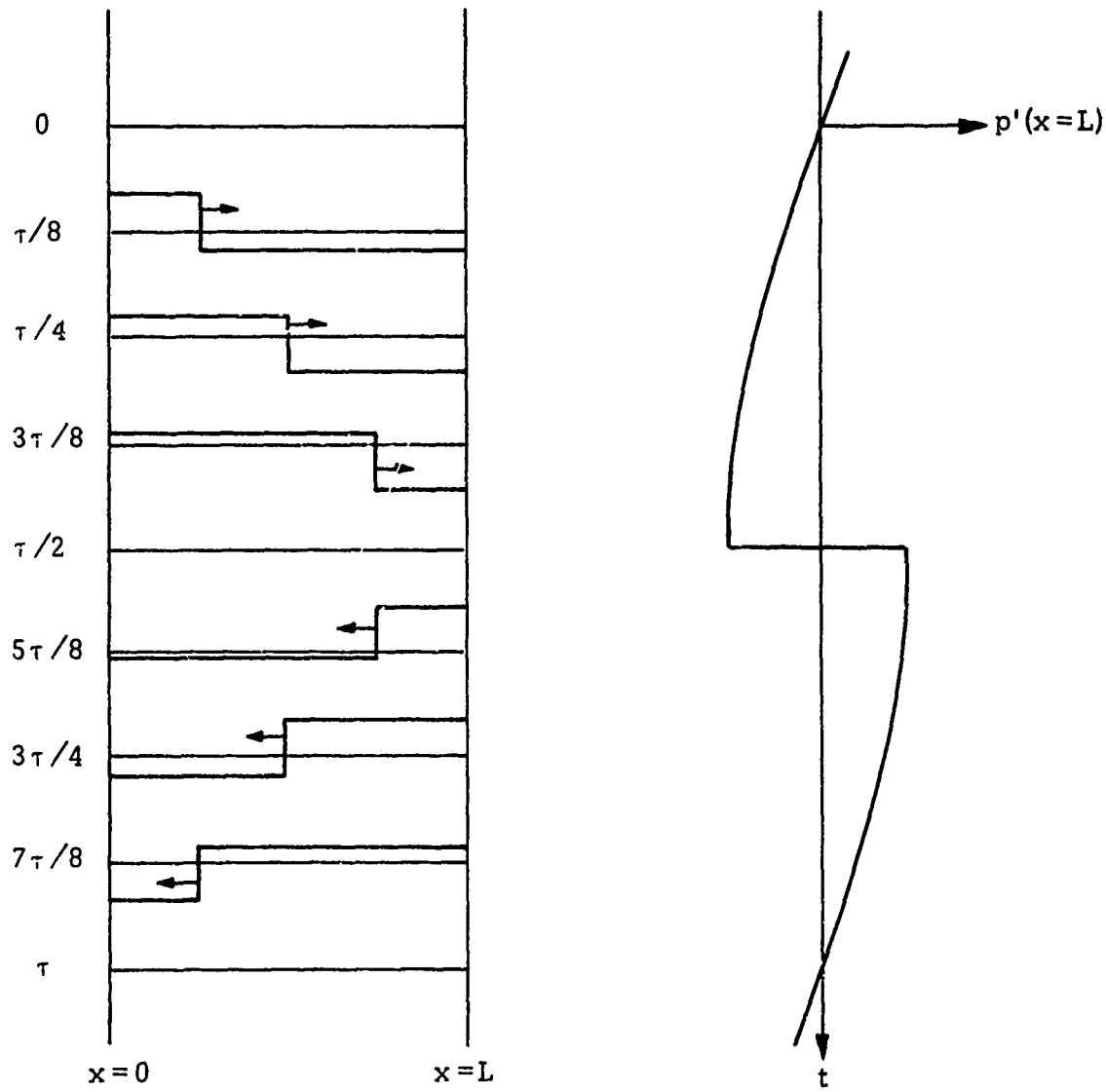

Figure 2-2. Distribution of Pressure Along the Chamber and Pressure at x = L for a Weak Travelling Shock Wave

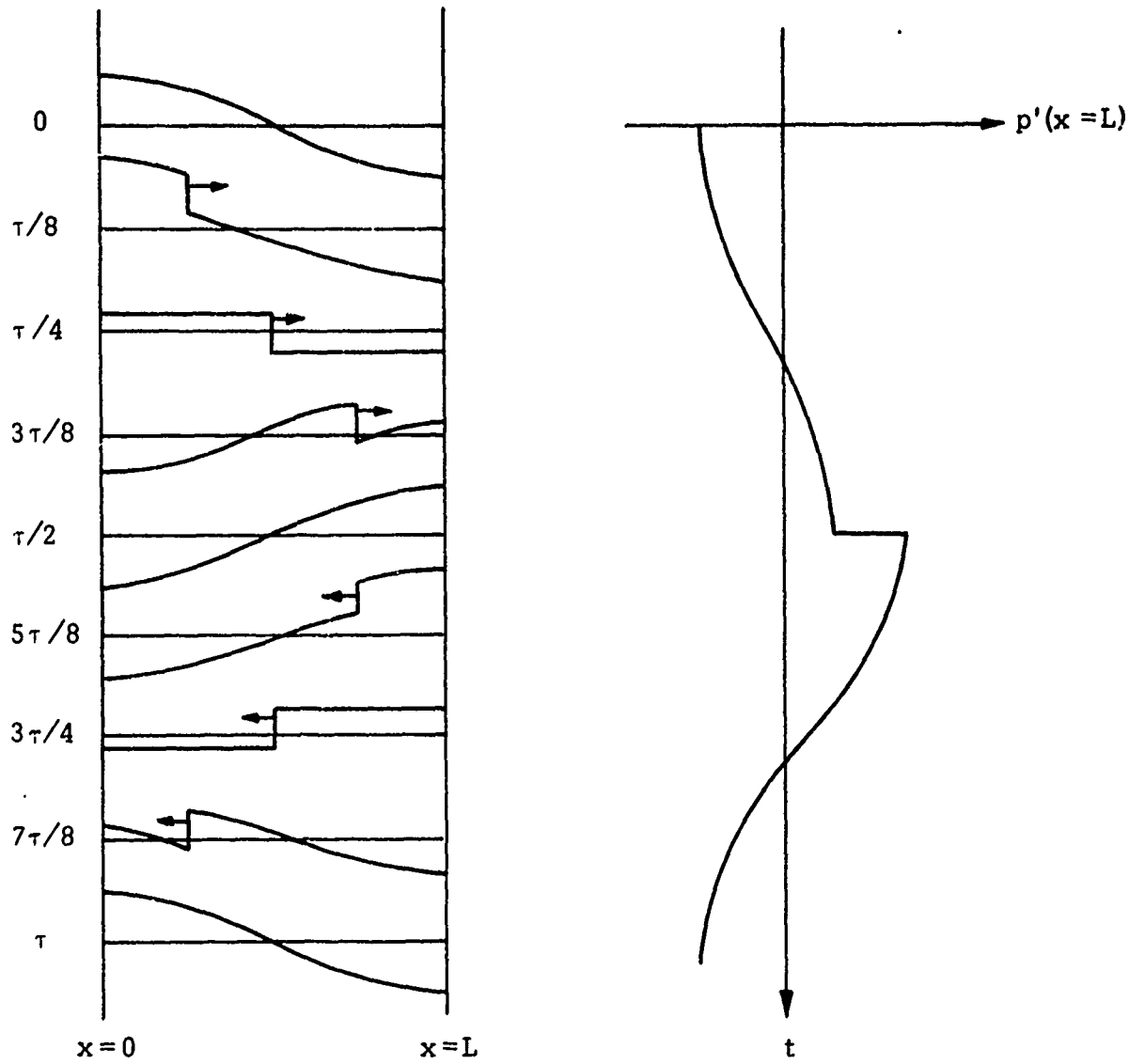

Figure 2-3. Distribution of Pressure Along the Chamber and Pressure at x = L for a standing wave with a weak travelling shock wave

Note that if the standing wave is weak, so the motion is dominated by a travelling shock wave, the pressure measured at one end appears roughly as a sawtooth or triangular wave. In time, the pressure jumps abruptly, and then decays until it jumps again upon the next arrival of the shock. Many of the pressure traces reported in the work at CARDE and SRI, discussed below, exhibit, qualitatively, this kind of behavior. Even for the case of nonlinear motions in a simple resonant tube, the pressures measured differ from the form shown here, owing to contributions from many harmonics.

It is clear that previous work on the classical problem of waves in a resonant tube provides background, but no useful results for the problem of transient waves in a rocket motor.

2.2 Experimental Results for Longitudinal Waves in Solid Propellant Rocket Motors

Longitudinal instabilities arise spontaneously in full-scale motors--a number of examples exist, but few have been reported in the open literature. The most recent reports of such observations appear in Refs. 6-8. Most of the data which are available for motors have been taken in laboratory devices, and almost all involve pulsing.

It is possible to produce sharp fronts propagating in a tube by introducing an impulse of mass, momentum, or energy. This may be done, for example, with an electric spark or a small explosive charge. If the tube contains only an inert gas, the subsequent motions are not particularly interesting--they die. For a rocket motor, however, introducing a pulse during a firing is a useful--indeed, the only--means for determining completely the stability characteristics. The combustion processes constitute a source of energy; the amplitude of the pulse may grow, remain unchanged, or decay. Whatever happens must, of course, reflect the nonlinear conflict between the gain and loss of energy for the pulse.

Qualification of liquid rocket motors by pulsing has been a standard procedure for some time. Although the technique has, for practical purposes essentially not been used for solid propellant motors (an exception is program for developing motors used in the Canadian "Black Brant" vehicle, cited in Ref. 17), there exists a substantial amount of laboratory data for instability studies using T-burners as well as burners with cylindrical configurations. Only results for end-vented burners will be discussed here.

It should be noted that in laboratory tests, the strength of the pulse can be controlled, although precision is a problem. Thus, it is possible to produce perturbations much larger than one would normally encounter in an actual motor, as, for example, might occur due to partial blockage of the nozzle by a small piece of material. Laboratory tests therefore offer more flexibility, and by proper interpretation should be applicable to real motors.

A significant amount of experimental data has been taken at the Canadian Armament and Research Institute (CARDE) (see Refs. 9-18) and at the Stanford Research Institute (Refs. 19-22). More recently, work on small pulsed motors has been done at the Aerojet-General Solid Propulsion Company (Ref. 23). Limited results on spontaneous longitudinal oscillations have been obtained at the Naval Weapons Center (Ref. 24), for a center-vented configuration. A few observations were reported earlier by Hercules, Inc. (Ref. 25) and by the Ballistics Research Laboratory (Ref. 26).

2.2.1 Data Taken at CARDE and SRI

In both the CARDE and SRI work, pulses were introduced at the head end of a motor by introducing small explosive charges. Apart from a few important visual observations (Refs. 13, 15 and 16) the data consists of pressure measurements taken at the head and aft ends of the chamber. Rectangular, slotted, star, and other cross-sections have been used, but most of the tests have been made with circular ports. Experimental variables which have been studied include chamber diameter and length (hence frequency), throat/port area ratio (hence chamber pressure and Mach number), initial temperature, and composition of the propellants. The last involved ballistic additives and aluminum content as well as changes of binder and size and type of oxidizer.

Pressure traces suggest the presence of one or more discrete finite pressure waves propagating up and down the chamber. (See Figures 1-3 and following remarks). Subsequently, optical observations (Refs. 13, 15, and 16) established that indeed the instability involved a weak shock wave, usually travelling with Mach number less than 1.2. It is evident from the experimental results that the disturbance introduced by the explosive charge very rapidly settles to the nearly planar wave travelling to and fro in the chamber. The strength is a function of position in the chamber, mainly because of the losses incurred upon reflection at the ends, particularly at the nozzle. The influence of the mean flow was more pronounced during travel from the nozzle to the head end; the wave front was then concave in the direction of propagation.

The wave motion therefore appears to be analogous to the case of the classical resonant tube driven at high amplitude, an idealized example of which is shown above in Figures 2-1 to 2-3. However, in a motor, there are obviously strong perturbations due to the combustion and related processes. That the instability is often predominantly a discrete travelling wave (in some cases two waves are present) is probably related to the pulsing, but insufficient information is given in the accounts to draw any conclusions. In the CARDE work, the explosive charges used were 0.3 gm to 12 gm depending on the size of the motor. No further details are given.

Moreover, only portions of a few records are reproduced and all show the discrete waves very shortly after the pulse. It is not possible to deduce any information about growth or decay rates of the waves. Indeed, in the latest work reported (Ref. 18), only time averaged pressures were recorded.

The experimental results therefore relate to the qualitative question of whether a pulse is stable or unstable, although in a few cases the limiting amplitudes are given. The severity of the instability is interpreted usually in terms of the shift of mean pressure.

In the motors used, progressive burning causes the mean pressure to rise during a firing; testing the stability characteristics consists of introducing a sequence of pulses which therefore occur at successively higher pressures. Typically, pulses early in a firing, at lower mean pressures, may be stable, while those at the higher pressures late in the firing may produce the travelling wave instability. (It is of course possible that in some cases all pulses may be stable or all unstable). Since there is generally an increase of the mean pressure when the pulses are unstable, there are some delicate questions involved in determining a stability boundary with any precision. How this has been done in the work cited (especially Refs. 13 and 18) will not be discussed here; it is thoroughly discussed in those references).

The behavior of the mean pressure during a firing in which an unstable pulse is initiated is sketched in Figure 2-4

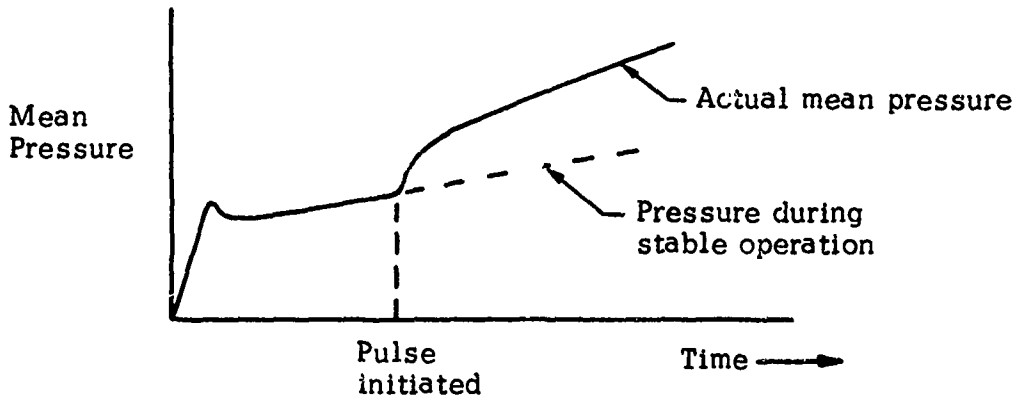

Figure 2-4. Mean Pressure for a Typical Firing from the CARDE and SRI Work

If no pulse is introduced, the firing is normally stable; thus the data truly relates to a problem of nonlinear instability. Much of the interpretation of data is based on plots of mean chamber pressure, measured at a fixed fraction of web burned, versus K , the ratio of burning surface to throat area. An example is shown in Figure 2-5; such data can be obtained, for example, from a series of firings identical except for the initial value of throat to port area ratio.

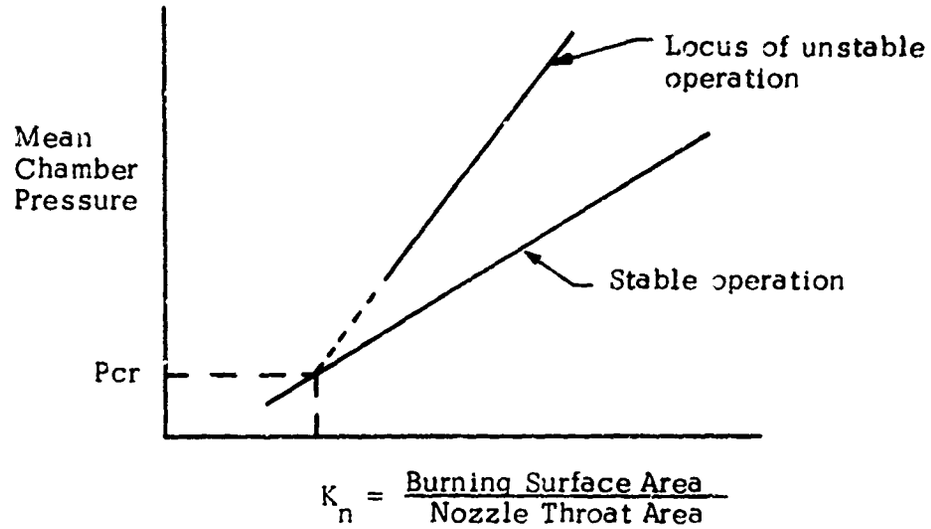

Figure 2-5. Sketch of Stable and Unstable Operating Pressures for a Fixed Fraction of Web Consumed

The intersection of the two lines in Figure 2-5 gives "critical" or "threshold" values of pressure and K_n.

Early work seemed to suggest that the dynamical characteristics of many propellants could be correlated in terms of the threshold values of pressure and K_n (Refs. 10,12 and 21). However, subsequently (Ref. 18) it was established that not only was this correlation severely limited by the motor configuration, but also that by no means all propellants could be characterized by the same stability boundary. Even worse, in many cases the stable and unstable lines shown in Figure 5 had slopes so nearly alike that a well-defined threshold point could not be established. As a result of the last conclusion, Roberts and Brownlee (Ref. 18) were forced to interpret their data in a different way. They chose to use the difference of the mean pressures for stable and unstable operation, taken at some arbitrary value of the stable value (1200 psia).

It is therefore not possible at the present time to discuss this data in the context of analysis. Obviously there is a great amount of information contained in the experimental results. The qualitative trends have been discussed thoroughly in Reference 18, but it seems worthwhile including here a brief summary of the main conclusions.

(i) For a given propellant and grain geometry, there is always an operating pressure above which finite disturbances are unstable. This has been found true for all propellants tested by both SRI and CARDE. It should be noted that theoretically the effects of the mean flow, and hence Mach number, are important to the question of stability. No attempt has been made, apparently to correlate data with this parameter, or to determine its influence. The proper strategy is by no means obvious at the present time.

(ii) Although the time-averaged pressure increases with time (see Figure 4) the amplitude of the wave (change of pressure divided by the mean pressure) measured at the head end remains essentially constant. The amplitude is also insensitive to the ratio of port-to-throat area, and K_n. Thus, there appears to be a limit cycle determined largely by the processes occurring during propagation.

(iii) Tests in motors geometrically scaled from lengths of 20 inches to 80 inches show that the larger motors remain nonlinearly stable to higher operating pressures. The design of the nozzle has very little influence. Increases to larger sizes (180 inches) showed only a small further change in the minimum stable operating pressure.

(iv) For a given propellant and grain cross-section, motors having "low" values of length to port diameter (and hence higher frequencies for the longitudinal mode) tend to be more stable. "Low" here means about five or less. At larger values, there seems to have been relatively little influence on the unstable waves. Whether or not his behavior is closely related to the frequency response of the propellants is not known.

(v) Changing the grain cross-section has essentially no influence if K_n is fixed. In other words, the waves really are close to being one-dimensional.

(vi) Very roughly, propellants having high burning rates tend to have higher threshold pressures. Put another way, it appears that if all variables including the mean pressure are fixed, an increase in burning rate (as, for example, by adding rate modifier or ballistic additive) is a stabilizing influence. This is contrary to much of the evidence for linear stability.

(vii) Addition of lithium fluoride which reduced the burning rate of an aluminized propellant greatly reduced the threshold pressure and in fact produced "extremely violent instability at practicable K_n levels" (Ref. 13).

(viii) It is difficult to generalize about the influence of aluminum (Ref. 18). However, it certainly is true that the addition of aluminum is by no means a guaranteed stabilizing influence and may very well aggravate a problem. This has been noted also in other works (Refs. 24 and 25, for example).

In summary, the data reported in these works is related directly to nonlinear stability. However, since there is no information concerning the growth and decay rates of pulses, the measurements cannot be treated quantitatively within the analysis presently available or covered in the work reported here.

2.2.2 Other Experimental Results

The early observations reported in References 25 and 26 contain insufficient detailed information to permit quantitative interpretation. One of the main conclusions of Reference 25, however, is of considerable practical interest, and is consistent with (viii) above: The addition of aluminum may cause a stable motor to become unstable in the longitudinal mode.

Although the observations discussed briefly in Ref. 24 were taken in a center-vented configuration, which will not be treated in the analysis discussed here, the data are important for at least two reasons. First, the unstable motions arise spontaneously, and second they exhibit very distinct nonlinear behavior.

The more recent measurements taken by Micheli (Ref. 23) are potentially very useful. These comprise approximately two dozen firings of tubular motors having a fundamental frequency of about 800 Hz for the longitudinal mode. The motors were pulsed, but spontaneous instabilities were also observed. Detailed records are available, but unfortunately the data have not been reduced from the raw state. It is particularly important that growth and decay rates can be found from the records. The instabilities appear to be mainly standing waves.

The same propellant (ANB3066) was used in all tests. As a result of current efforts in several laboratories, the dynamical characteristics should be quite well known in the near future. One interesting conclusion, based on a comparison of two firings, is that, as Brownlee has reported, an increase of mean pressure seems to be a destabilizing influence. Linear analysis (Section 8) shows that the major reason for this behavior is the decrease of the Mach number of the mean flow, and hence a decrease in the losses at the aft end, as the mean pressure is increased. Some of the numerical examples presented later in the present work have been based on these pulsed-motor firings.

2.3 Analytical Work on Longitudinal Instabilities

The numerical analysis discussed in the present report is, in an essential way, a new contribution to understanding the problem of nonlinear instabilities in solid propellant rocket motors. That is, in no previous work have the gas dynamical nonlinearities been taken into account in a computation of transient wave motions. In this section, what has previously been done is briefly summarized.

Available analytical works which are relevant here may be conveniently divided into two classes: those which are concerned primarily with the problem in solid propellant rockets, and those which are concerned with other kinds of nonlinear wave motions mainly in liquid rocket motors. None treat the problem in the detailed quantitative manner discussed here. On the other hand, they may provide certain results more easily and economically than an elaborate numerical calculation.

A very special feature of the longitudinal instability in solid propellant rocket motors is that there are necessarily substantial fluctuations of the gas velocity parallel to the burning surface. The combustion processes are surely sensitive to these unsteady motions, a phenomenon called "velocity coupling." There must also be fluctuations of pressure, to which the combustion processes will respond, producing "pressure coupling." Pressure coupling must always be present under unsteady conditions, but velocity coupling need not be, as, for example, in purely radial modes in a cylindrical chamber, or in an end-burner oscillating in a longitudinal mode.

Consequently, much of the work concerned with longitudinal instabilities in solid propellant rockets has been directed to characteristics and possible effects of velocity coupling. (Refs. 27-31). A fundamental characteristic of velocity coupling is that it is intrinsically nonlinear. This is a consequence of the fact that the combustion processes respond to the magnitude but not the direction of velocity fluctuations, thereby introducing rectification effects. This idea has been discussed in considerable detail in the works referred to. The stability of motions and the possible generation of harmonics have been discussed. But growth of waves to a limiting amplitude, and the nonlinear effects within the volume of the chamber have not been studied. It should be noted that since the nonlinearity associated with velocity coupling is of first order in the amplitude, while the gas dynamical nonlinearities are of second order (and higher) the nonlinear influence of the velocity coupling should be significant at relatively lower amplitudes. It is not presently possible to establish this conclusion definitively.

Two qualitative consequences of nonlinear velocity coupling are that higher harmonics should be generated and that an increase of mean chamber pressure may be produced. Both features are evident in some of the data.

The connection is appealing but cannot at this time be supported quantitatively. The major problem in doing so is that the coupling cannot be described quantitatively. Particularly in Reference 30, and in subsequent unpublished work, one may find speculations and estimates, but all conclusions remain tentative. However, nonlinearities and the mean flow in the chamber are ignored.

In Reference 22, the group at SRI attempted to interpret their data in terms of a model for the coupling between a small-amplitude pressure disturbance and the combustion processes at the surface. Certain aspects of the gas dynamics in the chamber (but not the mean flow) are discussed qualitatively and to some extent quantitatively. This work was based on the idea that the instability observed is a shock wave sustained by mass addition at the boundary, which in turn is related to a response function for pressure coupling only. They supposed that the response function had to have a certain arbitrarily chosen minimum value in order that the wave exhibit sustained periodic motion. They then examined the values of parameters appearing in their formulation of the response function to determine what values were required to match some observed stability data.

Although those results appeared at the time to be satisfactory, they are severely limited. No attempt was made to account in detail for the losses in the system; only a few test results were checked. Moreover, the relationship of the technique, and data obtained in the laboratory to the full-scale motors has not been treated.

The problem of combustion instability in liquid rocket motors has of course motivated a large number of works in the past twenty years. Of those, References 32-34 are concerned with the longitudinal, discrete wave motions. The techniques used are applicable only to periodic shock waves and hence have nothing to do with the transient growth of waves, although nonlinear stability is examined. The same sort of analysis was applied in Reference 35 to an end-burning solid propellant rocket motor. Obviously, because of that restriction, the important influence of mass addition along the lateral boundary is absent.

A modification of Galerkin's method has been used in References 37 and 38 to study stationary nonlinear wave motions in liquid propellant motors.

Extension of the technique to solid propellant motors with mass addition at the boundary, and to study travelling discrete pulses is not obvious and might encounter serious difficulties. Moreover, the transient growth or decay is not simply represented, and ultimately numerical computations are required. The important advantage of the approach is that only ordinary nonlinear differential equations need be treated.

In Reference 38, the observation that the instabilities in solid propellant motors often remain simply sinusoidal was used as the basis for constructing a single nonlinear ordinary differential equation to describe the motion. The equation is that for a nonlinear oscillator, and its solution gives a very good qualitative--to a limited extent quantitative--representation of transient growth of waves in T-burners. The failure of that work to produce anything like the harmonic content actually observed (albeit small) has motivated the work in Reference 39. It appears that the results will be simple to use and applicable to three-dimensional as well as one-dimensional, motions.

All of the analyses discussed above involve approximations of one sort or another. It is practically impossible to determine how good they are, particularly when the periodic motions are not represented as simple shock waves. Comparisons with experimental data are not entirely satisfying since usually fairly good results can be obtained by choosing appropriate values for the many parameters which necessarily arise. The situation will be much improved if an "exact" numerical analysis becomes available for checking approximate analyses. Thus, even if--as is likely the case-- it should be impractical to use numerical calculations to attempt correlations of all available data, nevertheless, an important gap is filled. A reasonable goal to head for is an approximate analysis valid for any configuration, and an accurate numerical analysis which can be used to check the approximations used, at least for one-dimensional problems.

2.4 Nonlinear Analyses of Instabilities in Liquid Rocket Motors

In addition to the works discussed above, there are some calculations of nonlinear waves in liquid rocket motors which are not applicable to the problem covered here but should be mentioned for completeness. One of

the most widely applied nonlinear instability models was originated by Priem and Guentert (Ref. 40). Their work has been modified and extended by several different investigators (Refs. 41-47), however, the model in all its forms is basically limited to the consideration of a two phase, liquid drop-gas, reacting mixture in a thin annulus. Depsite some of the shortcomings of the model, it does lead to the definition of stability limits in terms of engine design parameters; a feature which has led to a better understanding of liquid rocket instability. Priem's model is, however, not particularly well suited for an extension to solid rocket engines, and is limited to the consideration of transverse instability modes which are not being considered in the current program.

Burstein and Schechter (Ref. 48) have developed two-dimensional transient models. Two separate and complementary programs were developed describing, respectively, a pancake type motor ($r-\theta$ model) and a toroid with incremental thickness Δr (toroidal or $\theta-z$ model). The toroidal model is the first nonlinear analysis for investigating both tangential and longitudinal motions. Limited results were obtained mainly due to the excessive expense associated with solving two-dimensional transient governing equations. The pressure amplitude determined using the pancake model appeared to be unrealistically high. This can be partly attributed to energy accumulation in the plane z = constant. This is very similar to the constant energy assumption in the annulus required by the Priem analysis.

Recently Agosta (Ref. 49) developed a three-dimensional transient analysis. Numerical analysis was only carried out only for the one-dimensional case. Nonuniform droplet temperature was considered as a result of assuming finite thermal conductivity. Evaporation kinetics for nonequilibrium conditions were also included (Ref. 50) although the validity of this work at high pressure has yet to be proved. Theoretical wave form results were obtained for the transient one-dimensional model.

Many nonlinear extensions to the linear theory of the time lag model have been developed in studying instability of liquid rocket engines. Various approximation methods were used and the analyses do not depend totally on computerized solutions as those previously described. Based on this time-lag concept, Sirignano and Crocco (Ref. 32) studied longitudinal combustion instability for pressure waves of finite amplitude. Mass and energy addition

was assumed to occur only in an arbitrarily thin region next to the injector face. The solutions were shown to be unstable thus indicating the possibility of triggering longitudinal instability. Based on similar concepts Zinn (Ref. 51) studied transverse mode instability using oscillatory nozzle flow conditions while Sirignano employed the short nozzle concept. Michell (Ref. 33) extended the work of Sirignano to include possible discontinuous waves and distributed combustion. In this manner he was able to show that the final form of triggered longitudinal instability consisted of shock waves moving back and forth along the chamber. As noted above, the Galerkin method, with some modifications has been applied to some problems associated with combustion instability in liquid rocket engines. The important simplification achieved by the Galerkin method is that the nonlinear partial differential equations governing the problem are replaced by nonlinear ordinary differential equations. This is achieved by direct integration of the original equations over the volume of the chamber. Time remains as the sole independent variable. It is therefore natural to consider a disturbance which is distributed in space and maintains essentially the same spatial form in time, but has amplitude which changes nonlinearly in time.

Unfortunately, the analyses developed for liquid rocket instability studies cannot be easily applied to investigate solid propellant motor problems. One of the most crucial parts of all combustion instability problems is the coupling between the flow and the combustion processes. It is there that the source of energy for exciting and maintaining combustion instability resides. Heterogeneous combustion processes of solid propellants are totally different from liquid droplet burning which are usually governed by the rate of vaporization and/or gas phase kinetics. Furthermore, the spatial distribution of solid propellant grains, as in the case of motors with cylindrically perforated propellant grains, presents an entirely different problem formulation as compared with head-end injectors employed in liquid engines. As shown very strikingly by the results obtained here, the truly transient character of the burning under unsteady conditions is a fundamental part of the problem. Essentially all of the computations for instabilities in liquid rockets involve the assumption of quasi-steady coupling between

the flow and combustion. If that assumption were used in the present work, the results would be unrealistic and misleading.

The works of Powell and Zinn (Refs. 36,37) are most applicable to the analysis of standing waves where disturbances are distributed in space and maintain the same spatial form in time. These methods, with difficulty, could probably be modified and/or extended to treat solid rocket longitudinal instability. However, it is doubtful that all of the nonlinear coupling effects could be properly accounted for.

3. EQUATIONS OF MOTION

3.1 Discussion of the Mathematical Model

The flow in the combustion chamber of a metal loaded solid propellant rocket engine is calculated from a set of one-dimensional, unsteady, two-phase flow equations. Before presenting the equations, the assumptions upon which they are based are discussed.

It is assumed that the gas is ideal and nonreacting; the flow is inviscid and one-dimensional; the particles are spheres of a single size with uniform internal temperature, the particles are of negligible volume and do not interact with each other. The mass and particles coming from the burning surface are assumed to enter the chamber normal to the burning surface with zero tangential momentum, and at the adiabatic flame temperature.

Most solid rocket engine combustion chambers do not have rapid area changes, and the time for a pressure signal from the propellant surface to reach the centerline is usually a small fraction of the period of the longitudinal pressure waves; hence, a one-dimensional analysis should provide a reasonable approximation to the flow.

The combustion of a metal loaded solid propellant does not directly produce solid particles. The solid particles--aluminum oxide for aluminized propellants--are formed by the combustion of metal droplets which have been entrained by the gas flowing over the burning surface[61]. In the current work, however, the formation and combustion of the metal droplets has not been modeled and inert solid particles are assumed to be carried into the flow by the burning gases at a specified, and constant weight fraction.

In the analysis the particles are also assumed to be all of the same diameter, and all particles at a given location are assumed to have the same velocity and temperature. In actuality, the particle sizes form a distribution, which is at least bimodal due to two modes of oxide formation[61]. Quantitative particle distribution functions are not available, but the particle formation mechanisms are such as to produce both small 0-2μparticles (smoke) and larger 5-20μ particles.

Particle injection takes place continuously along the entire length of the chamber. Within a small volume, at any one time, various particles may possess different velocities and temperatures (even if they are all of the same size). This is a result of the fact that the history (trajectory) of each particle is different, and, in time, particles from different locations, injected at different times, can be in the same place. The ability to distinguish between particles because of their varying past histories is diminished with time, since all the particles eventually acquire the local velocity and temperature. For particles of radius, σ, mass, m, moving in a gas with viscosity, μ, characteristic times required for the particle to approach the local velocity and temperature may be defined (for Stokes flow) as:[62]

$$\tau_v = \frac{m}{6\pi\sigma\mu}$$
$$\tau_T = \frac{mC_p}{4\pi\sigma k} = \frac{mP_r}{4\pi\sigma\mu} \qquad (3\text{-}1)$$

Under typical conditions encountered in a solid rocket motor τ_v and τ_T are usually about 0.1 to 0.01 milli-seconds; only a fraction of the typical period of a longitudinal wave. Therefore, the current assumption that all particles at a given location and time have the same velocity and temperature, is a reasonable one. Although this assumption is a reasonable one it raises the conceptual problem of how the particles injected at a given time instantaneously acquire the local velocity and temperature of the gas. There are two modes by which this nonphysical event could be postulated to occur. The required energy and momentum could be instantly acquired from the gas, corresponding to infinite drag coefficient and Nusselt number. Or, alternatively, the newly injected particles may be said to instantly exchange energy and momentum with the other particles through collisional effects (infinite cross-section). The choice of one, or the other, of these postulates is reflected in the momentum and energy equations; however, as might be expected, as long as τ_v and τ_T are small compared to typical particle stay times in the chamber, the

choice makes little difference.

The equations, as used herein, imply the assumption of instantaneous acquisition of momentum and energy through collisions. The alternate forms of the equations are presented, for reference, in a footnote to the equations.

The assumptions previously mentioned, and discussed were made to allow the formulation of a relatively realistic nonlinear combustion instability model, without undue complication. The present model should allow for a reasonable assessment of this type of approach, and should it prove to be warranted, the model may be enhanced by the removal of one, or all, of the above assumptions.

3.2 Conservation Equations

Subject to the previous discussion, the equations of motion for the two phase mixture are as follows:

Continuity

Gas Phase
$$\frac{\partial}{\partial t^*}(\rho^* A^*) + \frac{\partial}{\partial x^*}(\rho^* u^* A^*) = \omega^* A^* \tag{3-2}$$

Particles
$$\frac{\partial}{\partial t^*}(\rho_p^* A^*) + \frac{\partial}{\partial x^*}(\rho_p^* u_p^* A^*) = \omega_p^* A^* \tag{3-3}$$

where asterisks denote dimensional variables, ρ^* and ρ_p^* are the gas and particle densities, respectively, u^* and u_p^* are, respectively, the gas and particle velocities, A^* is the chamber cross-sectional area, while ω^* and ω_p^* are the mass flux of gas and particles given off by the propellant per unit length, per unit cross-sectional area.

The quantity, ω^*, is related to the burning rate of the solid propellant, r^*, as follows:

$$\omega^* = \frac{\rho_s^* r^* \ell^*}{A^*(1+\beta_1)} \tag{3-4}$$

where ρ_s^* is the density of the solid propellant, ℓ^* is the perimeter of the grain, and β_1 is the weight ratio of solid particles to gas. The steady burning rate, r^*, is assumed to have the form

$$r^* = \tilde{C}^* \left[\frac{P}{P_{ref}}\right]^n (1 + C_k^* \; u^*) \tag{3-5}$$

Momentum

Gas Phase
$$\frac{\partial}{\partial t^*}(\rho^* u^* A^*) + \frac{\partial}{\partial x^*}(\rho^* u^{*2} A^*) = -\frac{\partial P^*}{\partial x^*} A^* + F_p^* A^* \tag{3-6}$$

Particles
$$\frac{\partial}{\partial t^*}(\rho_p^* u_p^* A^*) + \frac{\partial}{\partial x^*}(\rho_p^* u_p^{*2} A^*) = -F_p^* A^* \tag{3-7}$$

where the term F_p^* represents the effect of momentum transfer between the particle and gas. The momentum interaction is equal to the drag force exerted by the particles on the gas, per unit volume, and is given by

$$F_p^* = \frac{3}{8} \frac{\rho^* \rho_p^*}{\rho_m^* \sigma^*} C_D |u_p^* - u^*| (u_p^* - u^*) \tag{3-8}$$

where σ^* is the particle radius, ρ_m^* the density of the solid particles and C_D is the drag coefficient of the particles. The drag coefficient C_D is obtained from a well-established correlation of the so-called "standard" drag coefficient versus Reynolds number data. These data represent measurements for a single sphere in steady flow. The formula used was originated by Kliachko[63], and is,

$$C_D = \frac{24}{Re}\left(1 + \frac{Re^{2/3}}{6}\right) \tag{3-9}$$

The second term in the above equation represents a correction to the Stokes value, 24/Re, and allows the formula to be used at Reynolds numbers up to several hundred.

The gas and particle momentum equations (3-6) and (3-7) can be rewritten in modified form by subtracting the respective continuity equation, (3-2) or (3-3), after it has been multiplied by velocity (u^* or u_p^* as the case may be). The resulting modified momentum equations are:

Gas Phase+
$$\rho^* \frac{\partial u^*}{\partial t^*} + \rho^* u^* \frac{\partial u^*}{\partial x^*} = - u^* \omega^* - \frac{\partial P^*}{\partial x^*} + F_p^* \qquad (3\text{-}10)$$

Particles+
$$\rho_p^* \frac{\partial u_p^*}{\partial t^*} + \rho_p^* u_p^* \frac{\partial u_p^*}{\partial x^*} = - u_p^* \omega_p^* - F_p^* \qquad (3\text{-}11)$$

Energy

The energy equations for the particles and gas can be written in several different ways, in terms of internal energy, enthalpy, temperature, entropy, etc. The equations are written below in terms of temperature.

Gas Phase+
$$\rho^* C_p^* \frac{\partial T^*}{\partial t^*} + \rho^* u^* C_p^* \frac{\partial T^*}{\partial x^*} = \frac{1}{A^*} \frac{\partial}{\partial t^*} (P^* A^*) + u^* \frac{\partial P^*}{\partial x^*}$$
$$+ \omega^* \left[C_p^* (T_F^* - T^*) + \frac{u^{*2}}{2} \right] + F_p^* (u_p^* - u^*) + Q_p^* \qquad (3\text{-}12)$$

Particles+
$$\rho_p^* C_s^* \frac{\partial T_p^*}{\partial t^*} + \rho_p^* u_p^* C_s^* \frac{\partial T_p^*}{\partial x^*} = \omega_p^* \left[C_s^* (T_F^* - T_p^*) + \frac{u_p^{*2}}{2} \right]$$
$$- Q_p^* \qquad (3\text{-}13)$$

+As discussed in Section 3.1, the momentum and energy equations are slightly altered if it is assumed that the entering particles immediately acquire their momentum and energy from the gas flow. The differences are as follows: the term $u_p^* \omega_p^*$ must be subtracted from the r.h.s. of Eq. (3-10), and added to the r.h.s. of Eq. (3-11); the terms $u^* u_p^* \omega_p^*$ and $\omega_p^* \left[C_s^* (T_F^* - T_p^*) - 1/2 u_p^{*2} \right]$ $\omega_p^* \left[C_s^* (T_F^* - T_p^*) + \frac{u_p^{*2}}{2} \right]$ must be subtracted from the r.h.s. of Eq. (3-13).

where C_p^* and C_s^* are the heat capacities of the gas and solid, respectively, and Q_p^* represents the volumetric rate of heat transfer between the particles and gas.

$$Q_p^* = \rho_p^* C_p^* (T_p^* - T^*) / \left(\frac{m^* C_p^*}{2 Nu \pi \sigma^* k^*} \right) = \frac{\rho_p^* C_p^* (T_p^* - T^*)}{\tau_T^*} \tag{3-14}$$

where k^* is the gas thermal conductivity, Nu is Nusselt number and m^* is the mass of a particle,

$$m^* = \frac{4}{3} \pi \sigma^{*3} \rho_m^* \tag{3-15}$$

The parameter $\tau_T^* = (m^* C_p^*)/(2 Nu \pi \sigma^* k^*)$ is the thermal relaxation time constant, i.e., τ_T^* is the characteristic time it takes the particles to adjust to the local gas temperature. The Nusselt number is a function of Reynolds number and Prandtl number. The following expression suggested by Carlson[64] is used:

$$Nu = 2 + .459 \, Re^{.55} Pr^{.33} \tag{3-16}$$

Here again, the second term represents a correction to the Stokes flow value, i.e., Nu = 2. The gaseous equation of state is also required and is

$$P^* = \rho^* R T^* \tag{3-17}$$

3.3 Nondimensional Equations

In an effort to improve the accuracy and reduce the possibility of round-off error in the solution, the independent and dependent variables have been normalized. The resulting normalized (nondimensional) variables are more uniform in magnitude. The following new variables have, therefore, been

defined:

$$
\begin{aligned}
x &= x^*/L & T &= T^*/T_F^* & A &= A^*/L^{*2} \\
t &= t^* a^*_F/L^* & P &= P^*/P_F^* & \omega &= \omega^* L^*/\rho_F^* a_F^* \\
u &= u^*/a_F^* & \rho &= \rho^*/\rho_F^* & \omega_p &= \omega_p^* L^*/\rho_F^* a_F^* \qquad (3\text{-}18) \\
\rho_p &= \rho_p^*/\rho_F^* & T_p &= T_p^*/T_F^* & F_p &= F_p^* L^*/\rho_F^* a_F^{*2} \\
u_p &= u_p^*/a_F^* & C &= C_s^*/C_p^* & Q_p &= Q_p^* L^*/\rho_F^* C_p^* a_F^* T_F^* \\
a &= a^*/a_F^*
\end{aligned}
$$

where T_F^* is the propellant adiabatic flame temperature, P_F^* is chamber pressure, ρ_F^* and a_F^* are the density and sound speed evaluated at the chamber conditions and L^* is a reference length, usually the length of the grain.

In terms of these nondimensional variables equations (3-2), (3-3), (3-10 to 13) and (3-17) become:

<u>Continuity</u>

$$\frac{\partial}{\partial t}(\rho A) + \frac{\partial}{\partial x}(\rho u A) = \omega A \qquad (3\text{-}19)$$

$$\frac{\partial}{\partial t}(\rho_p A) + \frac{\partial}{\partial x}(\rho_p u_p A) = \omega_p A \qquad (3\text{-}20)$$

<u>Momentum</u>

$$\rho \frac{\partial u}{\partial t} + \rho u \frac{\partial u}{\partial x} = -u\omega - \frac{1}{\gamma}\frac{\partial P}{\partial x} + F_p \qquad (3\text{-}21)$$

$$\rho_p \frac{\partial u_p}{\partial t} + \rho_p u_p \frac{\partial u_p}{\partial x} = -\omega_p u_p - F_p \qquad (3\text{-}22)$$

Energy

$$\rho \frac{\partial T}{\partial t} + \rho u \frac{\partial T}{\partial x} = \frac{\gamma - 1}{\gamma} \left[\frac{1}{A} \frac{\partial (PA)}{\partial t} + u \frac{\partial P}{\partial x} \right] + \omega \left[(1-T) + \frac{\gamma - 1}{2} u^2 \right]$$

$$+ (\gamma - 1) F_p (u_p - u) + Q_p \tag{3-23}$$

$$\rho_p \frac{\partial T_p}{\partial t} + \rho_p u_p \frac{\partial T_p}{\partial x} = \omega_p (1 - T_p) + \left(\frac{\gamma - 1}{2} \right) \frac{\omega_p u_p^2}{C} - \frac{Q_p}{C} \tag{3-24}$$

State

$$P = \rho T \tag{3-25}$$

The nondimensional sound speed, $a = a^*/a_F^*$, is given by,

$$a = \sqrt{T} \tag{3-26}$$

3.4 Characteristic Equations

The equations of the characteristic lines, and their corresponding compatibility relations, can now be developed as follows: $\rho = P/T$ is substituted into equation (3-19) and the resulting temperature derivatives are eliminated using the energy equation (3-23), this yields

$$\frac{1}{\gamma} \left[\frac{\partial P}{\partial t} + u \frac{\partial P}{\partial x} \right] + P \frac{\partial u}{\partial x} = - \frac{P}{\gamma A} \frac{\partial A}{\partial t} - \frac{uP}{A} \frac{\partial A}{\partial x} + \omega + \left[\frac{\gamma - 1}{2} \right] \omega u^2$$

$$+ (\gamma - 1) F_p (u_p - u) + Q_p \tag{3-27}$$

The momentum equation (3-21) is then multiplied by an unknown multiplier, q, and added to equation (3-27), this gives

$$\frac{1}{\gamma}\left[\frac{\partial P}{\partial t} + (u+q)\frac{\partial P}{\partial x}\right] + \rho q \frac{\partial u}{\partial t} + \rho q\left[u + \frac{P}{\rho q}\right]\frac{\partial u}{\partial x} = -\frac{P}{\gamma A}\frac{\partial A}{\partial t}$$

$$- \frac{uP}{A}\frac{\partial A}{\partial x} + \omega(1-uq) + \frac{(\gamma-1)}{2}\omega u^2 + F_p\left[(\gamma-1)(u_p-u) + q\right] + Q_p \tag{3-28}$$

If the total derivatives of pressure and velocity are to be the same then the condition

$$q = \frac{P}{\rho q} \qquad \text{or} \qquad q^2 = \frac{P}{\rho} \tag{3-29}$$

must be satisfied. Since $a^2 = P/\rho$, this condition leads to

$$q = \pm a \tag{3-30}$$

If $\frac{\delta^+}{\delta t} = \frac{\partial}{\partial t} + (u+a)\frac{\partial}{\partial x}$ and $\frac{\delta^-}{\delta t} = \frac{\partial}{\partial t} + (u-a)\frac{\partial}{\partial x}$ (3-31)

are defined as the total derivatives along the characteristics lines given by

$$\frac{dx}{dt} = u \pm a \tag{3-32}$$

then equation (3-28) with (3-30) yields the following compatiblity relations:

$$\frac{1}{\gamma\rho a}\frac{\delta^+ P}{\delta t} + \frac{\delta^+ u}{\delta t} = -\frac{a}{A}\left[\frac{1}{\gamma}\frac{\partial A}{\partial t} + u\frac{\partial A}{\partial x}\right] + \frac{\omega}{\rho a}\left[(1-ua) + \left(\frac{\gamma-1}{2}\right)u^2\right]$$

$$+ \frac{F_p}{\rho a}\left[(\gamma-1)(u_p-u) + a\right] + \frac{Q_p}{\rho a} \tag{3-33}$$

$$\frac{1}{\gamma\rho a}\frac{\delta P}{\delta t} - \frac{\delta u}{\delta t} = -\frac{a}{A}\left[\frac{1}{\gamma}\frac{\partial A}{\partial t} + u\frac{\partial A}{\partial x}\right] + \frac{\omega}{\rho a}\left[(1+ua) + \left(\frac{\gamma-1}{2}\right)u^2\right]$$

$$+ \frac{F_p}{\rho a}(\gamma-1)(u_p - u) - a + \frac{Q_p}{\rho a} \tag{3-34}$$

The gas energy equation (3-23) is already in characteristic form. The gas streamlines

$$\frac{dx}{dt} = u \tag{3-35}$$

are characteristic lines, and if

$$\frac{\delta}{\delta t} = \frac{\partial}{\partial t} + u\frac{\partial}{\partial x} \tag{3-36}$$

is defines as the total derivative along the streamlines, then the energy equation becomes the compatibility relation, and may be written as

$$\rho\frac{\delta T}{\delta t} - \frac{(\gamma-1)}{\gamma}\frac{\delta P}{\delta t} = \frac{(\gamma-1)}{\gamma}\frac{P}{A}\frac{\partial A}{\partial t} + \omega\left[(1-T) + \frac{\gamma-1}{2}u^2\right]$$

$$+ (\gamma-1)F_p(u_p - u) + Q_p \tag{3-37}$$

A particle path,

$$\frac{dx}{dt} = u_p \tag{3-38}$$

is a dual characteristic. Defining,

$$\frac{\delta_p}{\delta t} = \frac{\partial}{\partial t} + u_p\frac{\partial}{\partial x} \tag{3-39}$$

as the total derivative along a particle path, allows the particle momentum and energy equations (3-22) and (3-24) to be written as

$$\rho_p \frac{\delta_p u_p}{\delta t} = - \omega_p u_p - F_p \tag{3-40}$$

$$\rho_p \frac{\delta_p T_p}{\delta t} = \omega_p (1 - T_p) + \left(\frac{\gamma - 1}{2}\right) \frac{\omega_p}{C} u_p^2 - \frac{Q_p}{C} \tag{3-41}$$

The particle continuity equation (3-20) becomes uncoupled from the remaining equations (since there is no particle equation of state which relates particle density to particle temperature) and cannot be written in characteristic form. It can, however, be written in the following alternative form

$$\frac{\delta_p \rho_p}{\delta t} + \rho_p \frac{\partial u_p}{\partial x} = \omega_p - \frac{\rho_p}{A} \frac{\delta_p A}{\delta t} \tag{3-42}$$

The required equations of motion are, therefore: the equations of the four characteristic lines, equations (3-32), (3-35), (3-38); the five compatibility relations, equations (3-33), (3-34), (3-37), (3-40), (3-41); and the particle continuity equation (3-42). These equations, together with the equation of state, (3-25), the transient burning rate analysis (Section 4), boundary conditions (Section 5), and initial conditions (Section 6), form the complete mathematical model of the instability problem.

4.0 RESPONSE FUNCTION FOR TRANSIENT BURNING

In general one must expect that the combustion processes will respond to both pressure and velocity fluctuations. Moreover, although this has not been established experimentally, the response may be nonlinear in addition to the intrinsic dependence on the magnitude of velocity fluctuations mentioned in Section 2.3. Other than a numerical calculation of the response to an exponential change of pressure (Ref. 58), there have been three treatments of the nonlinear response to pressure coupling (Refs. 55,56, 57). All are restricted to harmonic motions, and seek to obtain nonlinear heat conduction solutions. There are open questions, however, about the validity of these analyses. The present treatment is based on a linear solution for the heat conduction in the solid, coupled to a nonlinear solution of the chamber flow dynamics. This approach seems to be justified based on observation of data.

The method for calculating both the pressure coupled (Section 4.2) and velocity coupled (Section 4.3) response to disturbances of arbitrary waveform is essentially an extension of the analysis of the response to harmonic oscillations. Therefore, a summary of the harmonic analysis is included here to clarify the origin of the parameters required in the numerical analysis. The influence of aluminum is not explicitly accounted for.

4.1 Linear Response To Harmonic Pressure Oscillations

It has been shown (Ref. 59) that almost all existing analyses of the response of a burning solid to harmonic pressure fluctuations lead to essentially the same functional dependence on frequency. The reason, logically enough, is that all are based on the same assumptions, namely:

(1) The gas and solid phases are treated as homogeneous phases, and only variations in the direction normal to the burning surface are accounted for.

(2) Conversion of solid to gas occurs at an infinitesimally thin interface; in particular, no chemical reactions are present in the solid.

(3) The gas phase responds quasi-statically so that only the steady-state solution is required. This assumption is justified by the fact that processes in the gas phase are much faster than those in the solid.

The analysis is then conveniently split into three parts: the solid, the gas, and the interface.

4.1.1 Solid Phase

A coordinate system fixed to the gas/solid interface is used. With the approximations listed above, and assuming also that the material properties are constant, the problem reduces to the heat conduction equation,

$$\rho_s C_s \frac{\partial T}{\partial t} + \rho_s C_s \frac{\partial T}{\partial x} = k_s \frac{\partial^2 T}{\partial x^2} \tag{4-1}$$

The equation is linearized by writing $T = \overline{T} + T'$, $r = \overline{r} + r'$; the steady-state and fluctuating temperatures satisfy

$$\rho_s C_s \overline{r} \frac{d\overline{T}}{dx} = k_s \frac{d^2 \overline{T}}{dx^2} \tag{4-2}$$

$$\rho_s C_s \frac{\partial T'}{\partial t} + \rho_s C_s \overline{r} \frac{\partial T'}{\partial x} = k_s \frac{\partial^2 T'}{\partial x^2} - \rho_s \quad r' \frac{d\overline{T}}{dx} \tag{4-3}$$

From (4-2), with the conditions

$$\overline{T} = T_s \qquad (x \to -\infty)$$

$$\overline{T} = T_w \qquad (x = 0) \tag{4-4}$$

one finds

$$\frac{\overline{T} - T_s}{T_w - T_s} = e^{\xi_s} \tag{4-5}$$

where

$$\xi_s = \frac{\overline{r}}{\kappa_s} \; x \tag{4-6}$$

It is sufficient for linear problems to examine the case of harmonic time variations. The solution to Eq. (4-3), yields the formula for fluctuations of heat transfer from the interface into the solid,

$$\left[k_s \frac{\partial T}{dx}\right]_- = \bar{m} C_s \left[\lambda T'_w + \left(\frac{\bar{T}_w - T_s}{\lambda}\right) \frac{m'_w}{\bar{m}}\right] \tag{4-7}$$

where $m'_w = \rho_s r'$ is the fluctuation of mass flux, T'_w is the fluctuation of surface temperature, and λ is the complex function of frequency:

$$\lambda = 1/2 \left\{1 + \frac{1}{\sqrt{2}} \left[\sqrt{1+16\Omega^2} + 1\right]^{1/2}\right\} \tag{4-8}$$

$$\Omega = \frac{\varkappa_s \omega}{\bar{r}^2} \tag{4-9}$$

where ω is angular frequency of the waves.

It is common practice to assume that a simple pyrolysis law of the Arrhenius form applies:

$$m_w = B_w p^{n_w} e^{-E_w/R_o T_w} \tag{4-10}$$

Thus, the fluctuations of mass flux and surface temperature are related by

$$\frac{m'_w}{\bar{m}} = E \frac{T'_w}{\bar{T}_w} + n_w \frac{p'}{\bar{p}} \tag{4-11}$$

with the normalized activation energy for the surface reaction

$$E = E_w/R_o \bar{T}_w \tag{4-12}$$

Equations (4-7) and (4-11) may be combined to yield the desired result,

$$\left[k_s \frac{\partial T}{\partial x}\right]'_- = \left[\lambda + \frac{A}{\lambda}\right] \frac{T'_w}{\bar{T}_w} + n_w \left[\frac{1 - T_s/\bar{T}_w}{\lambda}\right] \frac{p'}{\bar{p}} \tag{4-13}$$

where the important parameter A is defined as:

$$A = \left(1 - \frac{T_s}{\bar{T}_w}\right) E \tag{4-14}$$

4.1.2 Interface

By examining conservation of mass and energy for a control volume encompassing the interface, one finds the general "jump" conditions

$$\rho_s r = \rho_g u_g \tag{4-15}$$

$$\rho_s r h_{w-} - \left[k_s \frac{\partial T}{\partial x}\right]_- = \rho_g u_g h_{w+} - \left[k_g \frac{\partial T}{\partial x}\right]_+ \tag{4-16}$$

in which the enthalpies on the solid and gas sides of the interface are h_{w-}, h_{w+}, respectively. The heat of reaction associated with the processes at the interface is Q_w,

$$Q_w = h_{w-} - h_{w+} \tag{4-17}$$

and $Q_w > 0$ for an exothermic reaction.

The perturbation of (4-16) is

$$\left[k_g \frac{\partial T}{\partial x}\right]'_+ = \left[k_s \frac{\partial T}{\partial x}\right]'_- + \bar{m}(C_p - C_s)T'_w - m'_w Q_w \tag{4-18}$$

and with (4-13), one has

$$\frac{1}{\bar{m} C_s \bar{T}_w}\left[k_g \frac{\partial T}{\partial x}\right]'_+ = \left[\left(\lambda + \frac{A}{\lambda}\right) + \left(\frac{C_p}{C_s} - 1 - AH\right)\right]\frac{T'_w}{\bar{T}_w}$$

$$+ n_w\left[1 - \frac{T_s}{\bar{T}_w}\right]\left[\frac{1}{\lambda} - H\right]\frac{p'}{\bar{p}} \tag{4-19}$$

where

$$H = \frac{Q_w}{C_s(\overline{T}_w - T_s)} \tag{4-20}$$

4.1.3 Gas Phase

This is the most difficult part of the problem if one wishes to cope with the details of the flame. However, it turns out that, owing to the assumption of quasi-static behavior, no matter what model one selects for the flame structure, the ultimate form of the response functions will be the same. For simplicity, the most elementary model will be discussed.

The energy equation for a thermal theory of flame propagation is

$$m\, C_p \frac{dT}{dx} = \frac{d}{dx}\left(k_g \frac{dT}{dx}\right) + Q_f\, w \tag{4-21}$$

where Q_f is the heat release per unit mass, and w is the reaction rate (sec^{-1}) divided by the gas density. This equation must be solved subject to the conditions

$$\left[k_g \frac{dT}{dx}\right]_+ = m\left[C_s(T_w - T_s) - Q_w\right] \tag{4-22}$$

at the surface ($x = 0$), and

$$\begin{aligned} T &= T_f \\ \frac{dT}{dx} &= 0 \end{aligned} \tag{4-23}$$

at the downstream edge of the flame ($x \to \infty$).

Now suppose that the energy release is uniform in the region from the surface to the edge of the flame ($x = x_f$) so $Q_f w$ is constant. This case has been treated in References 58 and 59. Equation (4-21) can then be integrated directly (note that $m = \rho_g u_g$ is constant) to give the formula for the heat

transfer to the surface

$$\left[k_g \frac{dT}{dx}\right]_+ = \frac{Q_f k_g}{C_p} \left[1 - \exp(-mC_p x_f/k_g)\right] \frac{w}{m} \tag{4-24}$$

It happens that for typical values of the quantities involved, the exponential involving x_f is negligible:

$$\frac{mC_p}{k_g} x_f \equiv \frac{\rho_s r}{k_g} C_p x_f = \left[\frac{C_p k_s}{C_s k_g}\right] \frac{r}{\kappa_s} x_f$$

$$\approx (1) \frac{(1 \text{ cm/sec})}{(10^{-3} \text{ cm/sec})} x_f$$

$$\approx 1000 x_f$$

Even if x_f is as unrealistically small as 20 microns, $1000 x_f = 2$; hence the approximation is quite good, and (4-24) becomes

$$\left[k_g \frac{dT}{dx}\right]_+ = \left[\frac{Q_f k_g}{C_p}\right] \frac{w}{m} \tag{4-25}$$

The perturbation of the last equation is

$$\left[k_g \frac{dT}{dx}\right]'_+ = \bar{m} C_p \Lambda^2 \left(\frac{w'}{\bar{w}} - \frac{m'}{\bar{m}}\right) \tag{4-26}$$

where

$$\Lambda^2 = \frac{Q_f k_g \bar{w}}{(\bar{m} C_p)^2 \bar{T}_w} \tag{4-27}$$

It remains only to find an expression for w, and, hence, w'.

Suppose that the reactions are mainly sensitive to changes of pressure, so $w' \sim p'$. It is convenient to define W by

$$\frac{C_p}{C_s}\left[\frac{\Lambda^2}{1-T_s/\bar{T}_w}\right]\frac{w'}{\bar{w}} = W\,\frac{p'}{\bar{p}} \tag{4-28}$$

With this assumption, (4-26) becomes

$$\left[k_g\,\frac{dT}{dx}\right]'_+ = \bar{m}\,C_s\bar{T}_w\left[\left(1-\frac{T_s}{\bar{T}_w}\right)W\,\frac{p'}{\bar{p}} - \frac{C_p}{C_s}\Lambda^2\,\frac{m'}{\bar{m}}\right] \tag{4-29}$$

which is the result required of the solution for the gas phase.

4.1.4 Linear Response Function and Fluctuations of the Flame Temperature

Equations (4-11), (4-19), and (4-29) can be combined to yield the ratio

$$\frac{m'/\bar{m}}{p'/\bar{p}} = \frac{\left(AW+\frac{C_p}{C_s}n_w\right)+n_w(\lambda-1)}{\lambda+\frac{A}{\lambda}+\frac{C_p}{C_s}E\Lambda^2-HA+\frac{C_p}{C_s}-1} \tag{4-30}$$

In the limit of zero frequency, $\lambda \to 1$ and (4-29) must reproduce the small change of burning rate due to a small change of pressure in steady state burning. For the common case $r \sim p^n$, this implies that the ratio (4-30) must equal n for $\omega \to 0$; i.e.,

$$n\left[A(1-H)+\frac{C_p}{C_s}E\Lambda^2+\frac{C_p}{C_s}\right] = A\left[W+\frac{C_p}{C_s}\,\frac{n_w}{A}\right] \tag{4-31}$$

Define the parameter B as

$$B = \frac{1}{n}\left[W+\frac{C_p}{C_s}\,\frac{n_w}{A}\right] \tag{4-32}$$

and the condition (4-31) is

$$\frac{C_p}{C_s} E\Lambda^2 - HA + \frac{C_p}{C_s} - 1 + (A+1) = AB \tag{4-33}$$

Hence, (4-30) has the simpler form

$$\frac{m'/\bar{m}}{p'/\bar{p}} = \frac{nAB + n_w\ (\lambda - 1)}{\lambda + \frac{A}{\lambda} - (1+A) + AB} \tag{4-34}$$

(Incidentally, with a bit of effort, one can show that (4-33) implies satisfaction of the mean energy balance at the gas/solid interface written in a slightly obscure form).

Equation (4-34) is proportional to the response function, R_b, usually defined as

$$R_b = \frac{m'/\bar{m}}{p'/\gamma\bar{p}} = \gamma\left(\frac{m'/\bar{m}}{p'/\bar{p}}\right) \tag{4-35}$$

A second quantity, the admittance function, is also important in studies of instability. This is defined as

$$A_b = \frac{u'/\bar{a}}{p'/\nu\bar{p}} = M_b\ \frac{u'/\bar{u}}{p'/\nu\bar{p}} \tag{4-36}$$

Now from the definition of $m = \rho u$*

$$\frac{m'}{\bar{m}} = \frac{u'}{\bar{u}} + \frac{\rho'}{\bar{\rho}}$$

or

$$M_b\ R_b = A_b + \frac{\rho'/\bar{\rho}}{p'/\gamma\bar{p}}\ M_b \tag{4-37}$$

*Note that owing to the way in which the mass flux is used here, the assumption is implicit that the propellant contains no metal. When applied to metallized propellants, $\bar{m}$ and m' must then be the values for the gases only.

With the perfect gas law, (4-37) can be written

$$R_b = M_b A_b + \gamma \cdot \frac{T'/\overline{T}}{p'/\gamma \overline{p}} \tag{4-38}$$

Here T' is really T_f', which can be written as the sum of an isentropic part and a nonisentropic part:

$$\frac{T_f'}{\overline{T}_f} = \left(\frac{T_f'}{\overline{T}_f}\right)_{isent.} + \left(\frac{T_f'}{\overline{T}_f}\right)_{non-isent.} = \frac{\gamma-1}{\gamma}\,\frac{p'}{\overline{p}} + \frac{\Delta T_f'}{\overline{T}_f} \tag{4-39}$$

Thus, (4-38) becomes

$$R_b - 1 = M_b A_b - \frac{\Delta T_f'/\overline{T}_f}{p'/\gamma \overline{p}} \tag{4-40}$$

The last result is generally true for linear variations. With the analysis leading to (4-34) one can deduce an explicit expression for $\Delta T_f'$ and hence for the admittance function. Consider first a control volume extending from the solid/gas interface downstream beyond the combustion zone; the energy balance for this region is

$$\left[k_g \frac{dT}{dx}\right]_+ = m\,(h_{w+} - h_f) = m\left[Q_f - C_p(T_f - T_w)\right] \tag{4-41}$$

where Q_f is again the energy released, per unit mass of flow, by chemical reactions. The perturbation of (4-41) is

$$T_f' = T_w' + \frac{m'}{\overline{m}}\left[\frac{Q_f}{C_p} - (\overline{T}_f - \overline{T}_w)\right] - \frac{1}{\overline{m}C_p}\left[k_g \frac{dT}{dx}\right]_+'$$

$$T_f' = T_w' + \left\{\left[\frac{Q_f}{C_p} - (\overline{T}_f - \overline{T}_w)\right] + \frac{C_p}{C_s}\Lambda^2\right\}\frac{m'}{\overline{m}} - \left[1 - \frac{T_s}{\overline{T}_w}\right] W\,\frac{p'}{\overline{p}} \tag{4-42}$$

The mean energy balance for a control volume extending from deep within the solid to a plane on the gas side of the interface is

$$\left[k_g \frac{dT}{dx}\right]_+ = C_s(\overline{T}_w - T_s) - Q_w \tag{4-43}$$

With (4-41), one has the identity for use in (4-42):

$$Q_f - C_p(\overline{T}_f - T_w) = C_s(\overline{T}_w - T_s) - Q_w \tag{4-44}$$

Also, combination of (4-25), written for steady burning, and (4-43) gives a formula for Λ^2:

$$\frac{C_p}{C_s} E\Lambda^2 = A(1 - H) \tag{4-45}$$

Now after the Arrhenius law (4-11) is used to eliminate T'_s from (4-42), and Equations (4-43) and (4-45) are substituted appropriately, the result is

$$\frac{T'_f}{\overline{T}_f} = \frac{\overline{T}_w}{\overline{T}_f}\left[\frac{1}{E} + 2\frac{C_s}{C_p}\frac{A}{E}(1-H)\right]\frac{m'}{\overline{m}} - \frac{\overline{T}_w}{\overline{T}_f}\left[\frac{C_s}{C_p}\right]\left[\frac{nAB}{E}\right]\frac{p'}{\overline{p}} \tag{4-46}$$

The bracketed terms multiplying $m'/\overline{m}$ can be rewritten, using (4-33) and (4-45) as

$$\frac{1}{E}\left[1 + 2\frac{C_s}{C_p}A(1-H)\right] = \frac{A}{E}\frac{C_s}{C_p}B \tag{4-47}$$

and with (4-35), one now has

$$\frac{T'_f}{\overline{T}_f} = \frac{C_s}{C_p}\frac{\overline{T}_w}{\overline{T}_f}\frac{nAB}{E}\left(\frac{1}{\gamma n}R_b - 1\right)\frac{p'}{\overline{p}} \tag{4-48}$$

To find the nonisentropic part of (4-48), write $T'_f/\overline{T}_f$ as in (4-39), and the last equation produces

$$\frac{\Delta T'_f}{\overline{T}_f} = \left[n\frac{C_s}{C_p}\frac{\overline{T}_w}{\overline{T}_f}\frac{AB}{E}\left(\frac{1}{\gamma n}R_b - 1\right) - \left(\frac{\gamma - 1}{\gamma}\right)\right]\frac{p'}{\overline{p}} \tag{4-49}$$

From the definitions of R_b and A_b, this can also be written as

$$\frac{\Delta T_f'}{\overline{T}_f} = \frac{1}{\gamma}\left[\frac{A_b}{\overline{M}_b} - (R_b - 1)\right]\frac{p'}{\overline{p}} \tag{4-50}$$

This completes the elementary linear analysis for harmonic motions. The fluctuations m', T_f', etc., are of course complex amplitudes with phases measured with respect to the pressure oscillation. It should be noted that (4-50) is a general result, whereas (4-49) involves the assumptions listed at the beginning of this discussion.

Although the flame temperature must in principle oscillate according to the preceding result, this behavior is not currently included in the numerical analysis. There is no reason why it cannot be incorporated, and, in fact, variable flame temperature will be added to the model as soon as possible. In the meantime, the exclusion of this effect should not affect the immediate task of assessing the possible value of the current approach to solid rocket instability.

4.2 Linear Response to an Arbitrary Change of Pressure

The response function, Equation (4-34), has been derived as the sensitivity to harmonic oscillations. However, simply by taking $i\Omega$ as the variable, (4-34) can be treated as a Laplace transform. Henceforth, the influence of surface reactions will be ignored ($n_w = 0$) so with $s = i\Omega$,

$$\frac{1}{nAB}\,\frac{m'}{\overline{m}}(s) = \frac{\lambda(s)}{\lambda^2(s) + (AB-A-1)\,\lambda(s) + A}\,\frac{p'}{\overline{p}}(s) \tag{4-51}$$

Note that $s = i\kappa\omega/\bar{r}^{a}$ is the dimensionless Laplace transform variable as associated with the dimensionless real time $\tilde{t}$,

$$\tilde{t} = \frac{\bar{r}^{a}\,t}{\kappa} \tag{4-52}$$

Thus, for any function $f(\tilde{t})$ having transform $F(s)$,

$$F(s) = \int_0^\infty f(\tilde{t})\, e^{-s\tilde{t}}\, d\tilde{t} \tag{4-53}$$

$$f(\tilde{t}) = \frac{1}{2\pi i} \int F(s)\, e^{s\tilde{t}}\, ds \tag{4-54}$$

Now define a new Laplace transform variable p,

$$p = 1 + 4s \tag{4-55}$$

so that the quantity λ is

$$\lambda = \frac{1}{2}\left[1 + \sqrt{1+4s}\right] = \frac{1}{2}\left[1 + \sqrt{p}\right] \tag{4-56}$$

Substitute (4-55) into the Laplace transform pair (4-53) and (4-54) to find

$$F(p) = \int_0^\infty \left[4\, e^{\tau} f(\tau)\right] e^{-p\tau}\, d\tau \tag{4-57}$$

$$\left[4\, e^{\tau} f(\tau)\right] = \frac{1}{2\pi i} \int F(p)\, e^{p\tau}\, dp \tag{4-58}$$

where

$$\tau = \tilde{t}/4 = \frac{\bar{r}^2 t}{4\kappa} \tag{4-59}$$

Hence, what appears now is $4e^{\tau}$ times the desired function of time, not the function itself.

The inverse transform of (4-51) gives $m'/\bar{m}$ as a function of $\tilde{t}$:

$$\frac{1}{nAB}\, \frac{m'}{\bar{m}}(\tilde{t}) = \frac{1}{2\pi i} \int \frac{\lambda(s)}{\left[\lambda^2 + (AB-A-1)\lambda + A\right]}\, \frac{p'}{\bar{p}}(s)\, e^{s\tilde{t}}\, ds \tag{4-60}$$

and if the substitutions $\tilde{t} \to \tau$, $s \to p$ are made,

$$\frac{1}{2nAB}\left[4e^{\tau}\frac{m'}{\bar{m}}(\tau)\right] = \frac{1}{2\pi i}\int \frac{(1+\sqrt{p})}{(\sqrt{p}-\sigma_1)(\sqrt{p}-\sigma_2)}\frac{p'}{\bar{p}}e^{p\tau}dp \tag{4-61}$$

where σ_1, σ_2 are the roots of the denominator,

$$\sigma_1 = -A(B-1) + i\sqrt{4A-(AB-A-1)^2} \tag{4-62a}$$

$$\bar{\sigma}_1 = \sigma_2 = -A(B-1) - i\sqrt{4A-(AB-A-1)^2} \tag{4-62b}$$

Thus, σ_1, σ_2 are complex conjugates.

In principle, (4-61) can be used for numerical calculations. For by use of the convolution theorem, if $p'/\bar{p}(\tau)$ is the inverse transform of $p'/\bar{p}(p)$ and $K(\tau)$ is the inverse of the remainder of the integrand, then formally

$$\frac{1}{2nAB}\left[4e^{\tau}\frac{m'}{\bar{m}}(\tau)\right] = \int_0^{\infty} 4e^{\xi}K(\xi)\cdot 4e^{\tau-\xi}\frac{p'}{\bar{p}}(\tau-\xi)\,d\xi$$

or

$$\frac{1}{8nAB}\frac{m'}{\bar{m}}(\tau) = \int_0^{\infty} K(\xi)\frac{p'}{\bar{p}}(\tau-\xi)\,d\xi \tag{4-63}$$

Note that the factor $4e^{\tau}$ must be carried along according to earlier remarks.

Unfortunately, the function $K(\xi)$ turns out to be extremely awkward to handle numerically. It contains terms involving complex error functions and exponentials such as $e^{\sigma_1^2(\tau-\xi)}\operatorname{erfc}(\sigma_1\sqrt{\tau-\xi})$. This combination can be shown to be equivalent to the $W(z)$ function defined on page 297 of Reference 70.

Several different series representations may be used to represent the above term. Each series, however, is either convergent in only part of the complex plane, or if convergent everywhere, is only very slowly convergent in part of the range of interest. It turns out, therefore, that even by using different series with overlapping regions of convergence there are parts of the complex plane of interest where many terms have to be taken in the series.

Since, in an instability solution, the burning rate integral must be carried out from 0 to the current time at each of many x locations, every time; the computation time involved in evaluating the integrand becomes prohibitive when the series are so slowly convergent. The fact that complex arithmetic must be used further serves to amplify the problem.

The numerical difficulties of the direct approach can be avoided by use of an alternate procedure. If (4-51) is written in terms of P, using (4-56) and (4-62), equation (4-51) can be written in terms of P as,

$$\frac{1}{2nAB}\left[1 - \frac{\sigma_1 + \sigma_2}{\sqrt{p}} + \frac{\sigma_1\sigma_2}{p}\right]\frac{m'}{\bar{m}}(p) = \left[\frac{1}{p} + \frac{1}{\sqrt{p}}\right]\frac{p'}{\bar{p}}(p) \tag{4-64}$$

Now take the inverse transform to find

$$\begin{aligned}\frac{m'}{\bar{m}}(\tau) = {} & \frac{\sigma_1 + \sigma_2}{\sqrt{\pi}}\int_0^\tau \frac{m'}{\bar{m}}(\tau - \xi)\, e^{-\xi}\frac{d\xi}{\sqrt{\xi}} - \sigma_1\sigma_2 e^{-\tau}\int_0^\tau \frac{m'}{\bar{m}}(\xi) e^{\xi}\, d\xi \\ & + 2nAB\left\{\frac{1}{\sqrt{\pi}}\int_0^\tau \frac{p'}{\bar{p}}(\tau - \xi) e^{-\xi}\frac{d\xi}{\sqrt{\xi}} + e^{-\tau}\int_0^\tau \frac{p'}{\bar{p}}(\xi) e^{\xi}\, d\xi\right\}\end{aligned} \tag{4-65}$$

Although this is not an explicit formula for $m'/\bar{m}$, the functions under the integrals are easy to handle numerically.

Equation (4-65) does present a problem at the lower limit of the integral, $\xi \to 0$, since the integrand becomes infinite. This singularity can be handled by dividing the integral into two pieces, and approximating the part near $\xi = 0$.

Thus,

$$\int_0^{\tau} f(\tau-\xi)e^{-\xi}\frac{d\xi}{\sqrt{\xi}} = \int_0^{\delta} f(\tau-\xi)e^{-\xi}\frac{d\xi}{\sqrt{\xi}} + \int_{\delta}^{\tau} f(\tau-\xi)e^{-\xi}\frac{d\xi}{\sqrt{\xi}} \tag{4-66}$$

where $\delta \to 0$. If only the first two terms in a Taylor's series expansion are retained, the first integral has the following value:

$$\int_0^{\delta} f(\tau-\xi)e^{-\xi}\frac{d\xi}{\sqrt{\xi}} \approx f(\tau)\int_0^{\delta} e^{-\xi}\frac{d\xi}{\sqrt{\xi}} - \frac{df}{d\tau}\int_0^{\delta} e^{-\xi}\sqrt{\xi}\,d\xi$$

$$\approx f(\tau)\left[2\sqrt{\delta} - \frac{2}{3}\delta^{3/2}\right] - \frac{df}{d\tau}\left[\frac{2}{3}\delta^{3/2} - \frac{2}{5}\delta^{5/2}\right] \tag{4-67}$$

where powers of δ greater than 3/2 have been ignored.

All the integrals in (4-65) can be treated in this way, and after some rearrangement, the final result used in the numerical calculation is

$$\frac{m'}{\bar{m}}(\tau)\left[1 - \frac{\sigma_1+\sigma_2}{\sqrt{\pi}}\left(2\sqrt{\delta} - \frac{2}{3}\delta^{3/2}\right) + \sigma_1\sigma_2\delta\right]$$

$$= \int_0^{\tau-\delta} \frac{m'}{\bar{m}}(\xi)\left[\frac{\sigma_1+\sigma_2}{\sqrt{\pi(\tau-\xi)}} - \sigma_1\sigma_2\right]e^{-(\tau-\xi)}\,d\xi$$

$$+ 2nAB\int_0^{\tau-\delta} \frac{p'}{p}(\xi)\left[\frac{1}{\sqrt{\pi(\tau-\xi)}} + 1\right]e^{-(\tau-\xi)}\,d\xi \tag{4-68}$$

$$+ \left\{-\frac{\sigma_1+\sigma_2}{\sqrt{\pi}}\,\frac{2}{3}\delta^{3/2}\,\frac{d}{d\tau}\left(\frac{m'}{\bar{m}}\right) + \frac{p'}{p}(\tau)\left[\frac{2nAB}{\sqrt{\pi}}\left(2\sqrt{\delta} - \frac{2}{3}\delta^{3/2}\right) + 2nAB\delta\right]\right.$$

$$\left. - \frac{2}{3}\,\frac{2nAB}{\sqrt{\pi}}\,\delta^{3/2}\,\frac{d}{d\tau}\left(\frac{p'}{p}\right)\right\}$$

The accuracy of this formula has been checked by examining several special cases which can be worked out exactly (see Appendix A).

The result (4-68) contains, in addition to the pressure index n, two parameters, A and B. Over rather broad ranges, they can be chosen independently. Previous experience has shown that A is probably in the range $5 < A < 50$ while $B < 1$. This constraint on B assures (see Ref. 60) that heat conduction to the solid from the gas is positive. However, A and B cannot be set entirely independently for the following reason. Both (4-61) and (4-68) produce a response, $m'/\bar{m}$, which consists of transient oscillations and a long-time "steady-state" behavior. It is necessary, for acceptable solutions, that the transients decay. This condition is met if and only if A and B satisfy the inequality[59].

$$A < \frac{B+1}{(B-1)^2} \tag{4-69}$$

One would like to choose A and B to match the dynamical behavior of the particular propellant used. In principle, data taken in T-burners, for example, should provide adequate basis. However, the available experimental results are limited. Hence one is forced to make crude estimates. One aid in this respect is the result[59] that the response to harmonic oscillations exhibits a peak occurring approximately at the value of dimensionless frequency, Ω,

$$\Omega_{peak} \approx A\sqrt{B} \tag{4-70}$$

4.3 Velocity Coupled Response

At the present time, the probelm of velocity coupling is unsolved. There is little question that the burning of a propellant will respond to disturbances of the velocity parallel to the surface. For steady-state burning this is called erosivity. One simple and commonly used representation of this effect is the modified form of the formula for the burning rate given by (3-5). Under unsteady conditions, visual observations, particularly of metallized propellants, suggest that the behavior is likely to much more complicated. Consequently, the simple response function based on unsteady heat conduction in the solid is probably not an accurate representation of the behavior. Additional time lags associated with processes at the interface between the solid and the gas, and possibly in the gas phase itself, are probably important.

Unfortunately, no quantitative information about those processes is available. For the purposes here, then, a very simplified approach is taken. It is assumed that the transient behavior is due solely to the unsteady thermal conduction in the solid phase. While this approximation may not adequately model the total response of real propellants, there is little reason to doubt that the thermal wave must be present in any case. An assessment of the importance of the thermal wave response relative to the complete velocity coupled response of a propellant must await further study.

This does not mean that the response to velocity coupling will be either qualitatively or quantitatively similar to that for pressure coupling. The reason for this is that velocity coupling is intrinsically non-linear, a point which has been emphasized in Refs. 27-31. This non-linearity arises because the burning is sensitive to the magnitude but not the direction of the velocity parallel to the surface. It is therefore independent of details of the physical processes and is always present. This is essentially the only feature peculiar to velocity coupling which has been discussed quantitatively in the literature. In the present work, the intent is to obtain numerical results for comparison with results obtained for pressure coupling. The latter is of course treated here as a purely linear phenomenon.

In view of the above remarks, and with appeal to the discussions of Refs. 27-31, the response of the mass flux to transient disturbances of velocity parallel to the surface is written, by analogy with the result (4-34) for pressure coupling, as

$$\frac{m'}{\bar{m}} = \frac{n_v A B_v}{\lambda + \frac{A}{\lambda} - (1+A) + A B_v} \left\{ \epsilon_1 (|u| - u_t) - \epsilon_2 (\bar{u} - u_t) \right\} \quad (4\text{-}71)$$

Here u_t is the threshold velocity. If has been introduced in previous work as a result of experimental observations on steady burning which have shown that the effect of erosion on the burning rate appears in some cases to be absent unless the parallel velocity u is larger than some value u_t. The quantities ϵ_1 and ϵ_2 are defined as follows:

$$\epsilon_1 = \begin{Bmatrix} 0 & |u| < u_t \\ 1 & |u| > u_t \end{Bmatrix}$$
$$\epsilon_2 = \begin{Bmatrix} 0 & |\bar{u}| < u_t \\ 1 & |\bar{u}| > u_t \end{Bmatrix} \tag{4-72}$$

The subscript ()v on n and B is used to indicate that the values of these parameters may differ from those for pressure coupling. In the limit $\omega \to o$ - i.e. a step change of u is imposed - Equation (4-71) becomes

$$\frac{\delta m}{\bar{m}} = n_v \, \delta(|u| - u_t) \tag{4-73}$$

The change of course, is all in $|u|$; u_t is held constant. If the threshold velocity is introduced in (3-5), the linearized form gives

$$\frac{\delta r}{\bar{r}} \equiv \frac{\delta m}{\bar{m}} = n \frac{\delta p}{\bar{p}} + \frac{C_k^*}{1+C_k^*(|u|-u_t)} \delta(|u|-u_t) \tag{4-74}$$

Comparison of (4-73) and (4-74) shows that the correct limit is obtained only if the parameter n_v is given by

$$n_v = \frac{C_k^*}{1 + C_k^* (|\bar{u}| - u_t)} \tag{4-75}$$

It obvious that for velocity coupling alone, the formula (4-68) can be used to compute the transient mass flux, but with n replaced by n_v, B by B_v and $\frac{p'}{\bar{p}}$ by $\epsilon_1 (|u| - u_t) - \epsilon_2 (|\bar{u}| - u_t)$.

When pressure and velocity coupling are accounted for simultaneously, and they are assumed to be additive, the transform of the mass flux is given by

$$\frac{m'}{\bar{m}} = \frac{nAB}{\lambda + \frac{A}{\lambda} - (1+A) + AB} \frac{p'}{\bar{p}} + \frac{n_v AB_v}{\lambda + \frac{A}{\lambda} - (1+A) + AB_v} \left\{ \epsilon_1 (|u|-u_t) - \epsilon_2 (\bar{u}-u_t) \right\} \tag{4-76}$$

The total transient burning response can then be calculated as

$$\frac{m'}{\bar{m}} = \left(\frac{m'}{\bar{m}}\right)_p + \left(\frac{m'}{\bar{m}}\right)_v \tag{4-77}$$

where $\left(\frac{m'}{\bar{m}}\right)_p$, the pressure coupled response, is calculated from equation (4-68), and $\left(\frac{m'}{\bar{m}}\right)_v$ the velocity coupled response is similarly calculated by making the proper substitutions (indicated previously) in equation (4-68).

5. BOUNDARY CONDITIONS

5.1 Head End - x = 0

The boundary conditions at x = 0 assume the head end is rigid. The boundary condition for the gas phase is then,

$$x = 0 \qquad u = 0 \tag{5-1}$$

The "correct" boundary condition for the particles at the head end would have to allow for particles colliding with the wall. The collision could be assumed to be completely elastic, inelastic, or anywhere in-between. However, if particles were allowed to bounce off the wall, there would clearly exist two classes of particles at locations near the end wall; those that were approaching the wall, and those that had already been reflected. The existence of particles having different velocities at the same location is not compatible with the assumptions underlying the two-phase flow analysis, as outlined in Section 3.1, and, hence, cannot be accommodated in the present model. With this in mind the particle boundary condition has been simply taken to be,

$$x = 0 \qquad u_p = 0 \tag{5-2}$$

This approximation should not seriously affect the overall solution.

5.2 End of the Grain - x = 1

The boundary condition at the end of the grain (x = 1, in the non-dimensional coordinate system) is approximated as follows. In rocket motors with short nozzles the convective derivatives, $u \frac{\partial}{\partial x}$, are much larger than the time derivatives, $\frac{\partial}{\partial t}$, in the flow field between the end of the grain and the throat. A quasi-steady approximation for the flow in this region should, therefore, be a reasonably good approximation.

While it is possible to obtain an "exact" one-dimensional two-phase nozzle solution,[65] the "fractional-lag" approximation[65,66] has been shown to yield very good results, and is much simpler. The fractional lag

analysis is based on the usual two phase flow assumptions (see Section 3.1), with one important difference. It is assumed that the particle velocity and temperature are constant fractions of the gas velocity and temperature, respectively.

$$\frac{u_p^*}{u_g^*} = K \qquad \frac{T_F^* - T_p^*}{T_F^* - T_g^*} = \frac{1 - T_p}{1 - T_g} = L \tag{5-3}$$

It can then be shown that

$$L = [1 + 3\ Pr\ C(1-K)/K]^{-1} \tag{5-4}$$

where Pr is the gas Prandtl number and C is the ratio of particle to gas specific heat.

The fractional lag assumption allows the one-dimensional two-phase equations of motion to be reduced to the one-dimensional isentropic equations for a perfect gas with altered properties. If $\dot{m} = \rho uA$ and $\dot{m}_p = \rho_p u_p A$ are the mass flow rates of the gas and particles, respectively, at the end of the grain, then the fractional lag analysis yields the following for the equivalent isentropic exponent, $\bar{\gamma}$.

$$\bar{\gamma} = 1 + (\gamma - 1)\ \frac{B}{E} \tag{5-5}$$

where,

$$B = \frac{1 + \frac{\dot{m}_p}{\dot{m}} K^2}{1 + \frac{\dot{m}_p}{\dot{m}} CL} \tag{5-6}$$

$$E = 1 + \frac{\dot{m}_p}{\dot{m}} \left\{K[\gamma(1-K) + K] + (\gamma - 1)\ CLB\right\} \tag{5-7}$$

and the equivalent Mach number, $\overline{M}$, is given by[+]

$$\overline{M} = E^{1/2} M \tag{5-8}$$

The value of the lag parameter, K, must, in practice, be determined iteratively. The following expression for K may be obtained[65],

$$K = -\frac{\Phi + (\Phi^2 + 4\Phi)^{1/2}}{2} \tag{5-9}$$

where

$$\Phi = \frac{9}{2}\left[\frac{\mu}{\rho_m \sigma^2 u}\right]\left[\frac{(\overline{\gamma}+1) A_t R}{2\pi}\right]^{1/2} \tag{5-10}$$

and R is the nondimensional throat radius of curvature, $R = R_t/r_t$. In order to find K from equation (5-9) $\overline{\gamma}$ must be known. However, equation (5-5) shows that K must be known to find $\overline{\gamma}$. The establishment of compatible K and $\overline{\gamma}$ values requires iteration.

Once the values of K and $\overline{\gamma}$ have been established the Mach number at the end of the grain is then found by solving the usual isentropic equation for Mach number as a function of area ratio.

$$\left[\frac{A_e}{A^*}\right]^2 = \frac{1}{\overline{M}_e^2}\left[\frac{2}{\overline{\gamma}+1}\left(1 + \frac{(\overline{\gamma}-1)}{2}\overline{M}_e^2\right)\right]^{\frac{\overline{\gamma}+1}{\overline{\gamma}-1}} \tag{5-11}$$

[+]The fractional lag analysis yields the choking condition, $\overline{M}_t = 1$, i.e., the Mach number of the "equivalent" perfect gas is unity at the physical throat. The actual gas Mach number does not reach unity until some point downstream of the throat.

The actual gas Mach number at the end of the grain is then

$$M_e = \frac{u_e}{a_e} = E^{-1/2} \overline{M}_e \tag{5-12}$$

The boundary condition at x = 1 is then, that the gas Mach number be equal to that given by equation (5-12). This matching condition assures that the flow will properly choke at the throat (at least within the confines of the present assumptions of one-dimensional quasi-steady nozzle flow with constant fractional lag). The treatment of the nozzle flow and boundary condition at the end of the grain, as presented, is a simplified and approximate one; but one which should give a fair representation of the actual flow. If, after further study, it can be deduced that a more accurate treatment of the nozzle is required, it will not be inordinately difficult to do so.

6. INITIAL CONDITIONS--STEADY STATE SOLUTION

In order to initiate the method of characteristics instability solution, the steady state equations of motion must be solved. The initial conditions are then generated by adding a perturbation to the steady state solution.

6.1 Steady State Equations in Conservative Form

The steady state two-phase analysis assumes that the mass added to the chamber (from propellant burning) is at constant enthalpy and has no axial momentum. The rate of particle mass addition is taken to be a constant fraction of the gas phase mass addition rate. In addition, the typical two-phase flow assumptions are made, i.e., the particles are spheres of a single size with uniform internal temperature, the particles do not interact with each other and are of negligible volume, etc. With these assumptions the steady state equations may be obtained from the time dependent equations (Section 3.2) by removing the time derivatives. The gas phase equations become:

Continuity: $$\frac{d}{dx^*}(\rho^* u^* A^*) = \omega^* A^* \tag{6-1}$$

Momentum: $$\frac{d}{dx^*}(\rho^* u^{*2} A^*) = -A^* \frac{dP^*}{dx^*} + F_P^* A^* \tag{6-2}$$

Energy: $$\frac{d}{dx^*}\left[\rho^* u^* (C_p T^* + 1/2\, u^{*2}) A^*\right] = \omega^* C_p T_F^* + F_P^* (u_p^* - u^*) A^* + Q_p^* A^* \tag{6-3}$$

State: $$P^* = \rho^* R T^* \tag{6-4}$$

Many times it is advantageous to work with the equations of motion in conservative form. Equations (6-1) and (6-3) are already in conservative form and equation (6-2) may be written in this form as

$$\frac{d}{dx^*}\left[(P^* + \rho^* u^{*2})A^*\right] = F_p^* A^* + P^* \frac{dA^*}{dx^*} \tag{6-5}$$

The particle equations are already in conservative form and are:

Continuity: $$\frac{d}{dx^*}(\rho_p^* u_p^* A^*) = \omega_p^* A^* \tag{6-6}$$

Momentum: $$\frac{d}{dx^*}(\rho_p^* u_p^{*2} A^*) = - F_p^* A^* \tag{6-7}$$

Energy: $$\frac{d}{dx^*}\left[\rho_p^* u_p^*(C_s^* T_p^* + \frac{1}{2} u_p^{*2})A^*\right] = \omega_p^* T_F^* - Q_p^* A^* - F_p^* u_p^* A^* \tag{6-8}$$

6.2 Nondimensional Equations

Using the definitions presented earlier in Section 3.3, the steady state equations can be written in the following nondimensional form (Note: pressure has been eliminated from equation (6-2) using the equation of state (6-4).

$$\frac{d}{dx}(\rho u A) = \omega A \tag{6-9}$$

$$\frac{d}{dx}(\rho_p u_p A) = \omega_p A \tag{6-10}$$

$$\frac{d}{dx}\left[\rho A(T + \gamma u^2)\right] = \gamma A F_p + (\rho T)\frac{dA}{dx} \tag{6-11}$$

$$\frac{d}{dx}(\rho_p u_p^2 A) = - A F_p \tag{6-12}$$

$$\frac{d}{dx}\left[\rho u A\left(T + \frac{\gamma-1}{2} u^2\right)\right] = \left[\omega + (\gamma-1)F_p(u_p - u) + Q_p\right]A \tag{6-13}$$

$$\frac{d}{dx}\left\{\rho_p u_p A\left[C T_p + \left(\frac{\gamma-1}{2}\right) u_p^2\right]\right\} = \left[\omega_p C - (\gamma-1)F_p u_p - Q_p\right]A \tag{6-14}$$

Equations (6-9 to 14) represent six simultaneous first order differential equations which can be conveniently integrated, since they are of the form

$$\frac{df_i}{dx} = g_i \qquad (i = 1 \ldots 6) \tag{6-15}$$

where

$$f = \begin{bmatrix} \rho u A \\ \rho_p u_p A \\ \rho A(T + \gamma u^2) \\ \rho_p u_p^2 A \\ \rho u A \left[T + \frac{(\gamma-1)}{2} u^2\right] \\ \rho_p u_p A \left[C T_p + \frac{(\gamma-1)}{2} u_p^2\right] \end{bmatrix} = \begin{bmatrix} f_1 \\ f_2 \\ f_3 \\ f_4 \\ f_5 \\ f_6 \end{bmatrix} \tag{6-16}$$

and

$$g = \begin{bmatrix} \omega A \\ \omega_p A \\ \gamma A F_p + \rho T \frac{dA}{dx} \\ -A F_p \\ [\omega + (\gamma-1) F_p (u_p - u) + Q_p] A \\ [\omega_p C - (\gamma-1) F_p u_p - Q_p] A \end{bmatrix} = \begin{bmatrix} g_1 \\ g_2 \\ g_3 \\ g_4 \\ g_5 \\ g_6 \end{bmatrix} \tag{6-17}$$

Equations (6-9 to 14) in the form of (6-15) are integrated using an Adams-Moulton integration routine. At each step the solution yields new values for the f's (6-16), and the flow variables themselves must then be calculated so the g's (6-17) can be reevaluated, and the integration continued. With the f_i known the flow variables may be calculated as follows:

$$u_p = \frac{f_4}{f_2}$$

$$\rho_p = \frac{f_2^2}{Af_4}$$

$$T_p = \frac{1}{C}\left[\frac{f_6}{f_2} - \left(\frac{\gamma-1}{2}\right)\left(\frac{f_4}{f_2}\right)^2\right]$$

(6-18)

$$u = \left(\frac{1}{\gamma+1}\right)\frac{f_3}{f_1}\left[1 - \left(1 - 2(\gamma+1)\frac{f_5 f_1}{f_3^2}\right)^{1/2}\right]$$

$$T = \frac{f_5}{f_1} - \frac{(\gamma-1)}{2}u^2$$

$$\rho = \frac{f_1}{uA}$$

The steady state equations are integrated from x = 0 to x = 1, (the end of the grain) where the gas Mach number must be matched to that of the nozzle solution to insure the choked flow condition is satisfied.

As discussed in Section 5.2, the fractional lag two phase nozzle solution establishes the Mach number at the end of the grain, M_e, once the nozzle radius of curvature chamber to throat area ratio, chamber temperature and particle to gas weight flow ratio have been selected.

Successive solutions with varying values of chamber pressure, P_F, are then carried out until the value of M_e predicted by the steady state chamber solution matches the value set by the fractional lag solution. In other words, varying the chamber pressure varies the amount of mass addition into the chamber through the pressure dependence of the solid propellant burning rate until the mass flow required to choke the nozzle is achieved.

7. NUMERICAL SOLUTION

The longitudinal combustion instability model developed in the previous sections has led to a set of nonlinear partial differential equations, which are coupled to the integral equation for the transient burning response. In general, closed form solutions to this set of equations cannot be obtained without resort to further approximation. Therefore, numerical techniques have been employed in order to obtain instability solutions without additional simplification of the model.

The numerical solution of the total problem is made up of several distinct elements; the characteristics equations, transient burning rate equation, and steady state equations. Each of these is individually discussed, in turn, in the remainder of this section.

7.1 Method of Characteristics

The one dimensional unsteady equations of motion are hyperbolic, and, therefore, are amenable to solution via the method of characteristics. The method of characteristics is itself, in the broad sense, a standard numerical method, however, the details of its application to a particular problem can, and do, vary over a considerable range. Each application, and set of equations, is subject to its own little innuendos, which should be taken into account in the formulation of a finite difference analog to the equations. The modified Euler method is the one most frequently employed in method of characteristic solutions. Prior experience with problems of the present type, however, indicates that it is preferable to handle the streamline characteristics in an implicit manner. This allows larger step sizes to be used, and higher gradients can be tolerated without deleterious effects.

The actual solution of the present problem consists of the repeated application of three types of calculations:

1. Field Points
2. Right Boundary Points
3. Left Boundary Points

Each of these calculations is described, in detail, below.

7.1.1 Field Points

A field point is created by the intersection of left running and right running characteristic lines. By definition, it cannot lie on one of the boundaries, since at a boundary one of the characteristic families is absent. Figure 7-1 shows how the finite difference mesh for a field point is created. Although higher order methods, involving more points, can, and have, been used, the usual characterisitc mesh, as shown, utilizes information at two adjacent points to solve for the flow variables at a third point, more advanced in time. Here, it is assumed that all required information is known at points 1 and 2, and the solution at point 3 is to be sought.

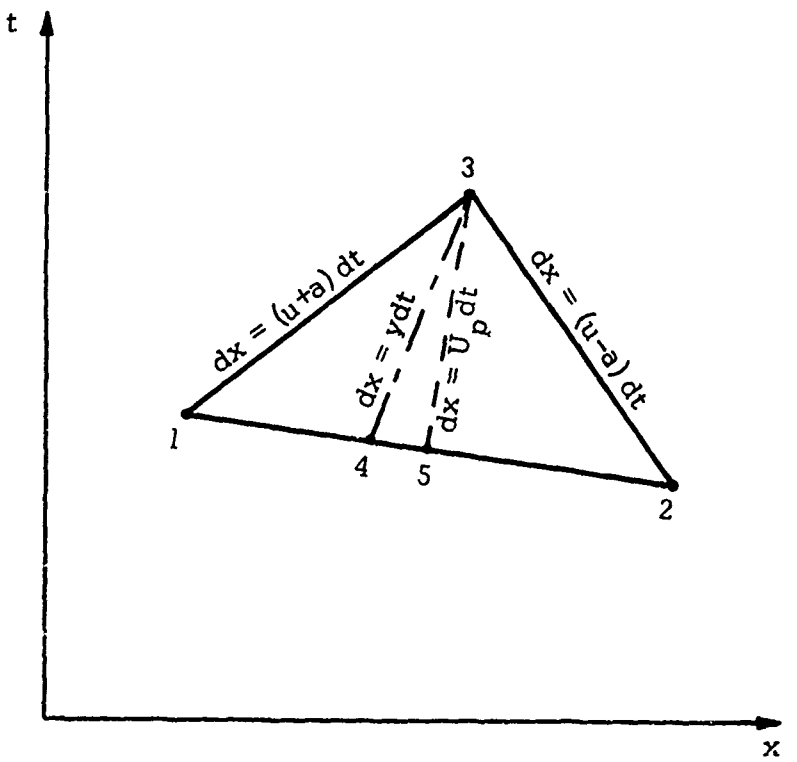

Figure 7-1. Field Point Calculation

In the present scheme, the solution is begun by assigning the flow variables at point 3 values equal to the average of their values at points 1 and 2. Using equation (3-32) for the directions of the characteristic lines, the location of point 3 yields,

$$t_3 = \frac{c^+ t_1 - c^- t_2 + x_2 - x_1}{c^+ - c^-} \tag{7-1}$$

$$x_3 = x_1 + c^+(t_3 - t_1) \tag{7-2}$$

where the average slopes of the characteristic lines are (the plus and minus signs are used to denote right and left running characteristics, respectively),

$$\begin{aligned} c^+ &= [(u_1 + a_1) + (u_3 + a_3)]/2 \\ c^- &= [(u_1 - a_1) + (u_3 - a_3)]/2 \end{aligned} \tag{7-3}$$

Average values of u, ρ, T, ω, a, etc., along each of the characteristics, are then defined, e.g.,

$$\begin{aligned} u^+ &= (u_1 + u_3)/2 \\ u^- &= (u_1 + u_2)/2 \end{aligned} \tag{7-4}$$

This enables the compatibility relations, equations (3-33) and (3-34) to be written as

$$G^+ \frac{(P_3 - P_1)}{(t_3 - t_1)} + \frac{(u_3 - u_1)}{(t_3 - t_1)} = RHS^+ \tag{7-5}$$

$$G^- \frac{(P_3 - P_2)}{(t_3 - t_2)} - \frac{(u_3 - u_2)}{(t_3 - t_2)} = RHS^- \tag{7-6}$$

where RHS^+ and RHS^- are the right hand sides of equations (3-33) and (3-34), respectively, evaluated in terms of the corresponding average values of the variables, e.g.,

$$RHS^+ = -\frac{a^+}{A^+}\left[\frac{1}{\gamma}\frac{\partial A}{\partial t}\Big|_{x^+,t^+} + u^+\frac{\partial A}{\partial x}\Big|_{x^+,t^+}\right] + \frac{\omega^+}{\rho^+ a^+}\left[(1-u^+a^+)\right.$$

$$\left. + \frac{(\gamma-1)}{2}u^{+2}\right] + \frac{F_p^+}{\rho^+ a^+}\left[(\gamma-1)(u_p^+ - u^+) + a^+\right] + \frac{Q_p^+}{\rho^+ a^+} \tag{7-7}$$

and

$$G^+ = (\gamma\,\rho^+ a^+)^{-1}$$

$$G^- = (\gamma\,\rho^- a^-)^{-1} \tag{7-8}$$

Equations (7-5) and (7-6) are easily solved to yield the pressure and velocity at point 3

$$P_3 = \frac{G^+P_1 + G^-P_2 + u_1 - u_2 + RHS^+\,\Delta t^+ + RHS^-\Delta t^-}{G^+ + G^-} \tag{7-9}$$

$$u_3 = u_1 - G^+(P_3 - P_1) + RHS^+\,\Delta t^+ \tag{7-10}$$

Since the burning rate ω, is only pressure and/or velocity dependent, its value at point 3 could now be calculated, in principle. In practice, the complexity of the transient burning rate analysis precludes it, from an economic standpoint. The burning rate analysis is used to calculate ω only after the completion of all the characteristics calculations for two or more time levels. When burning rate values are calculated at other times, they are done so by simple first order extrapolation from previous results.

The temperature at point 3 is found by utilizing the compatibility relation (equation (3-37)), along the gas streamline, $dx/dt = u$, (shown as line segment $\overline{3-4}$ in Figure 7-1). The intersection of the gas streamline passing through point 3 and the line segment joining points 1 and 2, shown as point 4, is not known, a priori, and must be located. The slope of the streamline is taken to be the average of u_3 and u_4*, hence, the location of point 4 is found to be

$$x_4 = \left[t_3 - t_1 + x_1 \frac{(t_2 - t_1)}{(x_2 - x_1)} - \frac{x_3}{.5(u_3 + u_4)}\right]\left[\frac{(t_2 - t_1)}{(x_2 - x_1)} - \frac{1}{.5(u_3 + u_4)}\right]^{-1} \tag{7-11}$$

$$t_4 = t_3 + \frac{(x_4 - x_3)}{.5(u_3 + u_4)} \tag{7-12}$$

All of the flow variables at point 4 may now be evaluated by lineraly interpolating between points 1 and 2. Average quantities, denoted by a $\overline{(\ )}$, are defined based on the values at points 3 and 4. As mentioned earlier, the solution of the streamline characteristics is carried out "implicitly". Here the term "implicit" is used to denote the fact that the temperature derivative in equation (3-37) is not evaluated strictly in terms of known quantities. Rather, the temperature on the right hand side is approximated as (T_3 (the current unknown)$+T_4)/2$. This has the effect of coupling the value of the derivative to the value of the variable, itself, and helps to prevent wild over or under-prediction. In the manner discussed above, the solution for T_3 is found to be

$$T_3 = \frac{[\bar{\rho} - \frac{1}{2}\bar{\omega}(t_3 - t_4)]\,T_4 + \frac{(\gamma-1)}{\gamma}(P_3 - P_4) + \overline{RHS}}{\bar{\rho} + .5\,\bar{\omega}(t_3 - t_4)} \tag{7-13}$$

*On the first iteration, u_4 is set equal to $(u_1 + u_2)/2$; a good approximation when the velocity is small.

where $\overline{RHS}$ is defined as

$$\overline{RHS} = (t_3 - t_4)\left[\frac{(\gamma-1)}{\gamma}\ \frac{\bar{P}}{\bar{A}}\ \frac{\partial A}{\partial t}\Big|_{\bar{x},\bar{t}} + \bar{\omega}\left[1+\tfrac{1}{2}(\gamma-1)\,\bar{u}^2\right] + (\gamma-1)\,\bar{F}_p(\bar{u}_p - \bar{u}) + \bar{Q}_p\right] \tag{7-14}$$

The sound speed can then be found as

$$a_3 = \sqrt{T_3} \tag{7-15}$$

and the equation of state yields

$$\rho_3 = \frac{P_3}{T_3} \tag{7-16}$$

The particle velocity and temperature at point 3 are found from the particle pathline characteristic (equation (3-38)) and its dual compatibility relations (equations (3-40) and (3-41)) in a manner essentially identical to the solution for T_3. In this case, the intersection of the particle pathline through point 3 and $\overline{1-2}$, shown as point 5, is located. Values at point 5 are established by interpolation and averages of the variables at 5 and 3 are defined (denoted by a subscript av). The solutions for u_{p_3} and T_{p_3} were also done "implicitly."

The equations for x_5 and t_5 may be obtained by simply changing all the 4's to 5's in equations (7-11) and (7-12), and are not given here. The final equations for u_{p_3} and T_{p_3} are easily shown to be

$$u_{p_3} = \frac{\rho_{p_{av}}\, u_{p_5} - (\tfrac{1}{2}\,\omega_{p_{av}}\, u_{p_5} + F_{p_{av}})(t_3 - t_5)}{\rho_{p_{av}} + \tfrac{1}{2}\,\alpha_{p_{av}}\,(t_3 - t_5)} \tag{7-17}$$

$$T_{p_3} = \frac{\left[\rho_{p_{av}} - \frac{1}{2}\omega_{p_{av}}(t_3-t_5)\right]T_{p_5} + (t_3-t_5)\left[\omega_{p_{av}}\left[1+\frac{(\gamma-1)}{2C}\left(\frac{u_{p_3}+u_{p_5}}{2}\right)^2\right] - \frac{Q_{p_{av}}}{C}\right]}{\rho_{p_{av}} + \frac{1}{2}\omega_{p_{av}}(t_3-t_5)} \tag{7-18}$$

It will be recalled that lacking a state equation for the particles, the equation for ρ_p cannot be put into characteristic form. The equation for ρ_p may be written as (see (3-42))*

$$\frac{\delta_p \delta_p}{\delta t} = \omega_p - \delta_p \frac{\partial u_p}{\partial x} \tag{7-18}$$

wherein the velocity derivative is treated as an ordinary variable, and is placed on the right hand side. In the form shown, equation (7-18) is analogous to the compatibility relations, equations (3-40) and (3-41), and ρ_{p_3} may be found in the manner previously outlined for velocity and temperature, provided a suitable approximation can be found for the velocity derivative.

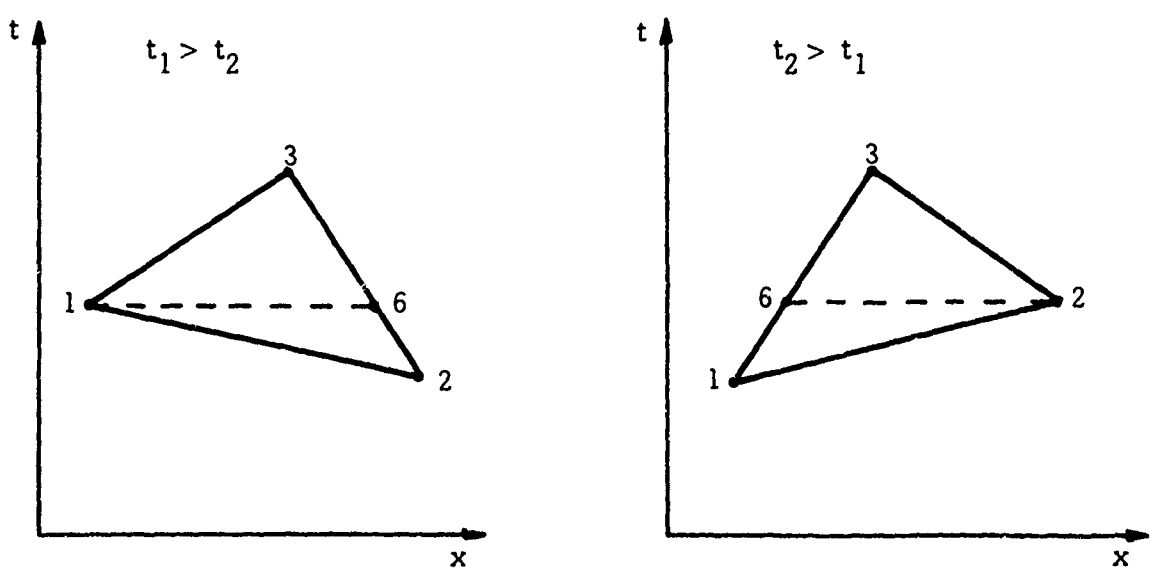

Figure 7-2. Calculation of $\partial u_p/\partial x$

*The area derivative term has been left out of the numerical analysis at this point. If varying area solutions are sought in the future the solution for ρ_p, shown here, will have to be modified.

A first order method for calculating $\frac{\partial u_p}{\partial x}$ has been devised, as follows: Depending on whether $t_2 >$ or $< t_1$ (see Figure 7-2) a new point, 6, is located; along $\overline{2-3}$ at t_1, if $t_1 > t_2$, or along $\overline{1-3}$ at t_2, if $t_2 > t_1$. The velocity at point 6 is found by linear interpolation and is

$$u_{p_6} = u_{p_2} + \frac{(t_1 - t_2)}{(t_3 - t_2)} (u_{p_3} - u_{p_2}) \qquad t_1 > t_2$$

$$u_{p_6} = u_{p_1} + \frac{(t_2 - t_1)}{(t_3 - t_1)} (u_{p_3} - u_{p_1}) \qquad t_2 > t_1 \tag{7-19}$$

The location of point 6, itself, is given by

$$x_6 = x_2 + c^-(t_1 - t_2) \qquad t_1 > t_2$$

$$x_6 = x_1 + c^+(t_2 - t_1) \qquad t_2 > t_1 \tag{7-20}$$

and the velocity derivative can then be approximated as

$$\frac{\partial u_p}{\partial x} = \frac{u_{p_6} - u_{p_1}}{x_6 - x_1} \qquad t_1 > t_2$$

$$\frac{\partial u_p}{\partial x} = \frac{u_{p_2} - u_{p_6}}{x_2 - x_6} \qquad t_2 > t_1 \tag{7-21}$$

The density, ρ_{p_3}, can now be found from equation (7-18),

$$\rho_{p_3} = \frac{\rho_{p_5} + \left[\omega_{p_{av}} - \frac{1}{2}\rho_{p_5} \frac{\partial u_p}{\partial x}\right](t_3 - t_5)}{\left[1 + \frac{1}{2}(t_3 - t_5) \frac{\partial u_p}{\partial x}\right]} \tag{7-22}$$

At this point, all of the flow variables at point 3 have been found. The whole procedure, from the locating of point 3, to the solution for ρ_{p_3}, is then repeated until satisfactory convergence has been obtained. The tests made to determine whether further iteration is required are based upon the relative change in a_3, ρ_3 and ρ_{p_3} from one iteration to the next. If

$$\frac{a_3^{(i)} - a_3^{(i-1)}}{a_3^{(i)}} < \epsilon_1$$

$$\frac{\rho_3^{(i)} - \rho_3^{(i-1)}}{\rho_3^{(i)}} < \epsilon_1 \qquad (7\text{-}23)$$

and

$$\frac{\rho_{p_3}^{(i)} - \rho_{p_3}^{(i-1)}}{\rho_{p_3}^{(i)}} < \epsilon_2 \qquad (7\text{-}24)$$

are all satisfied, the field point calculation is complete.

7.1.2 Right Hand Boundary

A right hand boundary point is created when a right running characteristic reaches the boundary at the end of the grain, $x = 1$. Since any left running characteristics passing through such a point would have to come from outside the domain of interest the information carried by them is not available. Without the compatibility relation on left running characteristics, one less equation is available; this is compensated for by the right hand boundary condition given by equation (5-12). This boundary condition fixes the Mach number at the end of grain, such that the flow will choke at the throat in a quasi-steady manner.

The finite difference mesh and method of solution for a right hand boundary point are quite similar to that of the field point.

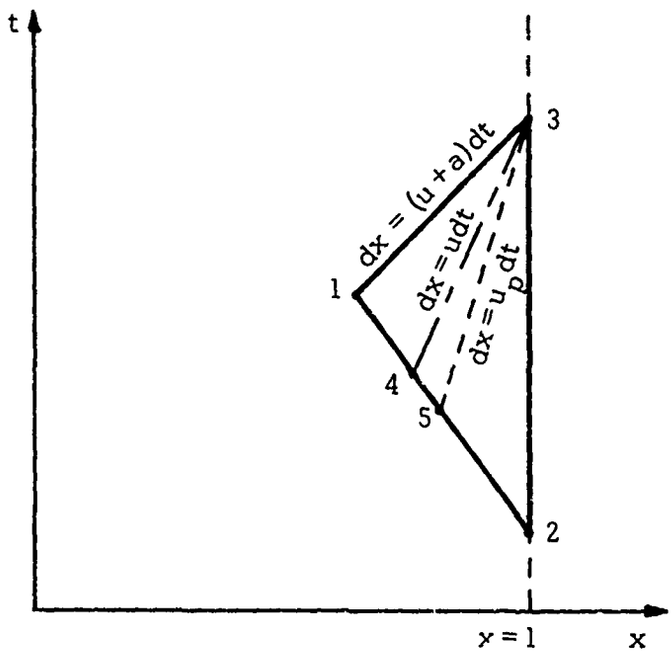

Figure 7-3. Right Hand Boundary Point Calculation

Again, points 1 and 2 are known, and the solution at point 3 is sought. In this case, $x_3 = 1$, is known; and $u_3 = M_e a_3$ must be satisfied. M_e is known from the boundary condition, but a_3 is not known until the energy equation is solved to yield T_3. To begin the solution u_3 and all of the other quantities at point 3 are set equal to the value of the respective variables at point 2. The location of point 3 is found to be

$$x_3 = 1$$

$$t_3 = t_1 + \frac{(x_3 - x_1)}{c^+} \qquad (7\text{-}25)$$

where c^+ is defined in equation (7-3). Proceding in a manner similar to that shown, previously, for the field point, P_3 is found from the compatibility relation on the right running characteristic $\overline{1-3}$.

$$P_3 = P_1 + [RHS^+(t_3-t_1) - (u_3-u_1)]/G^+ \tag{7-26}$$

where RHS^+ and G^+ have been given by equations (7-7) and (7-8).

The calculation of T_3, a_3, ρ_3, u_{p_3}, T_{p_3}, and ρ_{p_3} from the streamline and particle pathlines follows, identically, the procedure outlined for the field point solution. The only additional step is the calculation of u_3, from the boundary condition, after T_3 and, hence, a_3, have been found.

7.1.3 Left Hand Boundary

A left hand boundary point is formed when a left running characteristic intersects the wall, $x = 0$. Like the right hand boundary point calculation, the relation lost through the nonexistence of one characteristic family (here the right running family) is replaced by a boundary condition. In this case, the boundary condition is $u = 0$ at $x = 0$. (See equation (5-1)). As discussed in Section 5.1, an additional boundary condition has also been placed on the particle velocity, i.e., $u_p = 0$ at $x = 0$. As a result of these two conditions the line $x = 0$ is both a streamline and a particle pathline. The fixed location of these lines, in this case, makes the solution somewhat simpler, since the points denoted 4 and 5 in the field point and right hand boundary point calculations need not be established.

The left hand boundary point calculation is initiated by setting the variables at point 3 equal to their respective values at point 1. The location of point 3 is found to be*

$$\begin{aligned} x_3 &= 0 \\ t_3 &= t_2 - \frac{x_2}{c^-} \end{aligned} \tag{7-27}$$

*The program currently allows the left hand boundary to have a velocity, so that piston problems can be analyzed (without particles). This option was used only for program checkout and will not be considered here.

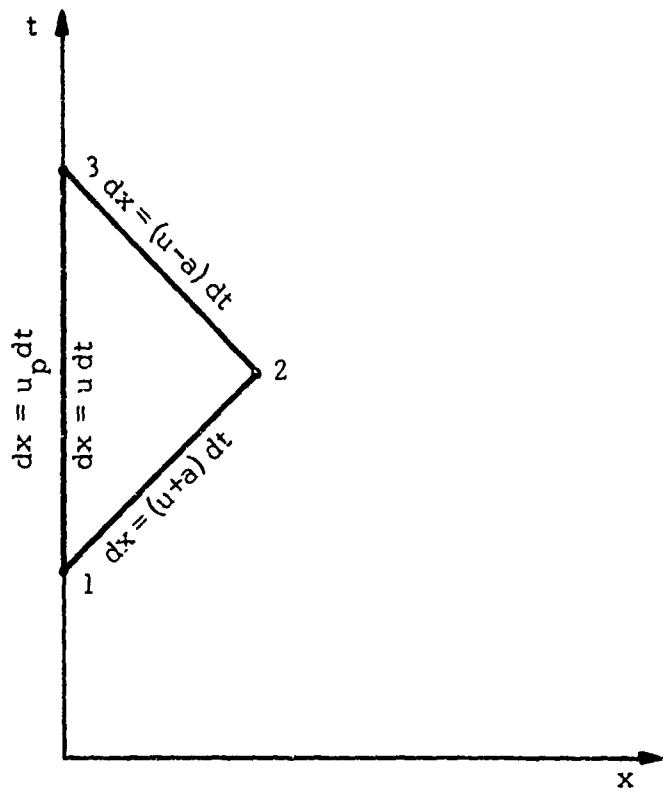

Figure 7-4. Left Hand Boundary Point Calculation

where c^- is defined in equation (7-3). The velocity at point 3, u_3, equals zero, by definition. The pressure can then be found from the compatibility relation for left running characteristics (equation (3-34)), and is

$$P_3 = P_2 + [RHS^-(t_3-t_2) - u_2]/G^- \tag{7-28}$$

where RHS^- can be found by analogy with equation (7-7) and G^- is specified by equation (7-8).

The temperature is found by integrating the gas streamline compatibility relation (3-37) from point 1 to point 3, and is given by

$$T_3 = \frac{\left[\bar{\rho} - \frac{1}{2}\bar{\omega}(t_3-t_1)\right] T_1 + \frac{(\gamma-1)}{\gamma}(P_3-P_1) + (t_3-t_1)\left[\frac{(\gamma-1)}{\gamma}\frac{\bar{P}}{\bar{A}}\frac{\partial A}{\partial t}\Big|_{\bar{x},\bar{t}} + \bar{\omega} + \bar{Q}_p\right]}{\bar{\rho} + \frac{1}{2}\bar{\omega}(t_3-t_1)} \tag{7-29}$$

where $(\bar{\ })$ quantities are based on conditions averaged between points 1 and 3.

The particle velocity, u_{p_3}, has been assumed to be zero, hence, in a similar manner, using equation (3-41), T_{p_3} is found to be

$$T_{p_3} = \frac{[\bar{\rho}_p - \frac{1}{2}\bar{\omega}_p(t_3-t_1)]\, T_{p_1} + (t_3-t_1)[\bar{\omega}_p - \bar{Q}_p/C]}{\bar{\rho}_p + \frac{1}{2}\bar{\omega}_p(t_3-t_1)} \tag{7-30}$$

The particle density is found in the general manner discussed in the field point calculation; however, in this case, a point 6 does not have to be located, since $\partial u_p/\partial x$ can be simply approximated as

$$\frac{\partial u_p}{\partial x} = \frac{u_2}{x_2} \tag{7-31}$$

The value of ρ_{p_3} can be computed from equation (7-22) by replacing the 5's with 1's. Like the other calculations, the left hand boundary point calculation is iterated until equations (7-23) and (7-24) are satisfied.

7.1.4 Ordering of the Calculations

As mentioned earlier, the method of characteristics solution is obtained by the repeated application of the three unit processes previously described; the field point, and right and left hand boundary points. In order to achieve a useful solution, however, a logical method for determining the order in which these calculations are to be performed is required. Several possible ordering schemes are possible, each having certain advantages and disadvantages. The scheme outlined below was selected as being the most appropriate for the problem; all constraints considered.

After a steady state solution has been achieved, an initial perturbation is added to it to generate the initial line, at t = 0, for the characteristics solution. The number of points, M, used on the initial line determines the mesh spacing for the solution. The characteristics solution is initiated by a field point calculation using points 1 and 2. Additional field point calculations are successively carried out until a total of M-1 have been performed, the last one involving points M-1 and M. At the completion of this first stage of the solution the x-t diagram has the form shown in Figure 7-5.

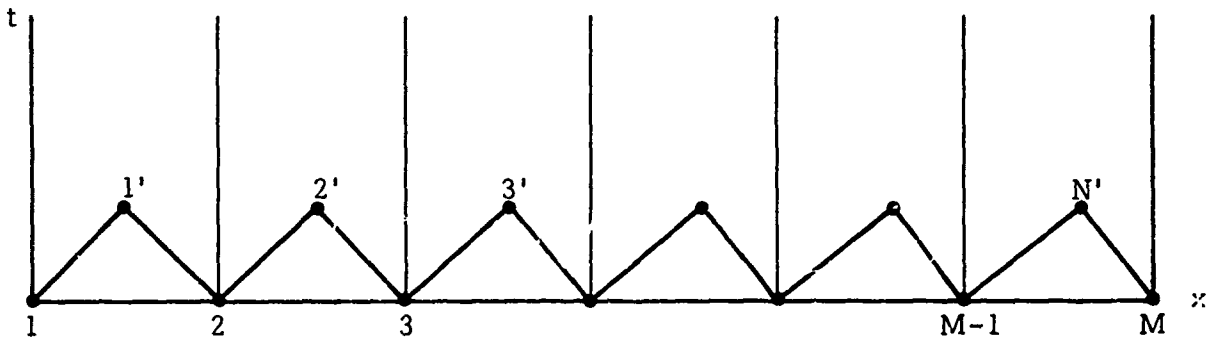

Figure 7-5. x-t Diagram After First Time Step

Another series of field point calculations is then performed using points 1', 2' .. N'(see Figure 7-5). Upon completion, a left hand boundary point calculation is carried out using points 1 and 1', and a right hand boundary point calculation using points N'and M is also performed. At this point the x-t diagram looks like the one illustrated in Figure 7-6.

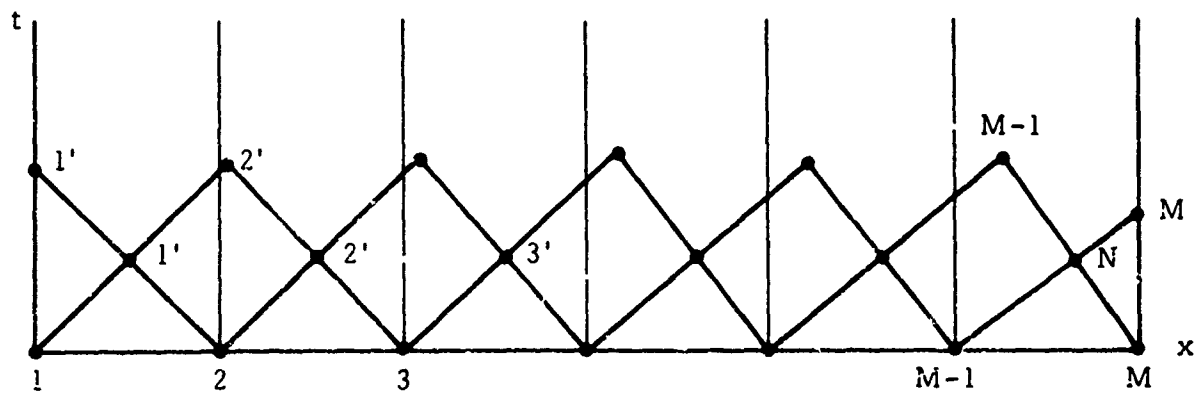

Figure 7-6. x-t Diagram After Two Time Steps (one complete "cycle" of the characteristics calculation)

The features to be noted from this figure are as follows:

1. Except for the new point M (right boundary point), all of the other points (1-(M-1)) have about the same value of time.
2. At the end of these two rounds of calculations the number of points remains the same, however, the locations of the points are somewhat displaced from their original positions.

These features cause the characteristic mesh network to become skewed. The skewness of the network generally becoming worse as time passes. This skewing of the mesh is a normal feature of characteristics solutions, and, as long as it does not become drastic, is not usually a cause for concern. In the present case, however, the skewness is undesirable due to the coupling between the flow and the transient burning rate calculation. The burning rate analysis is one dimensional in that it considers each x location independent of the others, and neglects longitudinal energy transfer. At each x location, however, the transient burning rate is a function of the pressure history at that location, for all time. In order to carry out the burning rate analysis, then, the pressure must be known at specific x locations, not at the somewhat random intervals that result from the usual characteristics mesh. This situation could have been relieved by essentially carrying along two different meshes; the characteristic mesh, and an orthogonal one, obtained by interpolation within the characteristic mesh, having fixed x locations, for use in the burning rate analysis. Such an approach, however, results in large computer storage requirements and an unnecessarily complex code.

The remedy for this problem that was adopted does not require two separate meshes to be carried along. Rather, when the point shown in Figure 7-6 is reached, the mesh is rectified by interpolation; thereby creating a set of points all at the same time, and at the same spacing as on the initial line. This pattern is then repeated until the computation reaches the desired time level. The details of the interpolation procedure are presented in the following section.

7.2 Interpolation - Rectification of the Characteristics Mesh

The interpolation of the characteristics results, in order to obtain a rectilinear mesh, could be carried out to varying degrees of accuracy. It was felt that the increased complexity and computation time associated with higher order interpolation schemes was not warranted since, in many practical cases, their theoretical accuracy advantages are often not realized. Thus linear interpolation has been used throughout.*

The interpolation is performed in the following manner. First, values of the variables at the original x locations are obtained by interpolating along lines connecting the new points 1, 2, ... M. Each of these points (denoted by primes in Figure 7-7) will then, in general, differ only slightly in their time coordinate; except for point M, at the right hand boundary, which usually lags considerably. The "regular" points, i.e., 1, 2, ... M-1, are then searched to determine the one having the smallest value of time, denoted t_{min}.

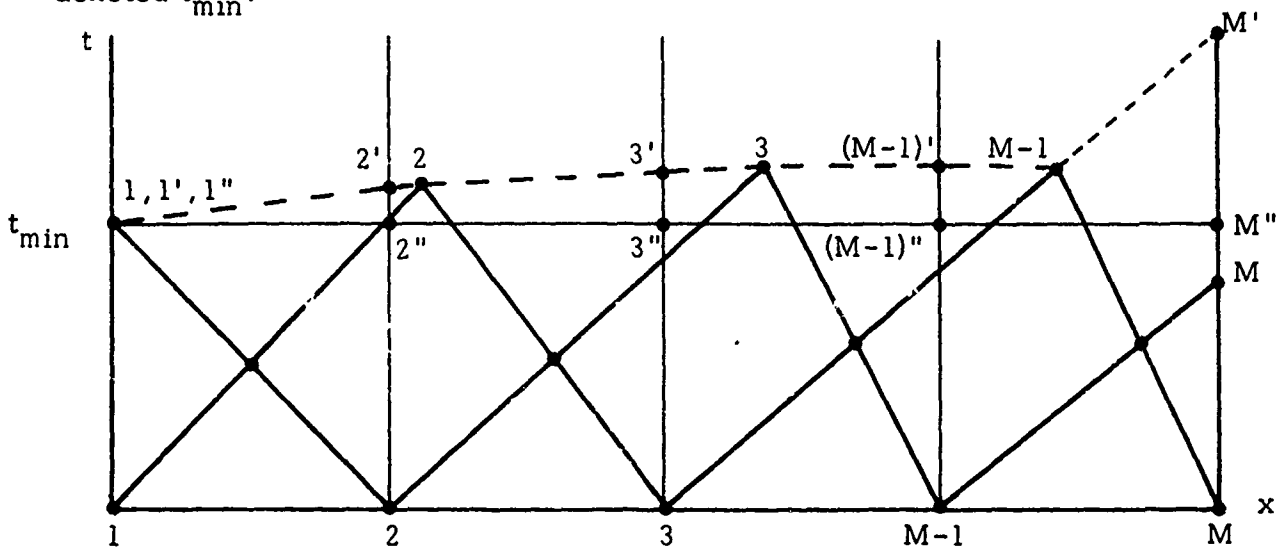

Figure 7-7. Interpolation Diagram For Rectifying the Characteristics Mesh

*The interpolation procedure can affect the accuracy of the results. Test cases with, and without, interpolation, using a quasi-steady burning rate, have been computed and a comparison of the results showed essentially no difference, at the end of 200 time steps. These cases did not have steep-fronted waves; if they did, differences between the solutions would probably have been evident.

This is usually point 1. Interpolation is then performed on each of the x = constant lines to obtain a set of points at the uniform time, t_{min}. These points are denoted by double primes in Figure 7-7. The original differences in the time coordinate are shown greatly magnified in Figure 7-7 so that the procedure may be clearly illustrated. The new right hand boundary point, M'', is established by extrapolation. This could be avoided by solving for an extra "dummy" right hand boundary point (shown as M') using points M and M-1, and then interpolating. This latter procedure is probably somewhat more accurate; however, it has not yet been incorporated into the computer program (and probably will not be unless the extrapolation procedure is found to be seriously lacking).

When the double interpolation procedure is completed the set of points obtained are directly analogous to the original set of points on the initial line, t = 0. The whole computation cycle can then be repeated as many times as desired. In the nondimensional coordinate system employed the points on the initial line are a distance $\Delta x = 1/(M-1)$ apart. It turns out that the time increment for a computational cycle, t_{min} in the illustration, is almost exactly equal to Δx. This result can be used as a rule of thumb to determine how many computation cycles are required to reach a given value of time. It should also be pointed out that since the time step is directly proportional to the spatial increment, the total number of mesh points, and the computation time, for a given problem varies as Δx^2. (If the number of points on the initial line is doubled, the computation time will approximately quadruple). As a consequence of this situation, efforts to optimize the accuracy-mesh size tradeoff are well rewarded.

Incidentally, the interpolation procedure also produces two desirable by-products. First, the randomness of the usual skewed characteristics mesh makes the interpretation of the calculated results difficult. In fact, in many applications the characteristics solution is stored on tape and later processed by a separate interpolation program. Second, the interpolation procedure allows the mesh to advance equally in time across the entire domain of interest. This eliminates the requirement for additional logic to prevent the calculation of points past the desired maximum time in some areas of the mesh, while the remaining portions of the mesh catch up.

7.3 Transient Burning Rate Solution

The interpolation procedure, just described, provides the pressure and velocity histories required for the transiet burning rate calculation. However, before the burning rate expression can be numberically evaluated the derivatives in equation (4-68) must be written in difference form. A simple two step formula is used, which yields the following*

$$\frac{d}{d\tau}\left(\frac{P}{\bar{P}}\right) = \frac{P(\tau) - P(\tau-\delta)}{\delta}$$

$$\frac{d}{d\tau}\left(\frac{m'}{\bar{m}}\right) = \frac{\frac{m'}{\bar{m}}(\tau) - \frac{m'}{\bar{m}}(\tau-\delta)}{\delta} \tag{7-32}$$

Since $m'/\bar{m}(\tau)$ is the unknown being evaluated, the term involving it is brought over to modify the multiplier on the left hand side of equation (4-68). The burning rate expression is also written in terms of the nondimensional time τ (see equation (4-59), the t in this equation is dimensional), while the remainder of the analysis uses the nondimensional time t (equation (3-18)). The two times are related as follows:

$$\tau = \frac{L}{a_f}\,\frac{\bar{r}^2}{4\kappa}\,t = t_c t \tag{7-33}$$

Since $\bar{r}$ is a function of axial distance the relative time constant, t_c, also varies axially. Defining,

$$\begin{aligned}
\delta' &= \delta/t_c \\
C_1 &= \frac{2}{3}(\sigma_1 + \sigma_2)(t_c/\pi)^{\frac{1}{2}} \\
C_2 &= \sigma_1\sigma_2\, t_c \\
C_3 &= 2nAB\, t_c \\
C_4 &= \frac{4}{3}\, nAB(t_c/\pi)^{\frac{1}{2}}
\end{aligned} \tag{7-34}$$

*The details of the solution are worked out only for the pressure coupled case. The calculation of $m'/\bar{m}$ for velocity coupling is essentially identical if n_v, B_v and $\epsilon_1(|u|-u_t) - \epsilon_2(\bar{u}-u_t)$ are used instead of n, B and $p'/\bar{p}$.

and using equations (7-32) and (7-33), the transient burning rate can be expressed in the final form used on the numerical solution.

$$\frac{m'}{\bar{m}}(t) = \left[1 - C_1\sqrt{\delta'}\,(2-t_c\delta') + C_2\delta'\right]^{-1}\left\{\frac{3}{2}C_1\int_0^{t-\delta'}\frac{m'}{\bar{m}}(\xi)\,\frac{e^{t_c(\xi-t)}}{\sqrt{t-\xi}}\,d\xi\right.$$

$$+\frac{3}{2}C_4\int_0^{t-\delta'}\frac{P'}{\bar{P}}(\xi)\,\frac{e^{t_c(\xi-t)}}{\sqrt{t-\xi}}\,d\xi + C_3\int_0^{t-\delta'}\frac{P'}{\bar{P}}(\xi)\,e^{t_c(\xi-t)}\,d\xi \tag{7-35}$$

$$-C_2\int_0^{t-\delta'}\frac{m'}{\bar{m}}(\xi)\,e^{t_c(\xi-t)}\,d\xi + C_1\delta'^{\frac{1}{2}}\frac{m'}{\bar{m}}(t-\delta') + C_4\delta'^{\frac{1}{2}}\frac{P'}{\bar{P}}(t-\delta')$$

$$\left.+\frac{P'}{\bar{P}}(t)\left[C_4\delta'^{\frac{1}{2}}(2-t_c\delta') + C_3\delta'\right]\right\}$$

The first two integrals in (7-35) must be integrated from 0 to the current time, t (actually t-δ'), each time step. As time goes on these integrals take longer and longer to do, and require increasing amounts of computer memory to store all of the required past history.

The second two integrals in equation (7-35) may be written as

$$e^{-t_c t}\left[C_3\int_0^{t-\delta'}\frac{P'}{\bar{P}}(\xi)\,e^{t_c\xi}\,d\xi - C_2\int_0^{t-\delta'}\frac{m'}{\bar{m}}(\xi)\,e^{t_c\xi}\,d\xi\right] \tag{7-36}$$

with their dependence on the parameter t explicitly removed. Hence, these two integrals need not be reevaluated from ξ = 0 each time; rather, a running sum is kept, which is added to at each time step. The latest value of the sum of the two integrals is then multiplied by the pre-exponential factor involving t.

The integrals are currently evaluated using the trapezoidal rule. Numerical tests have confirmed that this simplest of integration formulas yields accurate results for most cases of interest. If cases are encountered for which this method proves inadequate, it would not be too difficult to replace it with a more accurate (but more complex) formula.

7.3.1 Extending the Transient Burning Rate Solution to Long Times

The current method for computing the pressure and velocity coupled transient burning response requires four quantities to be stored at every axial location each time that a calculation is made. These quantities are:

$$\frac{p'}{\bar{p}} \text{ and } \left(\frac{m'}{\bar{m}}\right)_p \tag{7-37}$$

$$\varepsilon_1(|u|-u_t) - \varepsilon_2(\bar{u}-u_t) \quad \text{and} \quad \left(\frac{m'}{\bar{m}}\right)_v$$

As time increases, computer storage requirements will eventually exceed the available core of the computer being utilized. Additionally, as time increases, the burning rate integrals (Eq. 7-35) must be evaluated over longer and longer intervals. This causes the program execution time to increase nonlinearly, i.e. if the final time of the solution is doubled the execution time increases by a factor greater than 2. A method for at least partially ameliorating these drawbacks has been developed, however.

In practice the effect of a disturbance at a given time does not last forever. Its effect on the burning rate should decrease as time goes on, eventually damping out. Thus, one should be able to limit the amount of back history that need be considered. The time interval over which the effect of past disturbances disappears is dependent upon the values of A and B in a rather complex manner. Based on the analytical results, presented in Appendix A, for the special cases of step or experimential pressure changes it can be hypothesized that the effect of a disturbance at a given time, τ_o, should decay exponentially with time at a rate something like $e^{(x^2-y^2-1)(\tau-\tau_o)}$ where

$$\begin{aligned} x &= A(1-B) \\ y &= [4A-(AB-A-1)^2]^{\frac{1}{2}} \end{aligned} \tag{7-38}$$

Figure 7-8 shows the locus of the successive peaks in the transient burning rate response to a pressure disturbance of the form

$$\frac{p'}{\bar{p}} = .1\cos(\pi t) \qquad t \le 3.48 \quad (\tau \le .274)$$
$$\frac{p'}{\bar{p}} = 0 \qquad t > 3.48 \quad (\tau > .274) \tag{7-39}$$

This response was calculated using a small computer program which was developed solely to integrate equation (4-68) for a given pressure variation.

The result shown was obtained with the burning rate parameters A and B equal to 15 and .7 respectively. With these values of A and B $x = 4.5$ and $y = 5.454$, therefore, based on the aforementioned hypothesis it would be expected that the response would die out at a rate like $e^{-10.5\tau}$. The actual response, shown in Figure 7-8, damped, essentially exponentially, at a rate between $e^{-9.5\tau}$ and $e^{-10\tau}$; in relatively good agreement with expectations.

The example just discussed serves to illustrate that the response to a disturbance which occurs at a particular time eventually damps out. Since the current transient burning rate analysis is linear, this feature can be exploited to limit the amount of computer storage required to obtain solutions over long times. By using the principle of superposition the pressure or velocity disturbance history, at a given axial location, can be considered to be the sum of a series of discrete disturbances, each localized in time. The response to a disturbance which exists only from $t = t_1$ to $t = t_2$ will damp out (to within any given tolerance) in some time interval after t_2, denoted Δt_d. The size of this interval being a function of A and B. Thus knowledge of the disturbance which existed between t_1 and t_2 and the subsequent response to it becomes superfluous after a time equal to $t_2 + \Delta t_d$.

Based on this concept, a method for obtaining instability solutions out to as large a time as desired can be constructed, which requires no more storage than would ordinarly be required to compute the solution out to $t = 2\Delta t_d$. The procedure is as follows:

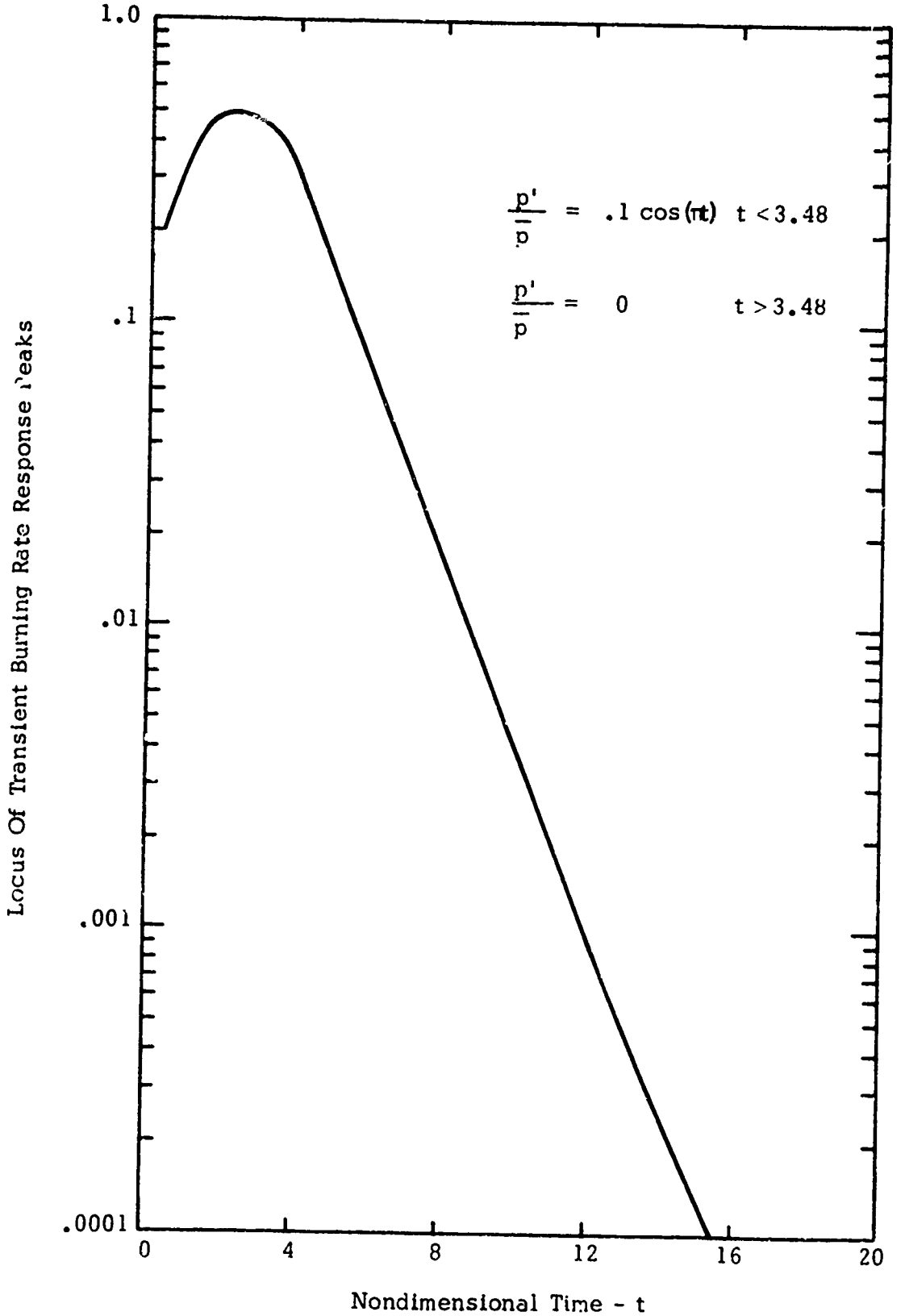

Figure 7-8 Example Of Transient Response Damping Subsequent To The Cutoff Of The Pressure Perturbation.

1. For times less than Δt_d, the burning response is computed in the straightforward manner discussed earlier. This is shown pictorially in Figure 7-9, for the case of a pressure coupled response. (Actually, the disturbance will typically have several cycles in Δt_d, however only one is illustrated).
2. At times between $t = \Delta t_d$ and $t = 2\Delta t_d$ the disturbance history at a given location is divided into two discrete parts (see Figure 7-10). One disturbance beginning at $t = 0$ and ending at $t = \Delta t_d$, and the other beginning at $t = \Delta t_d$. As shown in Figure 7-3, after Δt_d the response due to the first disturbance begins to damp while that due to the second disturbance grows. The total transient response is simply the sum of the two, i.e.

$$[\frac{m'}{\bar{m}}]_{total} = [\frac{m'}{\bar{m}}]_1 + [\frac{m'}{\bar{m}}]_2 \qquad (7\text{-}40)$$

3. When t becomes greater than $2\Delta t_d$ the response to the first disturbance should have diminished to the point where it is negligible. Therefore, the calculation of it is ceased; the second disturbance becomes the first, and a new disturbance, now considered the second, is initiated at $t = 2\Delta t_d$. The situation it then exactly as it was at $t = \Delta t_d$. This process is repeated after each Δt_d time interval until the desired time is reached.

When velocity and pressure coupling are treated simultaneously the aforementioned procedure leads to a total response given by the sum of four contributions (at $t > \Delta t_d$), i.e.

$$[\frac{m'}{\bar{m}}]_{total} = [\frac{m'}{\bar{m}}]_{p_1} + [\frac{m'}{\bar{m}}]_{p_2} + [\frac{m'}{\bar{m}}]_{v_1} + [\frac{m'}{\bar{m}}]_{v_2} \qquad (7\text{-}41)$$

where the p and v denote pressure coupled and velocity coupled response, respectively; while the subscripts 1 and 2 pertain to the first or second disturbance of each type.

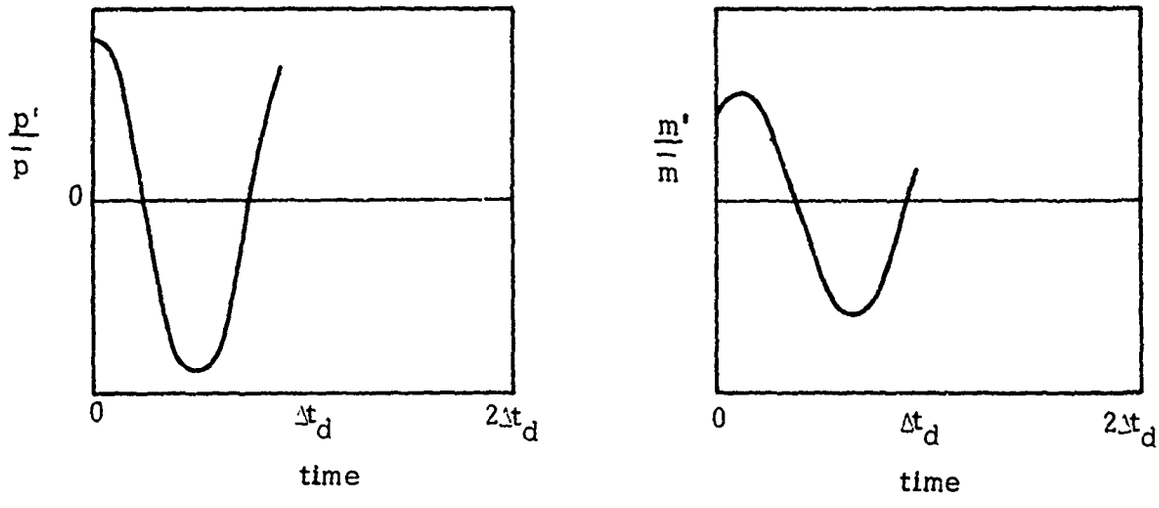

Figure 7-9 Pressure Coupled Response For $t < \Delta t_d$

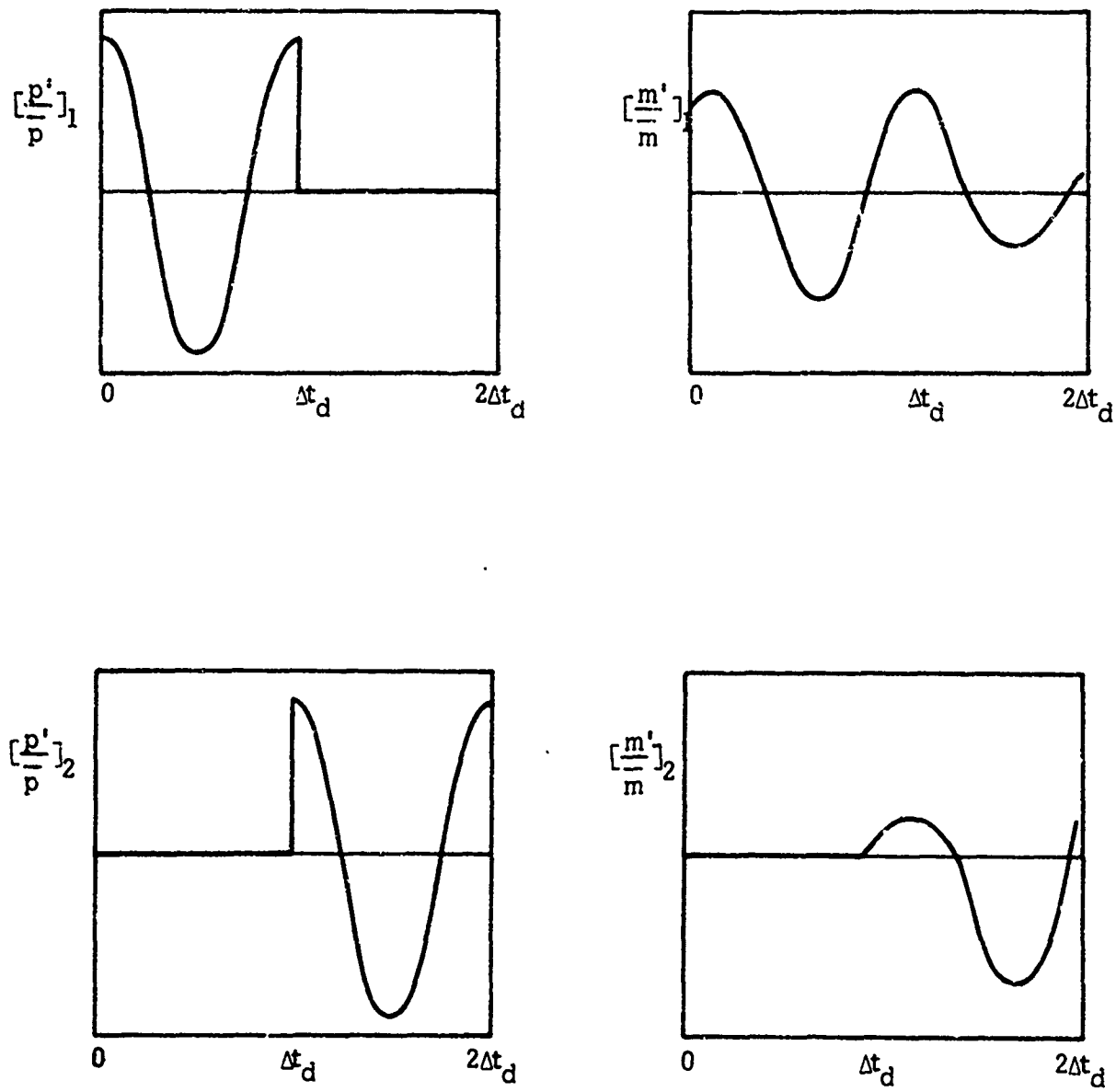

Figure 7-10 Pressure Coupled Response For $\Delta t_d < t < 2\Delta t_d$

7.4 Steady State Solution

The method of solving the steady state equations of motion has already been discussed in Section 6. Basically, the procedure is as follows. The equations of motion, in conservative form, are written as a set of six simultaneous first order differential equations (equation 6-15); which are then integrated using either an Adams-Moulton or Runge-Kutta integration routine.

As discussed in Section 6, the solution is actually an iterative one; wherein a value of chamber pressure, which yields the proper Mach number at the end of the grain, must be found. Newton's method is used to provide further "guesses" of the chamber pressure, after the initial solution has been carried out. This technique has worked quite well. Typically, about two iterations are all that is required. Even when very poor initial pressure guesses were specified, solutions rarely took more than six iterations to converge.

There was, however, one problem with the steady state solution. The boundary condition specified at $x = 0$, $u = u_p = 0$, corresponds to an initial state of dynamic equilibrium between the particles and gas. Like the chemical reaction rate equations these equations are of the "stiff" type and are very difficult to handle, at near equilibrium conditions. Standard, explicit, integration routines like Runge-Kutta and Adam-Moulton are unstable under such conditions, unless extremely fine integration steps are used. This problem can be overcome by the use of an implicit integration technique, as proven by the results of Reference 67, for the chemical kinetics system of equations. In the present case, however, the numerical difficulties at near-equilibrium conditions have been overcome by using an approximation, which serves quite well. The time, and expense, of changing to an implicit formulation and solution was thereby avoided.

The approximate method for overcoming the numerical problem is based on the observation that the gas velocity increases in a very nearly linear manner in constant cross-sectional area chambers. This is due to the fact that the burning rate does not vary to any great extent from the beginning to the end of the grain, for most motors.

It will be recalled (see Section 5) that the fractional lag nozzle solution is based on the assumption that velocity is proportional to axial distance in the region of the throat. The fact that u is also approximately proportional to x in the chamber means that a fractional lag analysis, similar to that of the nozzle region, should yield a very good approximation. The fractional lag analysis in the chamber differs somewhat from that in the nozzle due to the pressure of mass addition, however, very similar results are obtained. Starting from the fractional lag assumptions

$$u_p = K' u$$
$$T_p = 1 - L'(1-T) \tag{7-42}$$

it follows from the continuity equations that

$$\rho_p = \frac{\beta_2 \rho_o}{K'} \tag{7-43}$$

where β_2 is the ratio of particle to gas burning rate (equal to β_1, the particle to gas weight flow ratio). Without going into details, it can be shown that when the burning rate ω is then assumed to be invariant with respect to axial distance the constants K' and L' become,

$$K' = \frac{D}{2}\left[-1 + (1+4/D)^{\frac{1}{2}}\right]$$
$$L' = 1/\left[1 + 3\,Pr\,C(1-K)/K\right] \tag{7-44}$$

where the constant, D, is based on a Stokes flow analysis and is

$$D = \frac{9}{4}\,\frac{\mu}{\sigma^2 \rho_m u_E/L} \tag{7-45}$$

This approximate <u>chamber</u> fractional lag solution is used in one of two ways. If the particle size is so small, or other conditions are such, that near equilibrium (almost no lag) conditions exist throughout the chamber, then the approximation is used to obtain the complete solution, from x = 0 to

$x = 1$. On the other hand, if conditions are such that near equilibrium exists only near the head end, the approximation is used only until the normalized particle velocity is greater than .01 ($u_p > .01$).

The accuracy of this approximate technique has been tested in a few cases by comparing the results to ones obtained by using the exact equations and very small step sizes. The so-called "exact" solutions required that the initial conditions, at $x = 0$, be slightly perturbed out of equilibrium. Even without accounting for the slight differences in initial conditions, the "approximate" and "exact" results agreed to within a fraction of a percent, for the conditions considered. The steady state particle and gas velocities calculated for one of the test cases are shown in Figure 7-11.

For these conditions the gas velocity satisfies, almost exactly, the assumption of linear variation with distance; the primary assumption in the fractional lag analysis. The steady state solution for the case illustrated was actually found two ways; by using the fractional lag approximation for the first 8% of length, and using it over the entire length. The calculated velocities were identical; illustrating the accuracy that can be achieved with the approximate technique when the assumptions upon which it is based are fairly well realized.

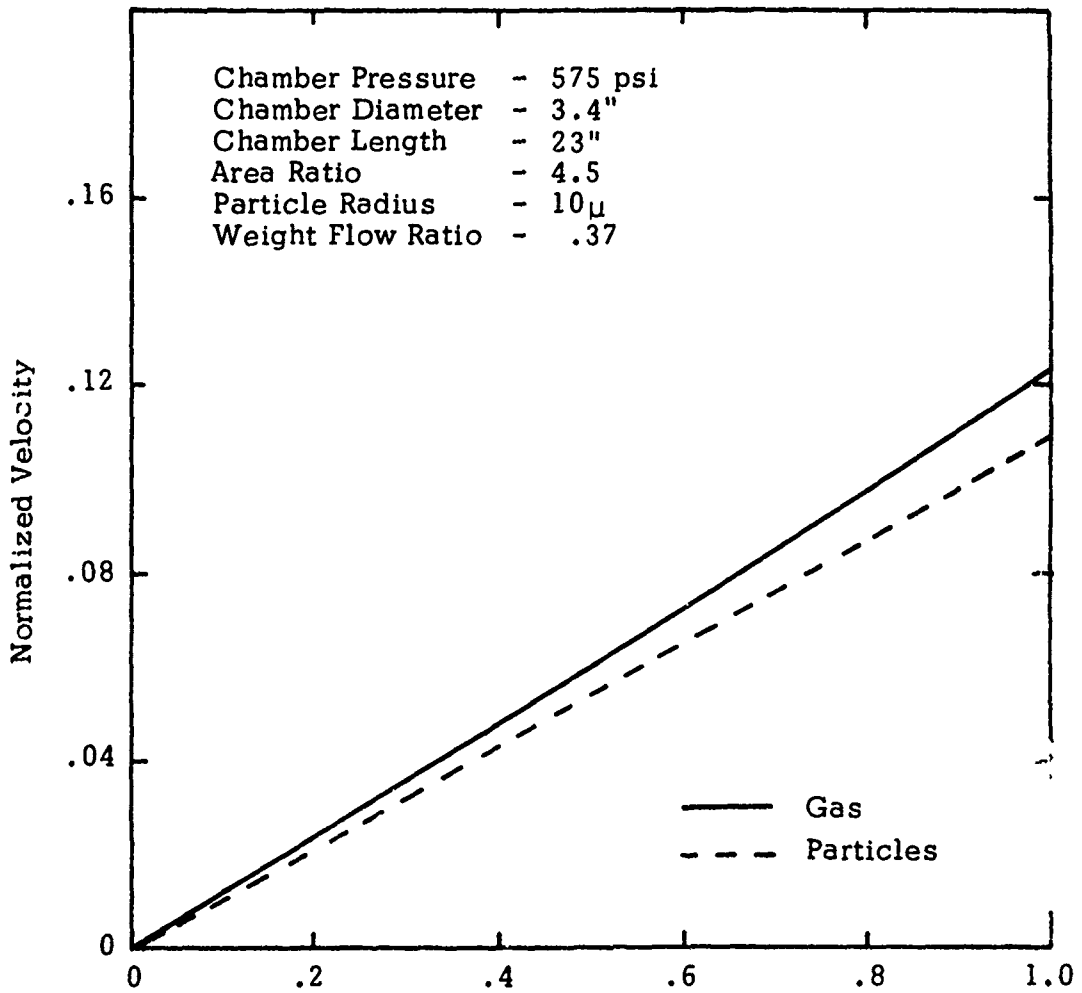

Figure 7-11. Two-Phase Steady State Solution Gas and Particle Velocities Versus Distance

8. ANALYSIS OF LINEAR STABILITY

Since the numerical calculation is valid for all amplitudes, it is useful as a check to compute independently the result for linear stability of a normal mode in the chamber. Eventually one finds a formula for the growth rate of an initial disturbance having the spacial distribution for a classical natural mode. The procedure followed here is that presented in References 31 and 52.

The calculation breaks down broadly into two parts: (1) linearization of the governing differential equations and construction of an inhomogeneous wave equation; (2) solution for the complex wave number for each of the stationary (harmonic) natural modes. All flow variables are assumed to be sums of steady, $(\bar{\ })$, and fluctuating, $(\ )'$, parts. The fluctuations are taken to vary harmonically in time; thus, for example, the perturbation of pressure is

$$\frac{p'}{\bar{p}} = \left(\frac{p'}{\bar{p}}\right)_o e^{i\bar{a}kt} \tag{8-1}$$

where $(p'/\bar{p})_o$ is the initial value and k is the complex wave number,

$$k = \frac{1}{\bar{a}}(\omega - i\alpha) \tag{8-2}$$

Therefore, if the growth constant, α, is positive the waves will grow. For use in checking the numerical results, consider the value of p' after one period of the oscillation, so $t = 1/f = 2\pi/\omega$. Then since α/ω is normally much less than unity,

$$\left(\frac{p'}{\bar{p}}\right)_{t=\frac{2\pi}{\omega}} = \left(\frac{p'}{\bar{p}}\right)_o e^{i(\omega - i\alpha)\frac{2\pi}{\omega}} = \left(\frac{p'}{\bar{p}}\right)_o e^{i2\pi} e^{2\pi\frac{\alpha}{\omega}}$$

$$\approx \left(\frac{p'}{\bar{p}}\right)_o (1)(1 + 2\pi\frac{\alpha}{\omega})$$

Hence, the calculated value of the growth constant is

$$\alpha \approx f\left[\left(\frac{p'}{\bar{p}}\right)_{t=\frac{1}{f}} - \left(\frac{p'}{\bar{p}}\right)_o\right] \tag{8-3}$$

A value for α is, therefore, easily found from the numerical calculation; the purpose here is to obtain a formula for the linear approximation to the problem.

The analysis begins with the complete inviscid conservation equations, given in Section 3.2 but repeated here in slightly altered from.

<u>Conservation of Mass</u>

(Gas Phase) $$\frac{\partial}{\partial t}(\rho A) + \frac{\partial}{\partial x}(\rho u A) = \omega A \tag{8-4}$$

<u>Conservation of Momentum</u> $$\rho\frac{\partial u}{\partial t} + \rho u\frac{\partial u}{\partial x} + \frac{\partial p}{\partial x} = F - u\omega \tag{8-5}$$

<u>Conservation of Energy</u> $$\rho C_v A\frac{\partial T}{\partial t} + \rho C_v A u\frac{\partial T}{\partial x} + p\frac{\partial}{\partial x}(uA) \tag{8-6}$$

$$= \left(\frac{a^2}{\gamma} + \Delta e_o + u^2\right)\omega A + Q_p A + u_p^2\,\omega_p A$$

$$+ (e_{pos} - e_p)\,\omega_p A$$

where F and Q_p are given by equations (3-8) and (3-14) respectively.

and $\Delta e_o = e_{os} - e_o = C_v(T_{os} - T_o)$ is the difference between the energy of the gas entering at the surface and that at the same position in the chamber, and e_{pos} is total energy of the particles at the surface.

*In the numerical analysis, it has been assumed that the flow coming in at the surface enters always with the <u>steady</u> flame temperature. Hence $\Delta T' = -T'$. It is also assumed that $e_{pos} = e_p$.

An equation for the pressure can be formed by adding RT times (8-4) to R/C_v times (8-6):

$$\frac{\partial}{\partial t}(pA) + \gamma p \frac{\partial}{\partial x}(uA) + uA\frac{\partial p}{\partial x} = (a^2 + R\Delta T_o + u^2)\,\omega A$$

$$+ \frac{R}{C_v} A\left[(u_p - u)F + Q_p\right] + u_p^2\,\omega_p A \tag{8-7}$$

where, as in the numerical analysis, $e_{pos} \approx e_p$ is assumed.

The linearized forms of (8-5) and (8-7) are

$$\bar{\rho}\frac{\partial}{\partial t}(Au') + A\frac{\partial p'}{\partial x} = -\bar{\rho}A\frac{\partial}{\partial x}(\bar{u}u') + A(F' - u'\bar{\omega}) \tag{8-8}$$

$$\frac{\partial}{\partial t}(Ap') + \bar{\gamma}\bar{p}\frac{\partial}{\partial x}(Au') = -\bar{u}A\frac{\partial p'}{\partial x} - \gamma p'\frac{\partial}{\partial x}(\bar{u}A) + AP'_{11} \tag{8-9}$$

where

$$P'_{11} = \bar{a}^2\,\omega' + (\gamma RT' + R\Delta T')\,\bar{\omega} + \frac{R}{C_v} A\,Q'_p \tag{8-10}$$ *

Here the speed of sound is for the gas only, $\bar{a}^2 = \gamma\bar{p}/\bar{\rho}$.

The wave equation for the pressure fluctuation p' is constructed by differentiating (8-9) with respect to time and substituting (8-8) for $\partial(Au')/\partial t$:

$$\frac{1}{A}\frac{\partial}{\partial x}\left(A\frac{\partial p'}{\partial x}\right) - \frac{1}{\bar{a}^2}\frac{\partial^2 p'}{\partial t^2} = h_{11} \tag{8-11}$$

*See footnote to previous page.

with

$$h_{11} = -\bar{\rho}\,\frac{\partial^2}{\partial x^2}(\bar{u}\,u') + \frac{\bar{u}}{\bar{a}^2}\,\frac{\partial^2 p'}{\partial t\,\partial x} + \frac{\gamma}{\bar{a}^2}\,\frac{\partial p'}{\partial t}\,\frac{1}{A}\,\frac{d}{dx}(\bar{u}\,A) \tag{8-12}$$

$$-\bar{\rho}\,\frac{\partial}{\partial x}(\bar{u}u')\,\frac{d\ln A}{dx} - \frac{1}{\bar{a}^2}\,\frac{\partial P'}{\partial t} + \frac{1}{A}\,\frac{\partial}{\partial x}[A(F' - u'\,\bar{w})]$$

The boundary conditions on p' (usually at x = 0,L) are set by solving the momentum equation (8-8) for $\partial p'/\partial x$).

$$\frac{\partial p'}{\partial x} = -f \tag{8-13}$$

$$f = \bar{\rho}\,\frac{\partial u'}{\partial t} + \bar{\rho}\,\frac{\partial}{\partial x}(\bar{u}\,u') - (F' - u'\,\bar{w}) \tag{8-14}$$

A formula for the wavenumber is found by comparing the problem governed by Equations (8-11) and (8-12), with the unperturbed problem (i.e., $h_{11} = f = 0$). As shown in Ref. (52), the result is

$$k^2 = k_\ell^2 + \frac{1}{E_\ell^2}\left\{\int_0^L h_{11}\,p_\ell\,A\,dx + \left[p_\ell\,fA\,dx\right]_0^L\right\} \tag{8-15}$$

where

$$E_\ell^2 = \int_0^L p_\ell^2\,A\,dx \tag{8-16}$$

and p_ℓ, k_ℓ are the mode shape and wavenumber for the unperturbed problem. With h_{11} and f given by (8-12) and (8-16), the formula for k^2 can eventually be put in the form

$$(k^2 - k_\ell^2)\, E_\ell^2 = \left(i\, \bar{\rho}\bar{a}\, k_\ell \left[\left(u'\, p_\ell + \frac{\bar{u}\, p_\ell^{\,2}}{\bar{\rho}\bar{a}^2} \right) A \right]_0^L - i\, \bar{a}\, k_\ell \int_0^L p_\ell\, \omega'\, A\, dx \right.$$

$$+ i \frac{k_\ell}{\bar{a}} \left(\frac{1}{\bar{\rho}} \int_0^L \left[p_\ell^2 + \frac{1}{k_\ell^2} \left(\frac{dp_\ell}{dx} \right)^2 \right] \omega\, A\, dx \right.$$

$$- \int_0^L \bar{u}\, \frac{dA}{dx} \left[p_\ell^2 + \frac{1}{k_\ell^2} \left(\frac{dp_\ell}{dx} \right)^2 \right] dx - \int_0^L p_\ell^2\, \frac{d\bar{u}}{dx}\, A\, dx \Bigg)$$

$$- \left(\int_0^L F'\, \frac{dp_\ell}{dx}\, A\, dx + i \frac{k_\ell}{\bar{a}} \int_0^L Q_p'\, p_\ell\, A\, dx \right. \tag{8-17}$$

$$- i \frac{k_\ell}{\bar{a}}\, R \int_0^L \Delta T'\, p_\ell\, \bar{\omega}\, A\, dx + \int_0^L u_p'\, \frac{dP_\ell}{dx}\, \bar{w}_p\, A dx$$

For the purposes here, it is sufficient to consider the case of constant cross-sectional area. Then the continuity equation for the average flow gives the relation between $\bar{\omega}$ and $d\bar{u}/dx$:

$$\frac{d\bar{u}}{dx} = \bar{\omega}/\bar{\rho} \tag{8-18}$$

since it is assumed throughout that the mean values of pressure and density are constant. Hence (8-17) simplifies to

$$(k^2 - k_\ell^2) \int_0^L p_\ell^2 \, dx = i \bar{\rho} \bar{a} k_\ell \left[u' p_\ell + \frac{u p_\ell^2}{\bar{\rho} \bar{a}^2} \right]_0^L - i \bar{a} k_\ell \int_0^L p_\ell \, w' \, dx$$

$$+ \frac{i}{\bar{\rho} \bar{a} k_\ell} \int_0^L \left(\frac{dp_\ell}{dx} \right)^2 \bar{w} \, dx \tag{8-19}$$

$$- \int_0^L F' \frac{dp_\ell}{dx} \, dx + i \frac{k_\ell}{\bar{a}} \int_0^L Q_p' \, p_\ell \, dx$$

$$- i \frac{k_\ell}{\bar{a}} R \int_0^L \Delta T' \, p_\ell \, \bar{w} \, dx + \int_0^L u_p' \frac{dp_\ell}{dx} \bar{T}_p \, dx$$

The first group of terms represents the interactions between combustion and the wave motions at the head end ($x=0$) and the lateral boundary (the integral over w'). The influence of the nozzle is represented by the term evaluated at $x = L$. An important stabilizing effect is represented by the integral over $(dp_\ell/dx)^2$. This is due to the inelastic process of accelerating the incoming gases to the acoustic speed ($u' \sim dp_\ell/dx$). The next group of terms represents the effects of particles in the gas phase - a stabilizing influence. For precise correspondence with the numerical analysis, Q_p' is the fluctuation of heat transfer from the particles to the gas. The last term ($\Delta T'$) is due to non-isentropic interactions between the wave motions and the combustion processes at the boundary.

Now for a uniform port, the unperturbed mode shape and frequency are

$$p_\ell = \cos (k_\ell x) \tag{8-20}$$

$$k_\ell = \frac{\ell \pi}{L} \tag{8-21}$$

and the acoustic velocity is

$$u = \frac{i}{\bar{\rho}\bar{a}\, k_\ell} \frac{dp_\ell}{dx} = -\frac{i}{\bar{\rho}\bar{a}} \sin(k_\ell x) \tag{8-22}$$

It is conventional to introduce an admittance function for the exhaust nozzle, defined as

$$\frac{u'}{\bar{a}} = A_n \frac{p'}{\gamma \bar{p}} \tag{8-23}$$

Then with $u' = \bar{u} = 0$ at $x = 0$,

$$i \rho a k_\ell \left[u' p_\ell + \frac{\bar{u} p_\ell^2}{\bar{\rho}\bar{a}^2} \right]_0^L = i k_\ell (A_n + \bar{M}_e) \tag{8-24}$$

where $\bar{M}_e$ is the Mach number at the entrance to the exhaust nozzle.

The source of mass, ω, is defined so that ωA is the local rate at which mass is added per unit length of chamber. If q is the perimeter and m_b is the mass flux of gases inward from the burning surface, then $\omega A = m_b q$. Now the fluctuations of mass flux, m_b', is related, for pressure coupling only, to the pressure fluctuation according to (see Section 4.1.4):

$$\frac{m_b'}{\bar{m}_b} = R_b \frac{p'}{\gamma \bar{p}} \tag{8-25}$$

Hence, the contribution from the lateral boundary in (8-19) can be written

$$i\,\bar{a}\,k_\ell \int_0^L p_\ell\, w'\, dx = i\,\bar{a}\,k_\ell \left(\frac{S_b}{A}\right) \frac{m_b}{\gamma \bar{p}} \int_0^L R_b\, p'\, p_\ell\, d\left(\frac{x}{L}\right) \tag{8-26}$$

where $S_b = q\,L$ is the area of burning surface. With $p' \approx p_\ell = \cos(k_\ell x)$ and R_b independent of position, this gives

$$i\,a\,k_\ell \int_0^L p_\ell\, w'\, dx = i\,\frac{k_\ell}{2} \left(\frac{S_b}{A}\right) \bar{M}_b\, R_b \tag{8-27}$$

Here $\bar{m}_b = \bar{\rho}\,\bar{u}_b$ and $\bar{M}_b = \bar{u}_b/\bar{a} = \bar{m}_b/\bar{\rho}\,\bar{a}$.

The contribution from the inelastic acceleration of the incoming gases is

$$\frac{i}{\bar{\rho}\,\bar{a}\,k_\ell} \int_0^L \left(\frac{dp_\ell}{dx}\right)^2 \bar{w}\, dx = i\,\frac{k_\ell}{2} \left(\frac{S_b}{A}\right) \bar{M}_b \tag{8-28}$$

The last integral in Equation (8-19) will in general involve both the admittance and response functions since, as shown in the discussion of the response to transient burning,

$$\frac{\Delta T'}{\bar{T}} = \frac{p'}{\gamma \bar{p}} \left[M_b\, A_b - (R_b - 1) \right] \qquad \text{(GENERAL)} \tag{8-29}$$

If the processes are isentropic, the fluctuation of flame temperature, T_f', equals the local fluctuation of chamber temperature, so $\Delta T' = T_f' - T' = 0$. But as noted earlier the fluctuations of flame temperature have not been taken into account in the numerical analysis: $T_f' = 0$. Hence $\Delta T' = -T'$, the isentropic value associated with the waves in the chamber:

$$\frac{\Delta T'}{\bar{T}} = -(\gamma - 1)\,\frac{p'}{\gamma \bar{p}} \qquad \text{(ISOTHERMAL)} \tag{8-30}$$

For these two cases, the integral becomes

$$-i\frac{k_\ell}{\bar{a}} R \int_0^L \Delta T' p_\ell \omega \, dx = i\frac{k_\ell}{2\gamma}\left(\frac{S_b}{A}\right) \bar{M}_b \begin{cases} (\gamma - 1) & \text{(ISOTHERMAL)} \\ \left(\dfrac{R_b - 1}{\bar{M}_b}\right) - A_b & \text{(GENERAL)} \end{cases} \tag{8-31}$$

Hereafter, for comparison with the numerical results, only the isothermal case will be discussed.

For simplicity, consider only the particle/gas force term in (8-9) and ignore the heat transfer for the present. A straightforward calculation of the linearized motions for small particles in oscillating Stokes flow gives

$$F' = \frac{C_m}{1 + i\,\omega\tau_v} \frac{dp_\ell}{dx} \tag{8-32}$$

where C_m is the mass fraction of particulate matter in the chamber, and τ is the characteristic relaxation time for a particle. Since C_m and τ are constant throughout the chamber, one finds

$$\int_0^L F' \frac{dp_\ell}{dx} dx = \frac{C_m}{1 + i\,\omega_\ell \tau_v} \frac{k_\ell^2 L}{2} \tag{8-33}$$

With all the above results, (8-19) is explicitly

$$\frac{L}{2}(k^2 - k_\ell^2) = \left\{ i\,k_\ell (A_n + \bar{M}_e) - i\frac{k_\ell}{2}\frac{S_b}{A}\bar{M}_b R_b \right\}$$

$$+ i\frac{k_\ell}{2}\frac{S_b}{A}\bar{M}_b$$

$$- \frac{C_m}{1 + i\,\omega_\ell \tau} \frac{k_\ell^2 L}{2}$$

$$+ i \left(\frac{\gamma - 1}{\gamma}\right) \frac{k_\ell}{2} \left(\frac{S_b}{A}\right) \overline{M}_b$$

Now $k^2 - k_\ell^2 \approx (\omega/\bar{a})^2 - k_\ell^2 - 2\,i\,\alpha k_\ell/\bar{a}$ and the imaginary part of the last equation gives

$$\frac{\alpha L}{\bar{a}} = \frac{\overline{M}_b}{2} \left(\frac{S_b}{A}\right) (R_b^{(r)} - 1) - (A_n^{(r)} + \overline{M}_e) - \frac{C_m(\omega_\ell \tau_v)}{1 + (\omega_\ell \tau_v)^2} \left(\frac{k_\ell L}{2}\right)$$

$$- \left(\frac{\gamma - 1}{2}\right) \left(\frac{S_b}{A}\right) \overline{M}_b \qquad (8\text{-}34)$$

The factor $C_m(\omega_\ell \tau)/(1 + \omega_\ell^2 \tau_v^2)$ is exactly the result shown in Equation (8-39) of Reference (53); that is, the attenuation constant due to particles is

$$\alpha_p = \frac{1}{2} (C_m\, \omega_\ell) \frac{\omega_\ell \tau_v}{1 + (\omega_\ell \tau_v)^2} = \frac{1}{2} \hat{\alpha}_p \qquad (8\text{-}35)$$

The factor 1/2 arises from the integration over the mode shape, while the remaining factors constitute an approximation to the particle damping. Hence, it is clear that more accurate estimates of the particle damping are accomodated in (8-34) simply by defining $\hat{\alpha}_p$ as shown, and using whatever numbers are available for $\hat{\alpha}_p$:

$$\frac{\alpha L}{\bar{a}} = \frac{M_b}{2} \left(\frac{S_b}{A}\right) \left(R_b^{(r)} - 1 - \frac{\gamma - 1}{\gamma}\right) - (A_n^{(r)} + \overline{M}_e) - \frac{\frac{1}{2} \hat{\alpha}_p L}{\bar{a}} \qquad (8\text{-}36)$$

This is the final result for a uniform port. Recall that it involves explicitly the assumption of isothermal pressure coupling.

8.1 Numerical Example

Consider the pulsed motors tested by Aerojet; the following values are used:

D_p = 1.99 in.

L = 23.5 in.

$\bar{p}$ = 1400 psia

$\bar{r}$ = .436 in./sec.

$\bar{a}$ = 3830 ft./sec.

$\bar{T}$ = 6110 °R

$\bar{\rho}$ = $\gamma\bar{p}/\bar{a}^2$ = .01655 slugs/ft.^{3} = .00852 gm/cm.^{3}

A = 3.11 in.^{2}

S_b = $\pi D_p L$ = 147 in.^{2}

ρ_s = 1.5 gm/cm.^{3} (density of propellant)

The Mach number of the gases leaving the burning surfaces is computed from the continuity relation applied to the interfacial conversion of solid to gas:

$$\bar{\rho}_p \bar{u}_p + \bar{\rho}\bar{u} = \rho_s \bar{r}$$

Then assuming that the particle and gas velocities are the same,

$$\bar{u} \cong \frac{\rho_s \bar{r}}{\bar{\rho}\left(1 + \frac{\bar{\rho}_p}{\bar{\rho}}\right)} \tag{8-37}$$

For the Aerojet propellant $\bar{\rho}_p / \bar{\rho} \approx .37$ and

$$\bar{u} = \frac{(1.5)\ (.436)}{(.00852)\ (1.37)\ (12)} = 4.66 \qquad \text{ft./sec.} \tag{8-38}$$

The Mach number of the gas flow is therefore

$$M_b = \frac{4.66}{3830} = .00122 \tag{8-39}$$

By applying conservation of mass to the average flow in the chamber, one finds for Mach number of the flow entering the nozzle,

$$\bar{M}_e = \frac{S_b}{A}\ \bar{M}_b = .0577 \tag{8-40}$$

For quasi-steady behavior of the nozzle, the admittance function is real, and equal to

$$A_n = \frac{\gamma - 1}{2}\ \bar{M}_e = .00577 \tag{8-41}$$

With these numbers, (8-36) gives

$$\frac{\alpha}{1920} = \underbrace{.0289(R_b^{(r)} - 1.17)}_{\text{(Lateral Burning)}} - \underbrace{.0635}_{\text{(Nozzle)}} - \underbrace{\frac{\hat{\delta}_p}{3840}}_{\text{(Particles)}} \tag{8-42}$$

A wave will grow if $\alpha > 0$, or, if the real part of the response function is sufficiently large,

$$R_b^{(r)} > 3.37 + \frac{\hat{\alpha}_p}{111} \tag{8-43}$$

Equation (8-36) gives the symbolic result,

$$R_b^{(r)} > 1.17 + 2\left(\frac{A_n^{(r)}}{\overline{M}_e} + 1\right) + \frac{\hat{\alpha}_p L}{\bar{a}\,\overline{M}_e} \tag{8-44}$$

This shows the obvious stabilizing effect of increasing Mach number of the mean flow.

9. NUMERICAL RESULTS

In order to check out both the analysis and the programming, several simple test cases were solved. First, the left hand boundary condition was modified to correspond to that of a piston undergoing constant acceleration. A perfect gas solution was then obtained without propellant burning or particles. The flow field generated by the piston motion is isentropic, and the solution at any point in the flow can be found using the Rieman invariants. The numerical solution accurately reproduced the known flow field, thereby verifying the characteristics analysis by itself.

The programming of the transient burning analysis was checked by comparing the transient burning rates computed by the instability program to those obtained from a simple check program (see Appendix A). When the pressure field calculated by the instability program, at a given x location, was input to the check program, the results of the two programs were identical, and served to corroborate the numerical accuracy of the transient burning rate solution. (In Appendix A the results of the check program were verified by comparison with theoretical solutions for several special cases).

The aforementioned test cases were basically designed to check the accuracy of the computer programming, and do not, themselves, contribute to the assessment of the present instability model. During the current project there was not sufficient time to systematically vary all of the solution parameters, or to try to optimize the inevitable accuracy-solution time trade-off. However, a limited number of instability solutions have been obtained and the effects of varying many of the solution parameters, over, at least, a limited range, have been demonstrated. Many of the solutions were obtained for a solid rocket configuration for which experimental data was available[23]; however, no attempt was made during the present effort to obtain quantitative results. Rather, the solutions were obtained, and compared with data, so that the qualitative validity of the results and the predicted trends could be ascertained. The results obtained

to date are summarized in the rest of this section. Except for Section 9.6, all of the calculations considered pressure coupling only.

9.1 Waves In a Closed End Tube

Another, of what might be termed a consistency check was made by modifying the right hand boundary condition to correspond to a solid wall. This allows the problem of wave propagation in a closed tube to be studied. If an external means of driving the waves were also added problems of the type discussed in Section 2.1 could be analyzed. No attempt to do this was made at this time. For waves with amplitudes low enough for the propagation speed to approach that of an infinitesimal sound wave, there should be no distortion of the wave form as it travels up and down the tube; although, if a loss mechanism is present, the wave will eventually damp out. Without a driving mechanism waves cannot grow, however, if they are of finite amplitude their wave form changes during propagation, and should become steeper.

Figures 9-1 and 9-2 show the pressure and velocity waves over one cycle (the time for a wave to travel from one end to the other and back) for the following conditions: length, 23"; chamber pressure, 360 psi; chamber temperature, 6110°F; particle diameter, 10μ, particle weight fraction, .37; γ = 1.2. The initial pressure perturbation corresponds to a first harmonic standing wave with normalized amplitude (small) of .01.

At the frequency corresponding to the above conditions (about 1400 hz) particle damping is large, and the amplitude of the wave diminishes rapidly. At these low amplitudes the flow remains linear, as can be seen from the invariance of the wave form and the fixed location of the node point (x = .5). The amount of particle damping predicted by the current program was semi-quantitatively compared to the results of Dehority[54]. The agreement between the results was within the degree of uncertainty to which the comparisons were made (approximately 10%). The pressure and velocity waves at approximately one half, one, and two cycles, for a closed tube with no particles and an initial first harmonic pressure disturbance of 0.1 amplitude, are shown in Figures 9-3 and 9-4, respectively. This is not a very high amplitude case that rapidly demonstrates nonlinear behavior, however, at the end of two cycles noticeable steepening of the pressure

wave can be seen, and the presence of a second harmonic is easily seen from the form of the velocity perturbation.

9.2 Effect of Burning Rate Parameters--A and B

The transient burning rate analysis developed in Section 4 contains two parameters, A and B, which govern the burning response of a propellant to an applied pressure disturbance. (The thermal diffusivity, $\varkappa$, can almost be considered as an additional parameter, since its value for a given propellant is still subject to a sizeable degree of uncertainty).

Depending upon the values of A and B, the transient burning rate perturbation can lead or lag the pressure disturbance, with amplified or diminished response (i.e., the amplitude of the burning rate perturbation can be larger or smaller than the amplitude of the pressure wave). In a linear analysis, with the pressure assumed to be harmonic, equation (4-34) yields the relationship between the burning rate and pressure. Implicit in this expression is the assumption that the pressure has been harmonic for all time; or, in more physical terms, that the process has been going long enough for the initial behavior associated with the origin of the pressure pulse to be inconsequential. In the present analysis, the pressure variation need not be harmonic, and the response at times immediately following the generation of a disturbance can also be calculated (Equation 4-68). It is still informative, however, to look a bit more deeply at the linear, long time, response; since many of its characteristics carry over, at least qualitatively, to the more general case.

Figure 9-5 shows the real part of the response (normalized by the value of the steady state pressure exponent, n) for A = 15 and B = .7, .9, 1., ($\eta_w = 0$) as a function of a nondimensional frequency, Ω, defined as

$$\Omega = \frac{2\pi f \varkappa}{\bar{r}^2}$$

f, being the frequency of the pressure wave in hz. Figure 9-6 is similar, but for A = 40, B = .8, .9, 1.0. In Section 4.2 it is pointed out that A and

B must satisfy the inequality

$$A < \frac{B+1}{(B-1)^2}$$

and that the peak response occurs in the neighborhood of $\omega = A\sqrt{B}$. The responses illustrated in Figures 9.5 and 9.6 do peak near the values given by this relation. Furthermore, the magnitude of the peak value is seen to grow larger as the values of A and B come closer to violating the above inequality. At low frequencies, to the left of the peak, the burning response leads the pressure, while at high frequencies it lags. (At long times, when equation (4-34) is appropriate).

The transient burning response to more general nonlinear waveforms, which are not pure harmonics, and have variable frequency, will of course be somewhat different. However, when faced with the task of trying to find values of A and B which yield calculated results that correlate well with engine firing data, knowledge of the burning response to constant pure harmonic pressure disturbances can be quite valuable.

Time has limited the extent to which the effects of varying the burning rate parameters could be studied, using the present nonlinear model. In order to make the calculations that were performed more representative and meaningful the engine geometry and propellant parameters were selected to approximately simulate the conditions of the experimental engine firings reported in Reference 23. In these tests the engine was usually subjected to pulsing, however, the configuration selected was one which was spontaneously unstable, i.e., without being pulsed.

The main engine parameters were as follows:

Throat diameter	0.775 in.
Port diameter	1.99 in.
Grain length	23.5 in.
Chamber pressure	1400 psia
Chamber temperature	6110°R
Burning rate	$.32\ (P/500)^{.3}$
Particle weight flow ratio	.37

In order to bring out the burning rate effects more vividly particle damping effects were kept to a minimum by selecting a particle size of 2μ[+]. Linear analysis (see Section 8.1)was used to provide a guide as to the size of the response factor needed to initiate instability. Curves such as illustrated in Figures 9-5 and 9-6 were then used to select values of A and B thought to correspond to stable and unstable response. The A and B values chosen were:

$$A = 15 \qquad B = .7$$
$$A = 11.5 \qquad B = .64$$

In order to begin the calculations a steady state solution was obtained, which was then, in turn, perturbed by the addition of a first harmonic standing pressure wave with amplitude equal to one-tenth of the mean pressure. Instability solutions were then carried out for approximately three cycles[++]. Figure 9-7 shows the calculated pressure histories at the head end, $x = 0$, and end of the grain, $x = 1$, for $A = 15$ and $B = .7$. Figure 9-8 contains the corresponding results for $A = 11.5$, $B = .64$. These results correspond to the type of measurement one obtains with a pressure transducer, except that the values shown are perturbations, i.e., they have the unperturbed steady state values subtracted out.

As expected, the results indicate that if $A = 15$, $B = .7$ the initial perturbation damps. While, with $A = 11.5$, $B = .64$, the wave ultimately amplifies. In the former case, the wave damps approximately 10% per cycle, while the unstable case shows an interesting nonlinear phenomenon

[+]The measured (as well as calculated) frequency was approximately 375 hz. Reference 54 was then used as a guide in selecting the particle size. Other calculations were also made with 5μ and 9μ particles (see Section 9.4). At the quoted frequency, 9μ particles are approximately the size corresponding to maximum particle damping.

[++]Time has been nondimensionalized by L/a_f; a_f being the gas only sound speed. If the wave speed in the two phase mixture were exactly equal to a_f then a cycle would correspond to a nondimensional time of 2. Since the two phase wave speed was less than a_f a cycle corresponded to $t \approx 2.3$.

After the first cycle the wave is almost unchanged; however, the second cycle sees the wave grow by about 40%, and by the end of the third cycle the perturbation has been amplified an additional 60%. Figure 9-22 contains' results for the same conditions, except for particle size, which show that the perturbation may actually first damp before ultimately amplifying. It appears that this behavior may be related to the "necking" phenomena which can be observed in experimental pressure traces, following [illegible]g. An explanation for the calculated results, and, hopefully, at least a partial explanation for the "necking" phenomena, can be inferred from the nature of the transient burning response.

The normalized values of the transient burning rate perturbation, (as calculated using Equation 4-68), for the same two sets of A and B values, are presented in Figures 9-9 and 9-10. The usual response factor calculations are not applicable at short times after the onset of a finite size disturbance. They assume that a harmonic disturbance has been present for all time. Realistically, however, the propellant cannot be expected to respond instantaneously to a sudden pressure change. The change in pressure alters the heat transfer rate to the propellant and initiates a thermal wave that travels down through the propellant. The initial response of the propellant, therefore, contains start up "transients" which, if the frequency and amplitude of the wave do not change rapidly, eventually die out. Only under these conditions of constant or slowly varying wave form, and damped initial transients, can the historic form of response function yield even approximately valid results.

As shown in Figures 9-9 and 9-10, as well as in Appendix A, the nature and duration of the initial transient burning response is a strong function of the values of A and B, as well as of the nature of the disturbance. With A = 15 and B = .7, the transient burning rate initially varies at a frequency close to that of the pressure wave, but with shifting phase angle. The ratio of the magnitude of the burning rate fluctuations to the magnitude of the pressure perturbation, $|(m'/\bar{m})/(P'/\bar{P})|$, ($(m'/\bar{m})/(P'/\bar{P})$ is simply related to the response function by Equation 4-35, and will at times be referred to as the response function) can be seen (using Figures 9-7 and 9-9) to vary from

a little less than 2, initially, to a value of about 4 at the end of one cycle. It then decreases over the next two cycles to around 2, which is approximately equal to the usual "long time" value of this ratio for the given A and B values and frequency.

Here, the most vivid aspect of the initial transient, is the peak in response at the end of the first cycle, at a value about twice that of the "steady state" response. Even with this initial boost in response the pressure decays over the first cycle, although not as rapidly as during the succeeding cycles. It is worth pointing out here, that the fate of the pressure disturbance depends not only on the magnitude of the burning rate, but also on its phase relationship to the pressure. Since neither the magnitude, nor the phase, of the response remains constant it serves to somewhat complicate the interpretation of nonlinear instability calculations.

The second set of results presented in Figures 9-9 and 9-10 were for A = 11.5, B = .64. Comparison of the pressure and burning rate histories at the head end shows that the response factor is initially about 1.5, and then grows to around 6.25, 7.75 and 8.0, at the ends of the first, second and third cycles respectively. The "long time" value of the response factor for this case is in the neighborhood of 8, so rather than exhibiting an initial peaking behavior, these results show a gradual climb to a "steady state" value over several cycles. It is this relatively slow build up in response that accounts for the fact that the pressure does not increase during the first cycle; only to be amplified at an increasingly faster rate during the succeeding cycles. Although not proven yet, it can be readily hypothesized that the "necking phenomena," referred to earlier, that is observed in pressure traces from pulsed engines, can be attributed to a similar slow build up in burning response. It is hoped, that in the future, an investigation relating to this phenomena can be carried out, and the validity of the hypothesis proven.

The previous discussion was based on observation of the pressure history at a fixed location. It is also illuminating to look at the results as a function of axial distance, for different times. Figure 9-11 shows the pressure distribution in the chamber just after the disturbance was

initiated and at the approximate end of each of the first three cycles. Figure 9-8 demonstrated that the wave amplitude was unchanged after one cycle. The new figure, 9-11, shows that the waveform also remained essentially the same during this interval. At the later times, t = 4.6 and 6.9, the wave is seen to have grown, while the null point moves towards the left and the positive portion of the wave becomes somewhat larger in magnitude than the negative part ($|P_{x=0}| > |P_{x=1}|$). The wave is still predominantly a first harmonic, but it is not pure any longer. Nonlinear gasdynamic effects have caused the wave to steepen a bit; which, in other words, says the wave contains some higher harmonic content.

Since the current analysis is nonlinear, the wave is, and must be, treated in its entirety; however, it is still constructive, at times, to consider the wave as made up of a basic frequency and harmonics. Consider Figure 9-12, which shows the velocity perturbation in the chamber ($u - u_{t=0}$) at the same, end of cycle, times. If the pressure disturbance was a true standing wave the velocity wave would be passing through the null position at the end of a cycle. As the number of cycles increase it can be seen that the velocity wave develops a small remainder at the end of a cycle (note the scale factor on the velocity axis), which by the end of the third cycle is beginning to look reminiscent of a second harmonic velocity wave form.

Remembering the indications of at least a small amount of higher harmonic content in both the pressure and velocity waves, it is instructive to look at the wave form of the mass burning rate perturbation $(\dot{m} - \dot{m}_{t=0})$+ shown in Figure 9-13. The wave forms depicted are definitely purer than those corresponding to the velocity and pressure. Note the central nodal point at x = .5 has hardly been displaced even after three complete cycles. Obviously, the burning rate, for this case, does not rapidly respond to small, higher frequency, disturbances. This is the first evidence that the current transient burning rate model yields a response which, essentially,

+The so-called transient burning rate perturbation shown in Figures 9-5 and 9-10 is actually $(\dot{m} - \dot{m}_{t=0})/\dot{m}_{t=0}$.

is able to discriminate between harmonics. Something which it must do if it is to be a viable model.

The next section will deal in further detail with the response of the propellant to different harmonics.

9.3 Effect of Initial Disturbance Wave Form

Since neither the form of the disturbances which occur randomly in a rocket engine chamber, nor the exact conditions generated by an experimental pulsing apparatus are really known, it would be accommodating if the instability results calculated using the present model were insensitive to the nature of the initial disturbance. As it turns out, however, this is not the case; at least over the first few cycles.

Admittedly, the exact form of a small random disturbance should hardly matter in an engine which is spontaneously unstable, since the tendency of an engine-propellant combination will be to amplify only those modes which are ultimately observed. If an analytical model is to be truly representative, it too must possess this property. In such a case one should use some general wave form, made up of arbitrary percentages of the first harmonic and various overtones, as the initial disturbance and let the model dictate which mode or modes will be amplified and which will disappear. If a single pure harmonic is used (1st, or 2nd, or 3rd, etc.) as the initial disturbance one runs the risk of not being able to simulate the actual response, since all the rest of the harmonics will not be present initially and may not be created, even through nonlinear modification of the original wave form.

Similar considerations also hold with respect to predicting the results of pulse tests. However, there are further complicating factors in this case. (Neglecting, for the present, the fact that pulse guns usually introduce foreign gases). First, the pressure pulse introduced is accompanied by velocity and temperature disturbances. Accurate representations of each of these is, of course, not feasible. Second, the location and magnitude of the pulse can influence the measured results, even after many cycles, and to the extent of even determining whether the pulse will eventually grow

or decay. Hopefully, the present model, with suitable modification[+], if necessary, will be able to serve the dual role of both predicting and helping to understand the basic mechanism underlying each of these effects.

Several instability solutions have been obtained in an initial effort to understand the characteristic behavior of the present model, as it relates to the foregoing discussion. The engine geometry and propellant properties were the same as those listed in the previous section, and the same two pairs of A and B values were used.

The first solution to be discussed was identical to the A = 11.5, B = .64 case presented in the previous section, except the initial disturbance was taken to be a 10% second harmonic, instead of the 10% first harmonic employed earlier. The pressure and transient burning rate perturbation histories at the head end and end of the grain are presented in Figures 9-14 and 9-15. Like the earlier cases, this solution was also carried out for 3 cycles, however, since the frequency is twice as large, the elapsed time is only half that of the first harmonic cases.

In comparing these results for the second harmonic to the earlier results (Figures 9-8 and 9-10 one is immediately struck by the fact that the second harmonic damps, while the first was amplified. This difference can be traced to the behavior of the transient burning response. At the higher frequency the response factor (ratio of normalized burning rate perturbation to normalized pressure perturbation) peaks in the neighborhood of 2, before decreasing to order unity; while, it will be recalled, that the response factor for the first harmonic rose steadily to a value around 8. Additionally, the response at the primary frequency was approximately in phase, while the second harmonic response exhibits a significant phase lag. This behavior was, of course, to be expected, in view of the characteristics of the usual linear response factor; as shown in Figures 9-1 and 9-2. For the engine configuration under consideration, the frequency

[+]For instance, the addition of velocity coupling to the transient burning rate model.

of the first harmonic is very near the peak in the response versus frequency curve. The frequency corresponding to the second harmonic is then significantly displaced to the right of the peak, and, hence, results in a much lower burning response. The peak also corresponds to zero phase shift, while the amount of phase lag monotonically increases as the frequency becomes higher. Under these conditions, each of the higher harmonics should be increasingly damped, as their frequencies move further and further away from the peak on the response curve.

The pressure and velocity waveforms in the chamber, for the second harmonic case, are presented in Figures 9-16 and 9-17, respectively. Figure 9-16 shows the initial pressure disturbance, and the waveform at the end of two cycles (t = 2.39). The velocity peaks one-quarter cycle after the pressure; therefore, in order to show the velocity waveforms at close to their peak values, they are shown in Figure 9-17 at t = .3, and t = 2.7. Earlier, in discussing the type of initial disturbance to select when solving a spontaneous instability problem, it was suggested that a general waveform containing the first and several higher harmonics be employed. In order to see how this idea would work out in practice, an instability solution was obtained starting with an initial pulse consisting of the sum of a 5% first harmonic and a 5% second harmonic. The same A and B values (11.5 and .64) and engine configuration were stipulated. It will be recalled that individually the first harmonic was amplified, while the second was damped. The results presented in Figure 9-18 should, therefore, come as no surprise. This figure shows the initial pressure distribution in the chamber, and its subsequent development. The curves are spaced in time at approximate intervals of $\Delta t = 1.3$, corresponding to the time for a full cycle at the frequency of the second harmonic. Every other curve, then, corresponds to a full cycle of the first harmonic. It can be seen, that as time progresses, the presence of a second harmonic becomes less and less obvious, until, at the last time (t = 6.90), it has all but disappeared. The same effect can be seen in the velocity, as demonstrated by Figure 9-19. Here, as in Figure 9-12, the velocity waves are shown only slightly displaced from their null positions (the times plotted are not exactly full cycles, and there is also some effect of nonlinearities) so

their magnitude is small. In fact, a comparison of the pressure and velocity wave forms at $t \approx 6.9$, with those of the corresponding first harmonic only (initial pulse) case in Figures 9-11 and 9-12, indicates that there is less second harmonic content in the waves which started with 50% second harmonic. This seeming paradox is due to the presence of nonlinear effects, as explained below.

Both the "first harmonic only" and the "mixed" case were initiated with 10% magnitude pulses. In the former case the pressure grows, after the first cycle, and by $t = 6.9$ has been amplified about 220%. In the "mixed" case the first harmonic continues to behave in the same manner, however, the second harmonic content (50% initially) is almost completely damped out by $t = 6.9$. As a result, the wave, after initially being damped, has only amplified by about 17% at $t = 6.9$. The nonlinear effect of wave steepening, is, of course, amplitude dependent. The wave steepening process corresponds to the generation of higher harmonics. At the higher amplitude of the "first harmonic" case second harmonic content is being produced more rapidly than in the lower amplitude "mixed" case. Thus, while the second and higher harmonics damp fairly rapidly, they will always be present to some degree in high amplitude waves, for they are continuously being generated.

The pressure and burning rate histories at $x = 0$, and 1, are presented in Figures 9-20 and 9-21, so they may be compared to the earlier ones for the "pure" first and second harmonic cases (Figures 9-8, 9-10, 9-14 and 9-15). The disappearance of the second harmonic content and lack of burning response to it, is also vividly portrayed in Figures 9-20 and 9-21.

It was gratifying to observe this ability of the model to selectively amplify the first harmonic, since the experimental pressure traces recorded for this engine configuration showed it to be spontaneously unstable; with very little higher harmonic content in evidence, even after many cycles.

The idea of using an initial pulse containing all the modes of interest (at least the primary and lower harmonics, the higher frequency elements

will always be created by nonlinear effects) has proven to be an interesting one, and is probably worth adopting as standard. The effort to perform further quantitative comparisons with data is certainly warranted. This will involve, among other things, continuing the calculations for many more cycles so that calculated and measured growth rates and limiting amplitudes can be compared.

9.4 Effect of Particle Size

For a given particle weight fraction, the amount of damping is a strong function of both frequency and particle diameter. Several linear analyses of acoustic wave particle damping have been performed, e.g., Ref. 53. These show that, at a given frequency, the amount of damping peaks for a certain diameter particle, and falls off, usually fairly rapidly, for larger and smaller particles. Nonlinear damping calculations[69] have shown that nonlinear effects tend to shift the particle diameter corresponding to maximum damping without affecting the maximum amount of damping, itself.

When all of the other gains and losses are fairly well balanced the amount of particle damping can be the factor which determines the stability of the rocket motor. Also, if the amount of particle damping is large, it can improve the stability characteristics of an engine even if the other gains are much greater than the losses.

The present analysis represents a step forward since nonlinear particle damping is included in a total instability model so its effect is completely coupled to the other combustion and flow phenomena. Currently, the model assumes the particles are all of uniform size. This assumption was made to enable the basic model to be assessed in as straightforward and simple a manner as possible. There is no theoretical restriction of the type of particle size distribution which could be incorporated into the instability analysis, e.g., an analytical particle distribution function, or an approximation to a distribution using a discrete set of particle sizes. The use of even two particle sizes would be a significant step towards realistically matching the bimodal type particle size distributions typically found in solid rocket motors.

The instability calculations presented previously were all based on a particle diameter of 2μ. A few instability solutions were also performed, varying only particle diameter, in order to assess the behavior of the solution, with respect to this parameter.

Figure 9-22 shows a comparison of the pressure histories at the head end for cases with particle diameters of 2, 5 and 9 microns. The results of Reference 54 indicate that, at the frequency and weight flow ratio of these test cases, the maximum damping occurs for about 9μ particles. The results shown do indicate that as the particle size goes from 2 to 9 microns damping does increase. The peaked nature of the damping versus particle size curve is not illustrated, since larger than 9μ particles were not considered in this brief initial look at particle damping. With A and B values of 11.5 and .64; linear analysis (see Section 8.1) predicts that the engine would be unstable for all three particle sizes considered. As seen in Figure 9-22, the present calculations corroborate the linear results. Thus, this particular engine, could not be stabilized by efforts to vary aluminum particle size. Increasing the weight fraction of aluminum would, of course, eventually provide enough damping, assuming no other deleterious effects were also induced. The actual particle size distribution in the experimental engine that this case was based on, is not known. The engine firings were, however, spontaneously unstable; thus, there is qualitative agreement between the current findings and experiment, regardless of the particle size.

Particle damping is, of course, due to the inertia of the solid particles, which causes them to exert a drag force on the gas in their efforts to keep up with it. In a constant velocity flow the particles would eventually attain the gas speed. When the gas is accelerating, however, the particles can never quite reach the gas velocity, no matter how small the particles or the rate of acceleration. Figures 9-23 to 9-25 show the particle and gas <u>total velocities</u> (not velocity perturbations) about one-quarter cycle past the end of the first cycle ($t \approx 2.9$), when the gas velocity is passing through its peak; for each of the three particle sizes considered. Figure 9-23 shows that the 2μ particles are small enough to just about keep up with the gas. The difference in particle and gas

velocity being only a fraction of a percent. As the particles become larger their inertia causes them to lag further and further behind the gas. Figures 9-24 and 9-25 show approximately a 6% lag for the 5μ particles and a 15% lag for the 9μ particles. Note that the magnitude of the gas velocity (and pressure, see Figure 9-22) decreases as the increased from 2 to 9 microns, due to the larger amount of energy dissipated through drag.

9.5 Effect of Initial Disturbance Amplitude and Drag Law

The extent to which pulse amplitude serves as a determining factor in the stability of a solid propellant engine is not yet understood. Nor is the role of the initial pulse known with respect to its influence upon the limiting amplitude. The foregoing are, of course, nonlinear phenomena, and, as such, are not amenable to solution by the linear techniques which have been the backbone of solid rocket instability analysis, in the past. The present computer program represents a tool, which, hopefully, will allow these phenomena to be investigated and the extent of their influence to be determined.

All that has been done to the present time, is to look at the differences in response (over the first cycle only) to initial disturbances of varying amplitude. This preliminary effort serves only as a relative indicator of the extent to which nonlinear effects are encountered at various amplitudes. Some of these results are presented below.

Figure 9-26 shows a comparison between the head end pressure histories for two instability solutions which differ only in the magnitude of the initial pulse. The pressure perturbations have been normalized by these initial values, in each case, to allow the differences to be more easily discerned. One solution has been discussed earlier; the 10% magnitude, A = 11.5, B = .64, first harmonic case. The second solution employed an initial 2% pulse. As illustrated in Figure 9-26, there is not too much difference between the two solutions. The normalized amplitudes of the two solutions are essentially the same at the end of the first cycle, however, the history of the larger amplitude wave shows it has

become somewhat steeper than the smaller amplitude wave. The differences between the two solutions would continue to grow as time increased, and the waves amplified (this case was unstable). These results do indicate, however, that waves in the 0 to 10% amplitude range are not rapidly distorted due to the influence on nonlinear effects.

A similar pressure plot, which covers a wider amplitude range, is presented in Figure 9-27, for somewhat different conditions. The chamber pressure was 360 psi, port to throat area ratio was 4.5, and 10_{μ} particles were used. The transient burning rate parameters, A and B, were taken to be 10 and .8, respectively. All other conditions were essentially the same as those for the solutions previously discussed. These new conditions correspond to significantly increased particle and nozzle damping and decreased burning response. (The frequency of the first harmonic for this case was about 1400 hz). It is not surprising, therefore, that the waves damp quite rapidly.

Two of the curves shown in Figure 9-27 correspond to first harmonic disturbances with initial amplitudes of 1% and 50% of the mean pressure. The third curve also corresponds to a 50% initial disturbance, however, in this case, a Stokes law drag coefficient was used to see what the difference would be. (The drag law used in all the other solutions is given by equation (3-9)). It can be seen that the 50% initial amplitude waves are subject to large and rapid steepening, even though they have damped to one-third their starting amplitude during the first cycle. Although not too evident in the Figure, the 50% initial amplitude waves were damped, percentagewise, somewhat more than the 1% wave. To be exact, the 50% waves were both damped about 67%, while the 1% wave was damped by only 63%. Although the conditions for which these solutions were obtained are not the most representative of solid rocket engines, in general, the results are interesting because they show the current model is capable of predicting an amplitude dependence for the damping rate. This is an important feature, one that is necessary, if a model is to be capable of calculating limiting amplitudes.

The results for the two 50% initial amplitude cases are also interesting since they illustrate the effect changing the drag law. At this large amplitude, particle Reynolds numbers (based on relative velocity between particle and gas) on the order of 300 are encountered, far beyond the range where Stokes' law is valid ($Re \lesssim 1$). At such Reynolds numbers, the nonlinear drag law given by equation (3-19) yields a drag coefficient several times larger than Stokes' law. Despite this fact, Figure 9-27 shows that even such a large change in drag coefficient did not measurably affect the amount particle damping even when particle damping was, itself, quite large. (Particle damping accounts for about 2/3 of the total damping for this case). The Stokes law wave is seen to have steepened up considerably more than the other one, however, the amplitudes at the end of one cycle are almost identical.

The relative insensitivity of the computed results to the form of the drag coefficient-Reynolds number relationship can be explained as follows. Other things being equal, a larger drag coefficient will cause the relative velocity between particles and gas to decrease. The drag force exerted on the gas is proportional to $C_D \Delta V^2$, therefore, the combination of higher C_D and lower ΔV creates at least a partial balance, leaving the total force relatively unaffected. That the above actually occurs is graphically portrayed in Figure 9-28. The solid lines denote the gas and particle velocities calculated using Stokes' law, while the dashed lines show the same quantities at the same time as calculated using equation (3-9). As mentioned previously, the nonlinear drag coefficient is several times larger than its Stokes flow equivalent, but, as seen in the Figure, the corresponding relative velocities have an inverse relationship to the magnitude of C_D.

In other cases, where the waves grow or remain large for may cycles, the form of drag law may be more important, however, based on the present result, it does not appear that the exact form of the drag law is critical.

9.6 Velocity Coupling

A method for calculating the nonlinear effects of velocity coupling on the growth of pressure waves in a combustion chamber has been developed (see Section 4.3), and a limited number of solutions have been obtained in order to observe the qualitative characteristics of the model. The scope of the present effort did not allow for a systematic investigation of the effects of velocity coupling.

A series of instability solutions have been obtained for an engine configuration quite similar to that described in Section 9.2. Some of the dimensions and the propellant properties were modified, however, so the results are not directly comparable. All of the following solutions used $A = 11.5$, $B = B_v = .64$, $n = n_v = .3$, and 2μ particles. The four solutions differed as follows:

1. Velocity coupling only, $u_{th} = 0$
2. Pressure coupling only
3. Pressure and velocity coupling, $u_{th} = 0$
4. Pressure and velocity coupling, $u_{th} = .04$

Figures 9-29 and 9-30 show the waveforms of the pressure and burning rate perturbations, respectively, for the fourth case, i.e., pressure and velocity coupling with $u_{th} = .04$. The four curves on each graph depict the results at $t = 0$ and approximately at the end of each of the first three cycles. It can be seen that the pressure initially damps during the first cycle, but begins to be amplified during the following cycles, as the burning rate response builds up. At the end of the third cycle the pressure wave has recovered to just about its initial amplitude. Looking at these pressure waveforms in Figure 9-29, it can be seen that very little harmonic distortion has been introduced into the pressure wave over the first three cycles. This contrasts with the burning rate waveforms in Figure 9-30, which show a marked degree of distortion (compare Figure 9-30 with Figure 9-13).

The distortion in the burning rate waveform is, of course, due to the addition of a velocity coupled response which is inherently nonlinear. The fact that the pressure wave had so little harmonic content is evidence that, in this case, the energy coupling between the velocity coupled response and

the pressure wave was quite inefficient. Further evidence of this will be presented in later figures, as well as an explanation of the reason for this weak coupling. The pressure and pressure coupled burning rate histories for this case are, qualitatively, quite similar to those shown previously in Figures 9-8 and 9-10. Figures 9-31 and 9-32 show the time histories of the velocity perturbation function (Eqs. 4-71 and 4-72) and the transient velocity coupled burning rate at several different axial locations. The nonlinear nature of the velocity driving function is quite evident in Figure 9-31. The burning response tends to smooth out the distortions of the driving function as shown in Figure 9-32. There remains, however, a bias in the burning response that results in the waveform having a positive contribution greater than the negative contribution during the balance of the cycle. This bias generates a net positive contribution to the mass and energy in the chamber and could be responsible for the increase in mean pressure observed in so many instability traces.

Figure 9-33 shows the pressure histories at $x = 0$ for case 1, 2 and 4. The results for case 3 are quite close to those of 2 and 4 and have been left out for the sake of clarity. Here, again, it is apparent that the energy transfer from the velocity coupled response is quite inefficient in this case. Thus, the pressure coupled only and pressure plus velocity coupling pressure histories are almost identical; while with velocity coupling only, the pressure damps rather quickly since there is not enough gain to offset the significant amount of damping in the chamber.

The extremely inefficient transfer of energy from the velocity coupled response is due to the phase relationship between the velocity coupled burn rate and the pressure. The results of the linear analysis (Eq. 8-19) show that the coupling between the combustion and the wave motion is proportional to (in nondimensional form)

$$\int_0^1 p_\ell \, w' \, dx \tag{9-1}$$

If the waves in the chamber were pure harmonic standing waves the pressure, velocity and velocity coupled response would vary as follows, in the

absence of rectification or threshold effects.

$$P_\ell \approx \cos (k_\ell x)$$

$$v_\ell \approx \sin (k_\ell x) \qquad (9\text{-}2)$$

$$\left(\frac{m'}{\bar{m}}\right)_{v_\ell} \approx \sin (k_\ell x)$$

Thus, if the velocity coupled response were linear (i.e., rectification and threshold effects not present), then Equation (9-1) shows that the coupling between the velocity coupled response and the pressure wave would be zero. In the present model the amount of energy transferred to the pressure wave thus depends upon how much rectification and threshold effects modify the waveform of the velocity coupled response. For the conditions of the present solutions the coupling remains quite weak. General conclusions about the effect of velocity coupling must be deferred until solutions at a range of conditions, and for longer durations, have been obtained.

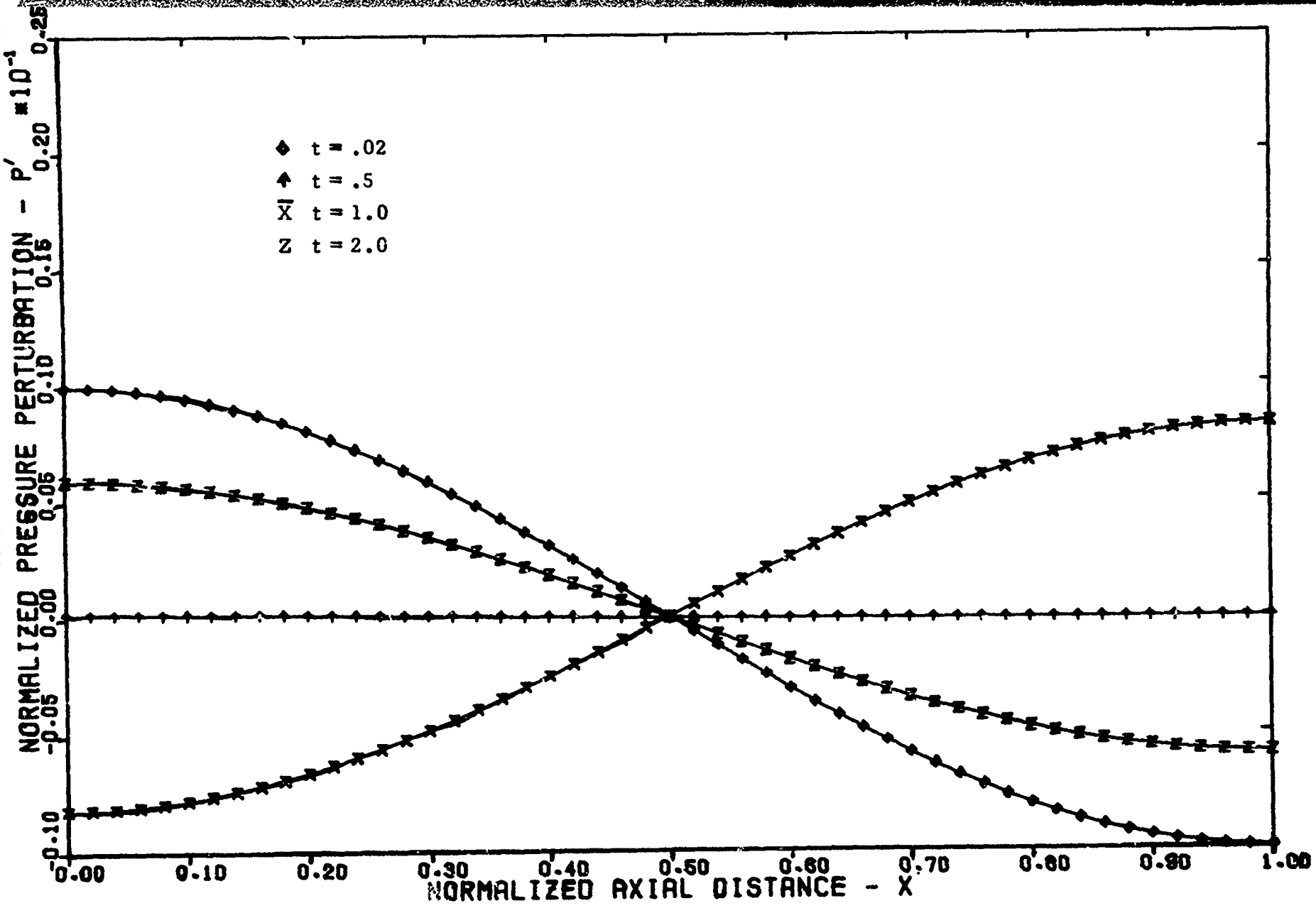

Figure 9-1. Wave Damping in a Closed Tube - 10 Micron Particles, $P_0' = .01 \cos(\pi x)$

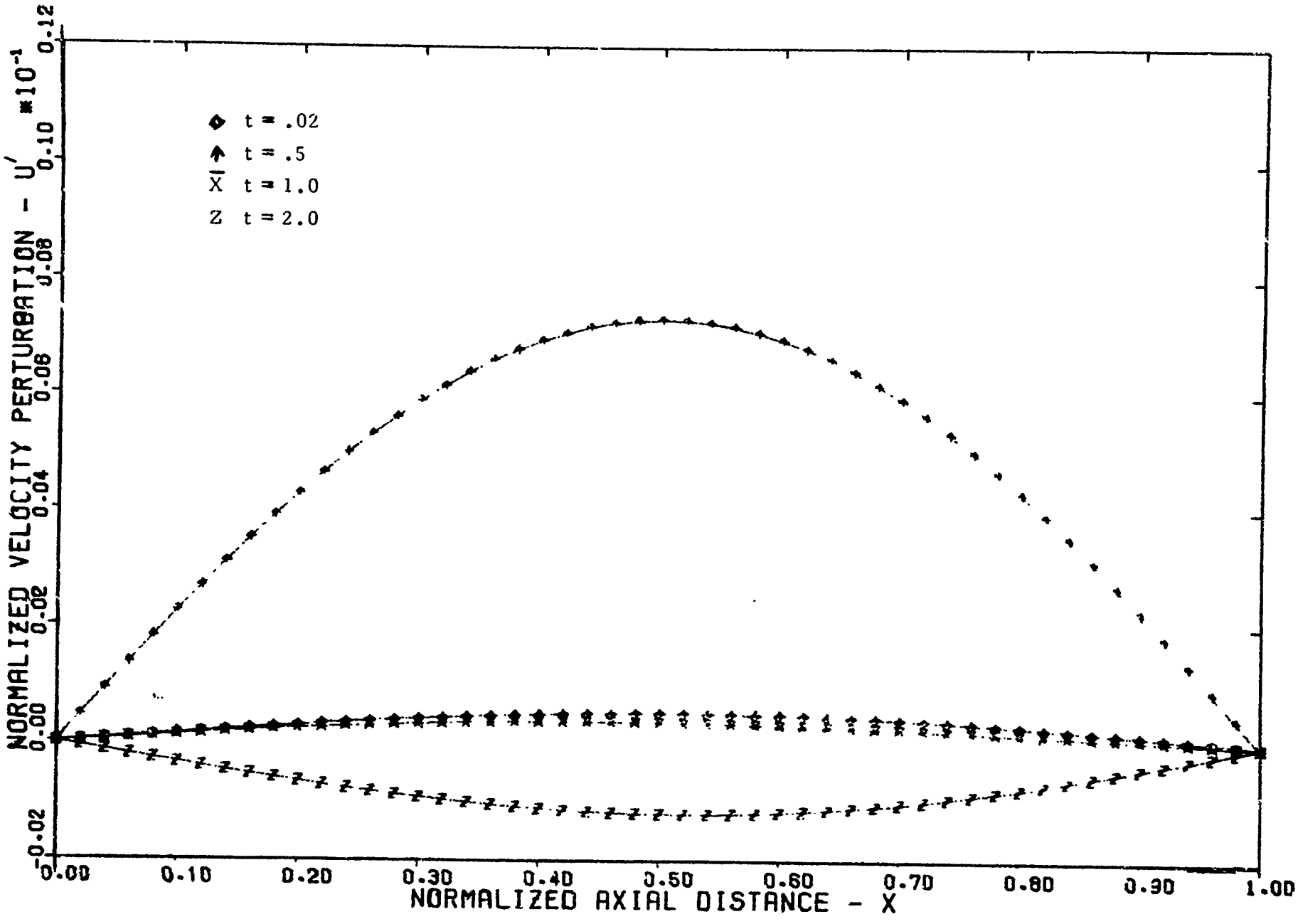

Figure 9-2. Wave In A Closed Tube - 10 Micron Particles, $P_0' = .1 \cos(\pi x)$

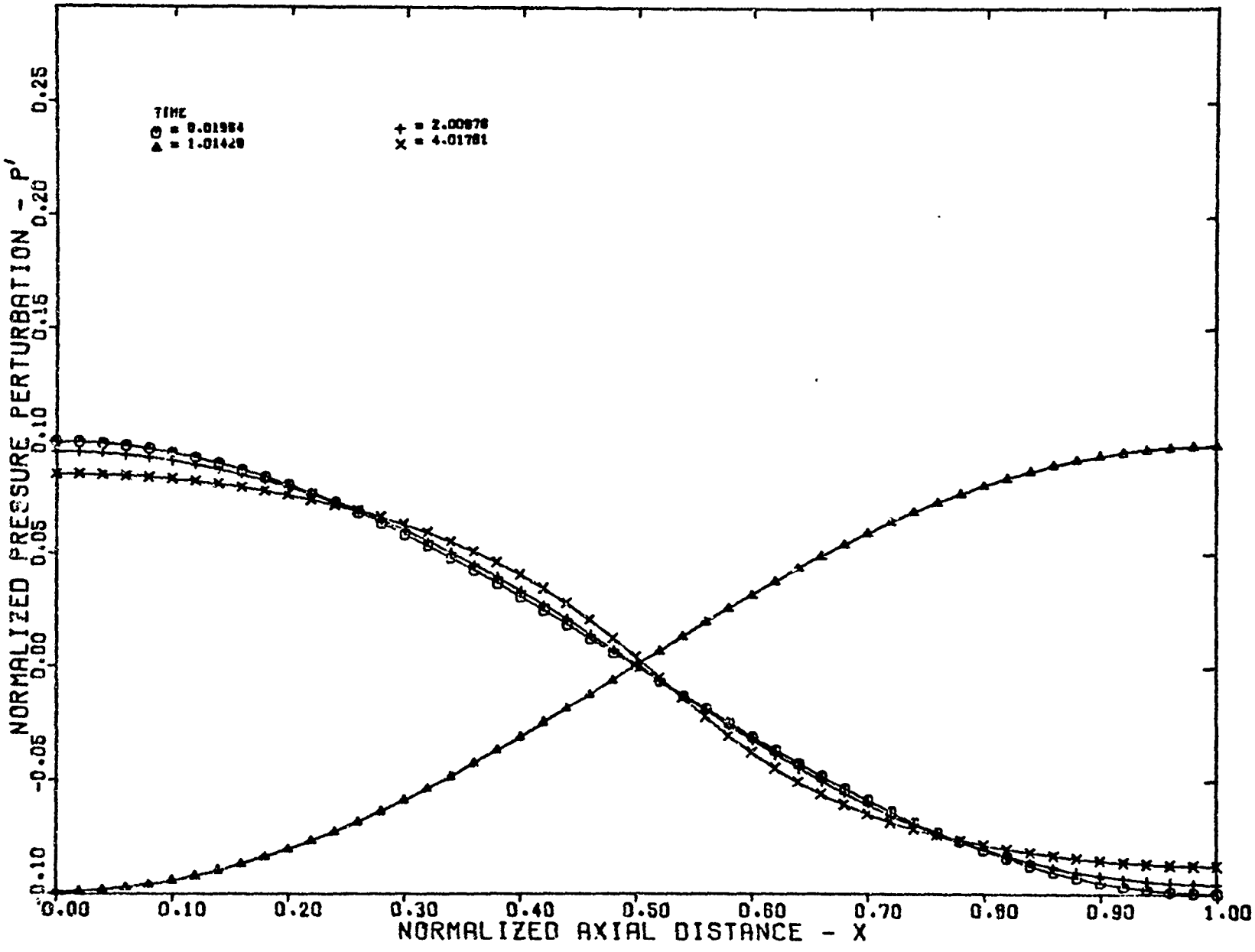

Figure 9-3. Wave In A Closed Tube - No Particles, $P_0' = .1 \cos(\pi x)$

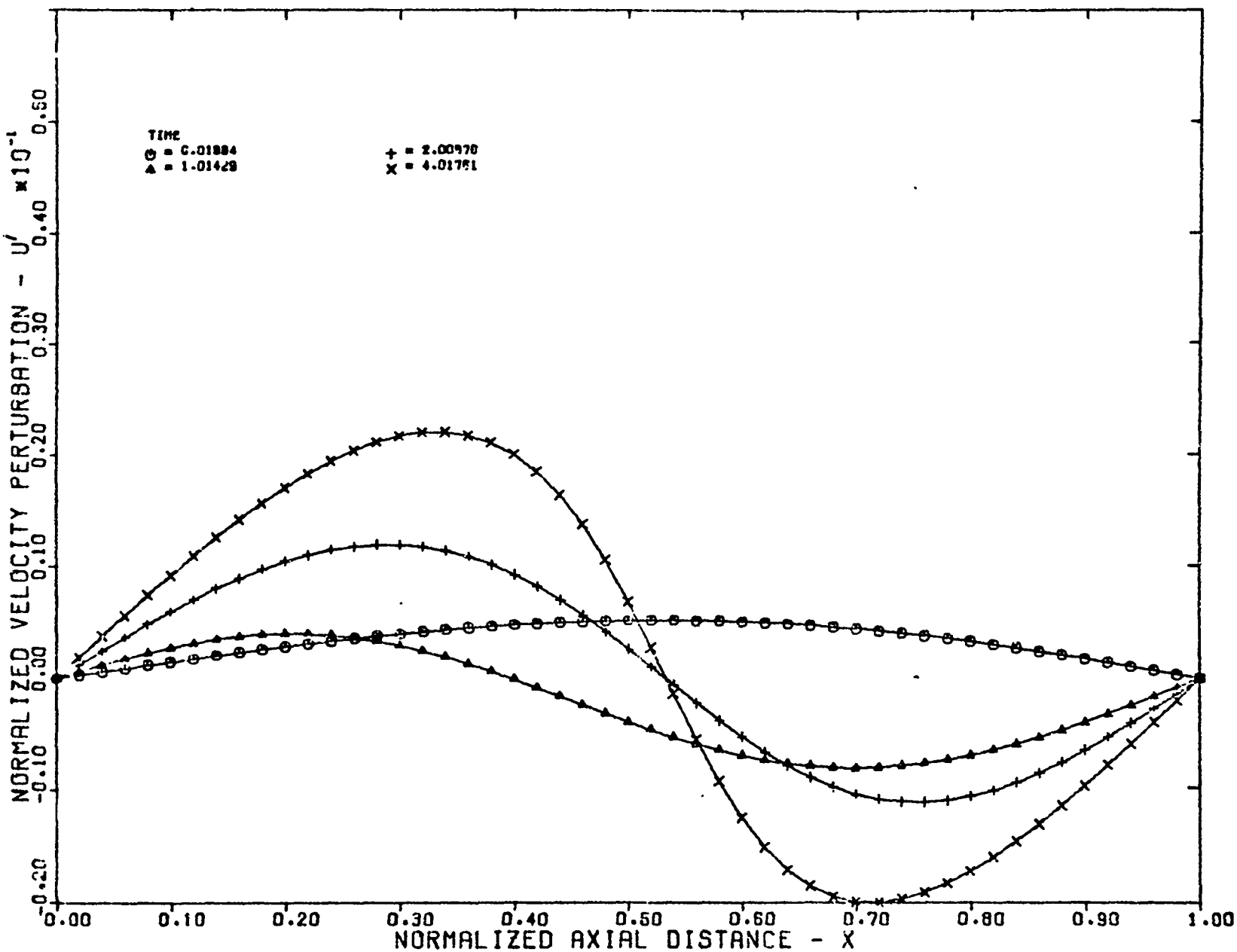

Figure 9-4. Wave In A Closed Tube - No Particles, $P' = .1 \cos(\pi x)$

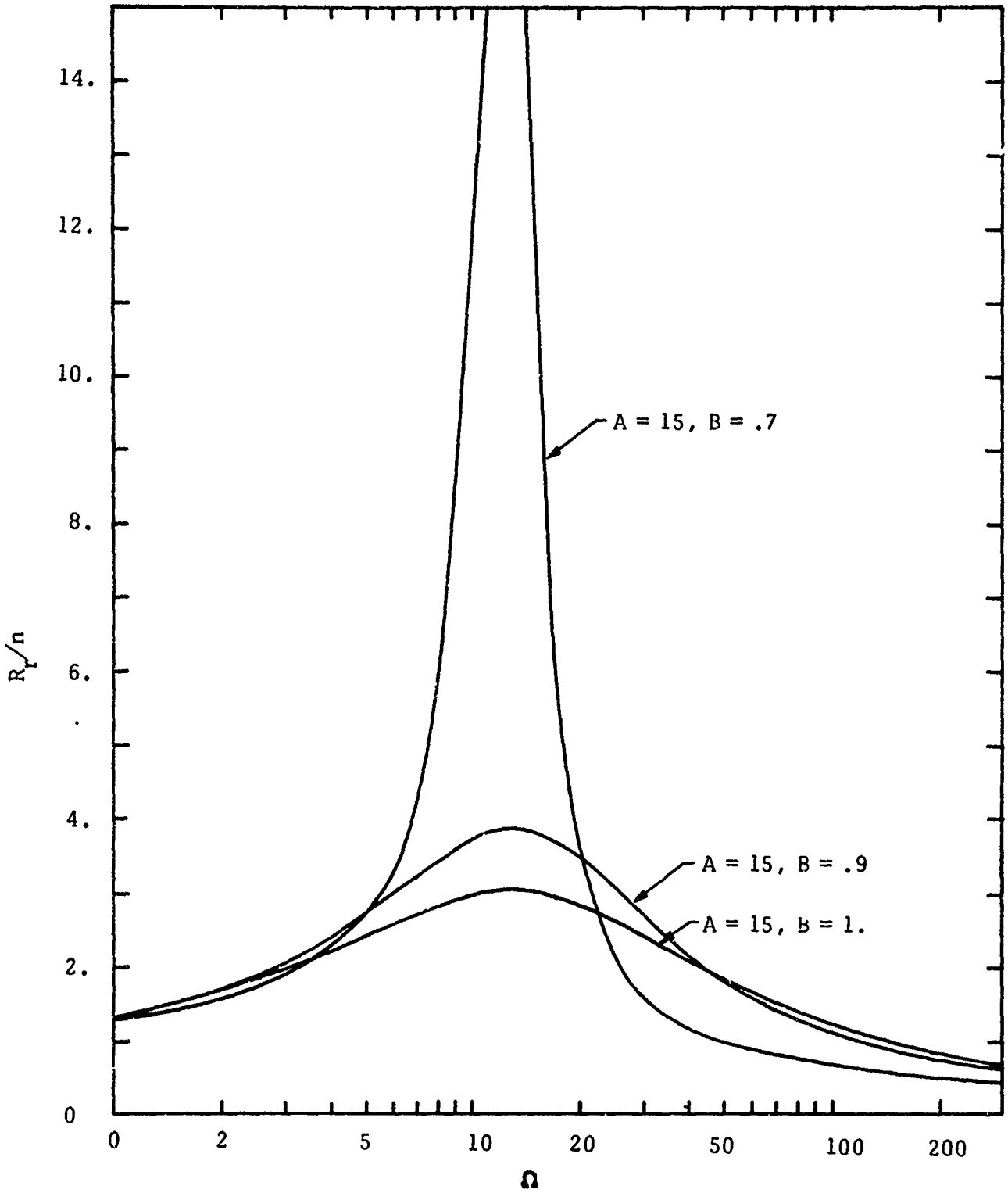

Figure 9-5. Real Part of Response Function versus Nondimensional Frequency

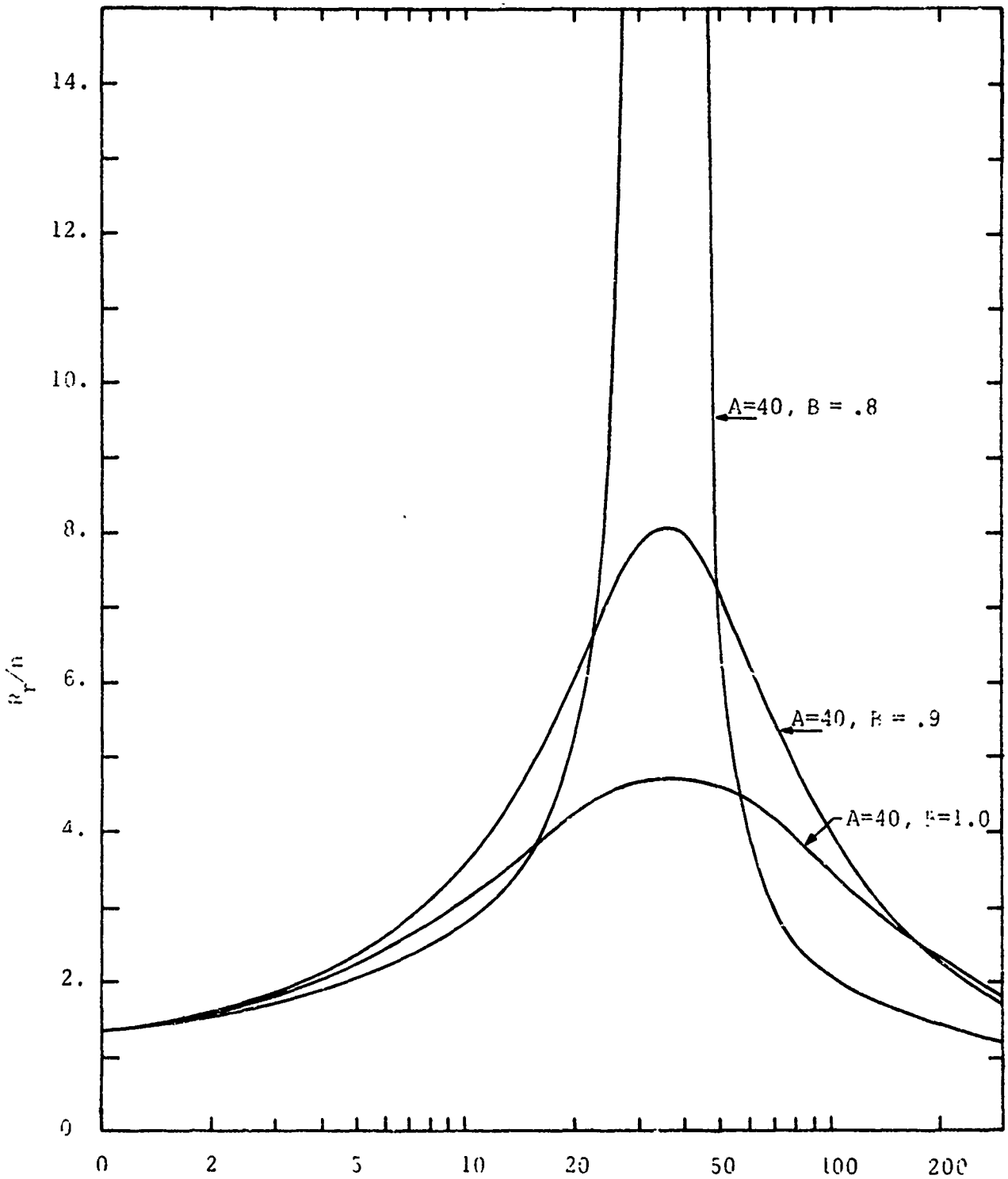

Figure 9-6. Real Part of Response Function versus Nondimensional Frequency

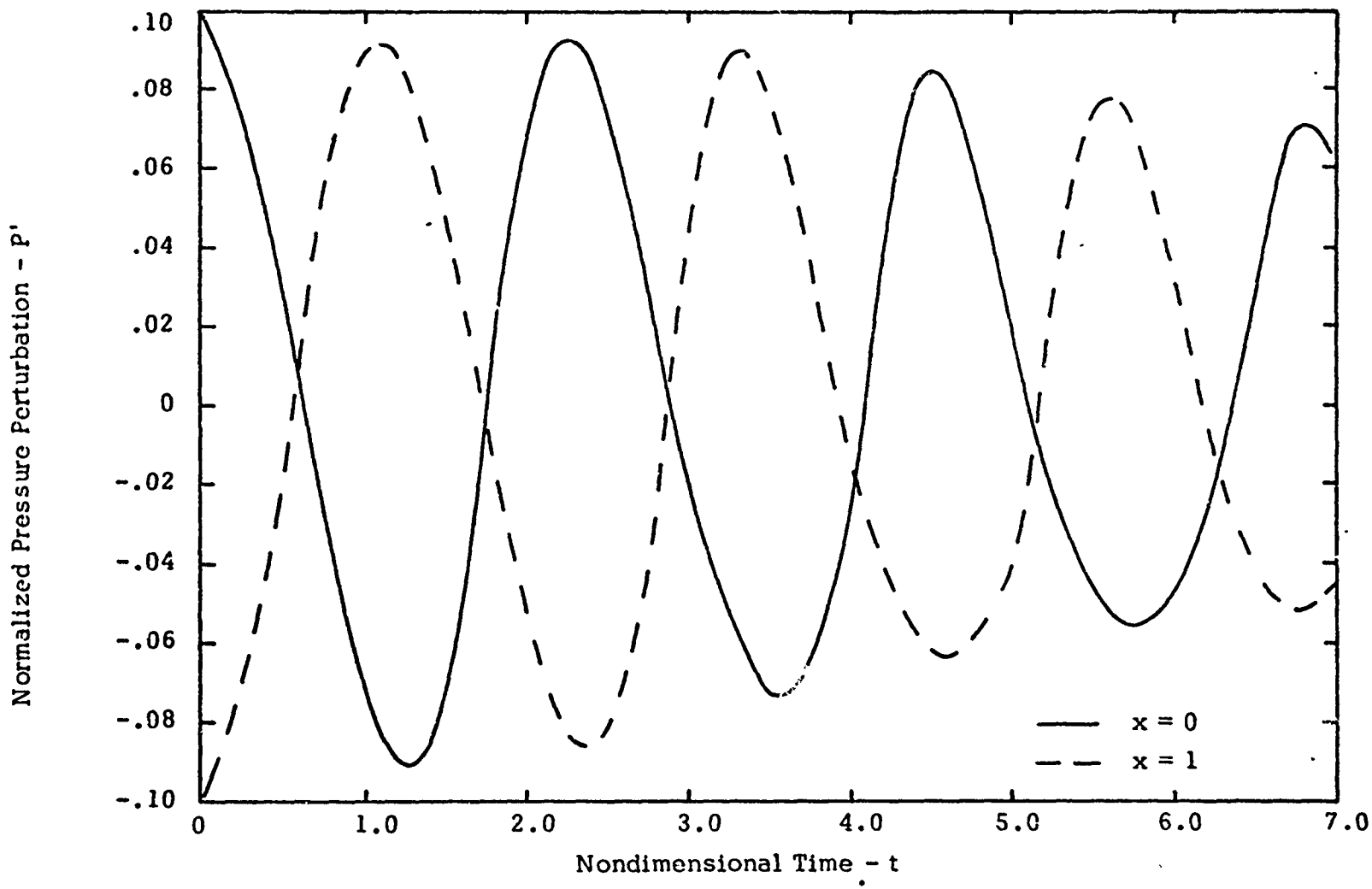

Figure 9-7. Pressure History At Head and Aft Ends of Grain
$A = 15$, $B = .7$, $P_0' = .1 \cos(\pi x)$, 2 μ Particles

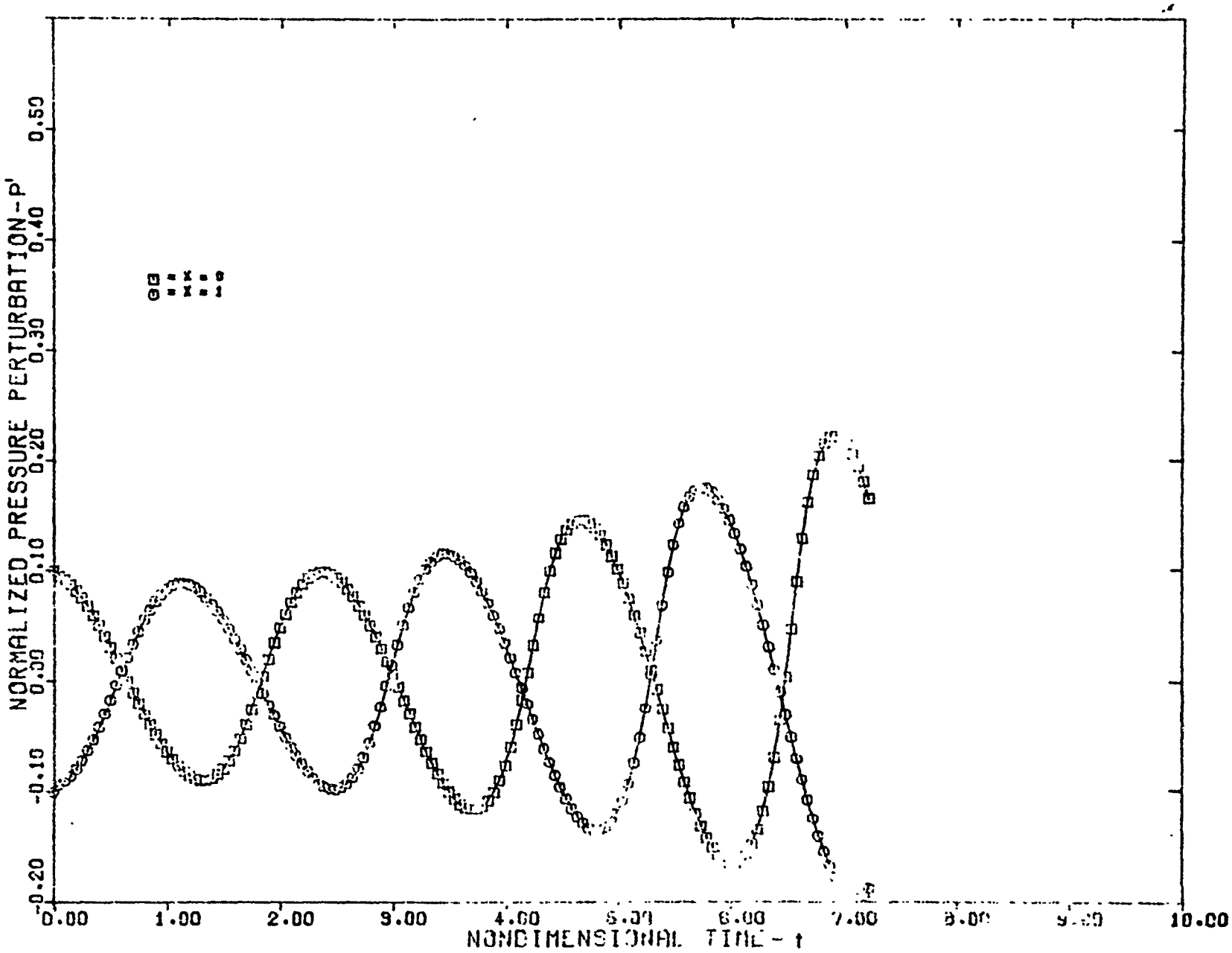

Figure 9-8. Pressure History At Head and Aft Ends of Grain
$A = 11.5$, $B = .64$, $P_0' = .1 \cos(\pi x)$, 2 μ Particles

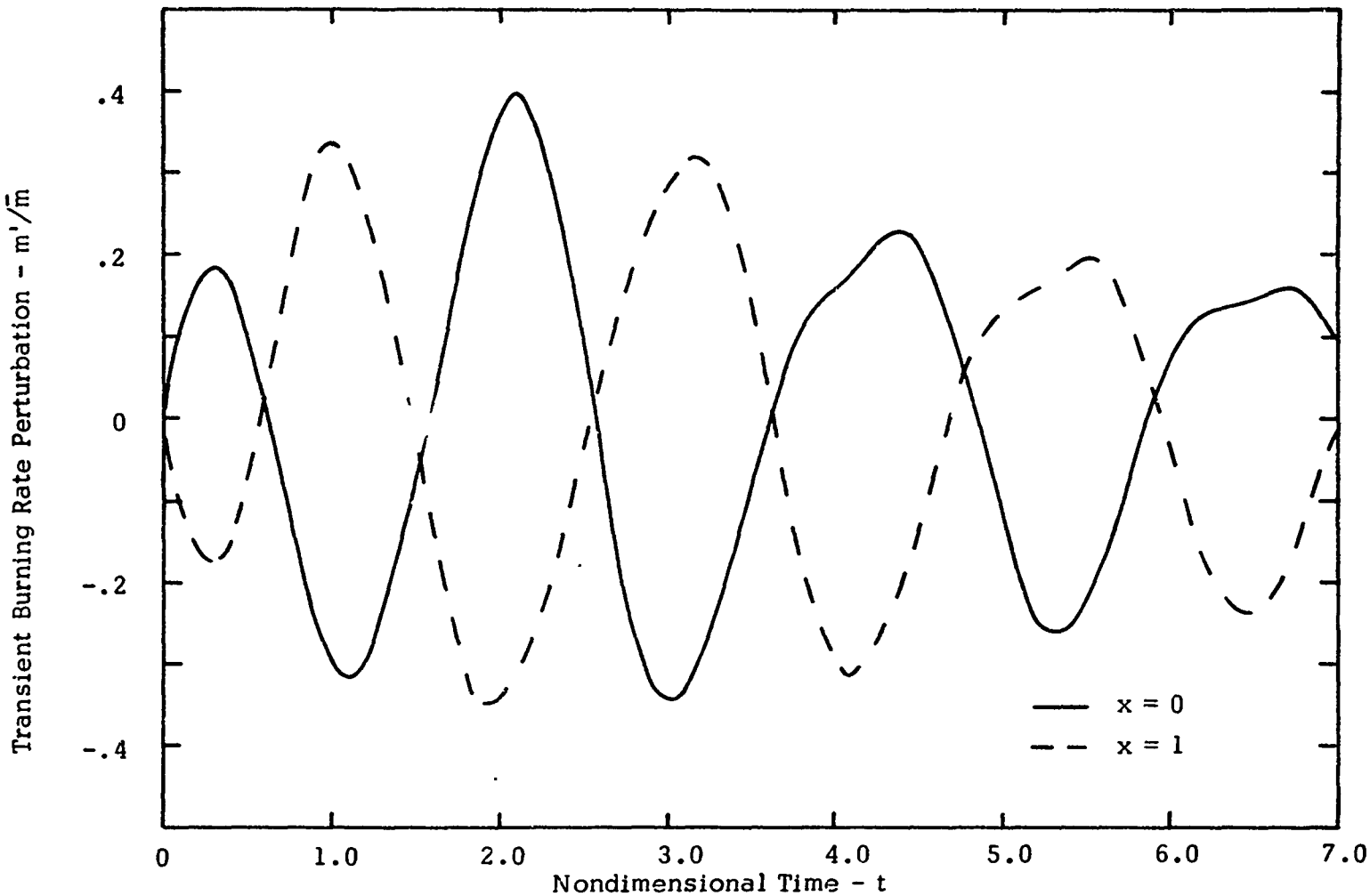

Figure 9-9. Transient Burning Rate History At Head and Aft Ends of Grain
$A = 15$, $B = .7$, $P_0' = .1 \cos(\pi x)$, 2 μ Particles

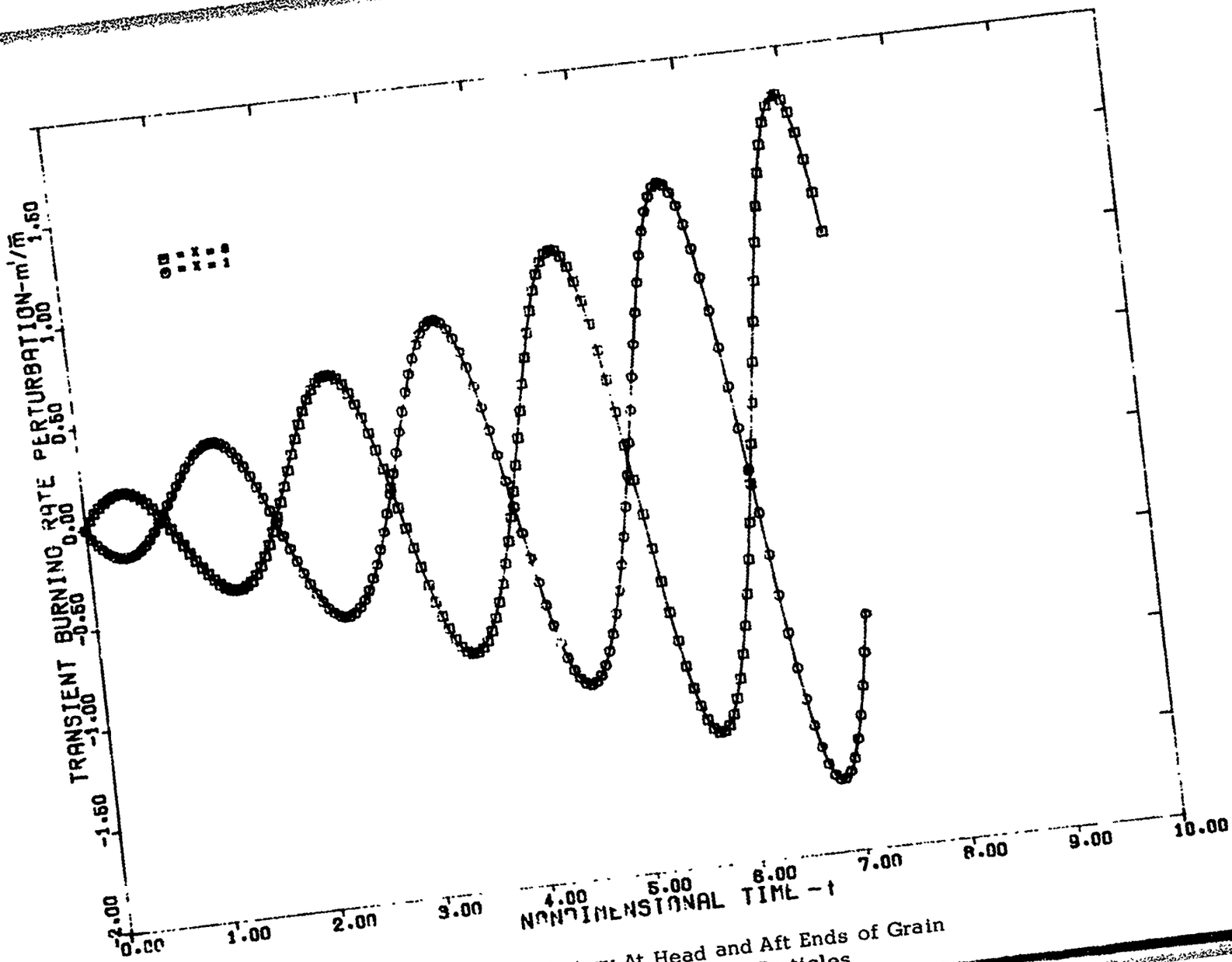

Figure 9-10. Transient Burning Rate History At Head and Aft Ends of Grain
$A = 11.5$, $B = .64$, $P_0' = .1 \cos(\pi x)$, 2 μ Particles

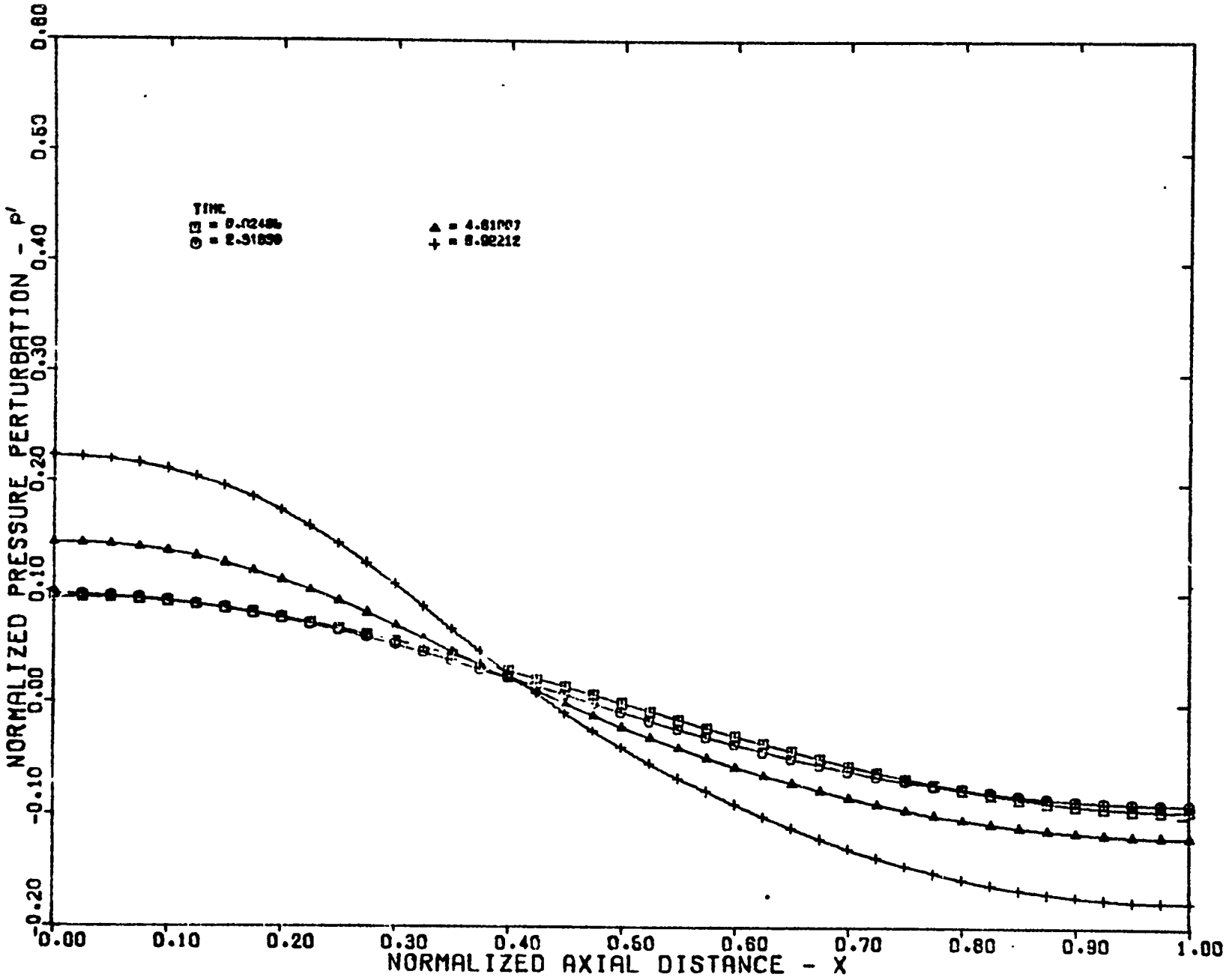

Figure 9-11. Pressure Waveform In the Chamber
$A = 11.5$, $B = .64$, $P_0' = .1 \cos(\pi x)$, 2 μ Particles

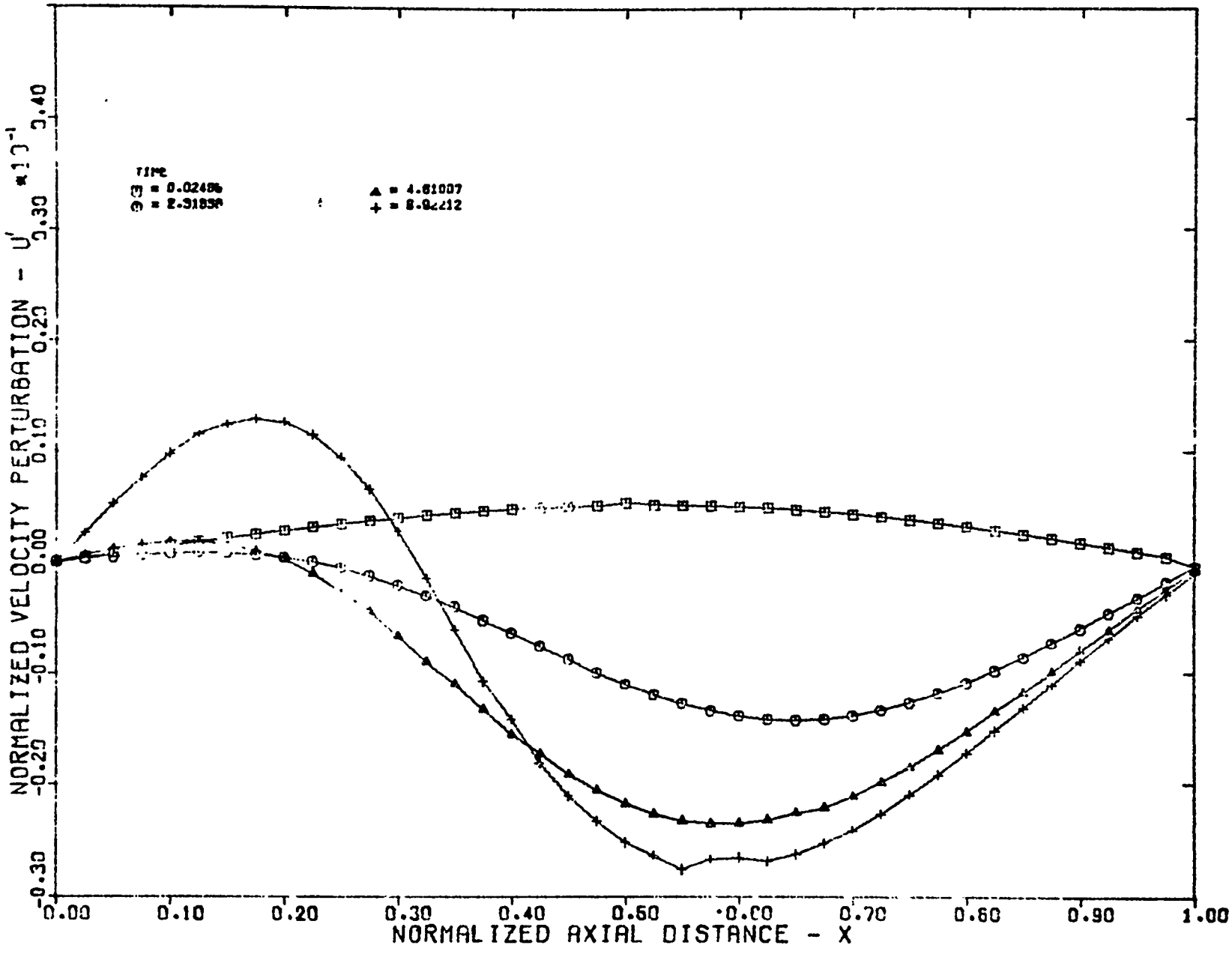

Figure 9-12. Velocity Waveform In The Chamber
$A = 11.5$, $B = .64$, $P_0' = .1 \cos(\pi x)$, $2\ \mu$ Particles

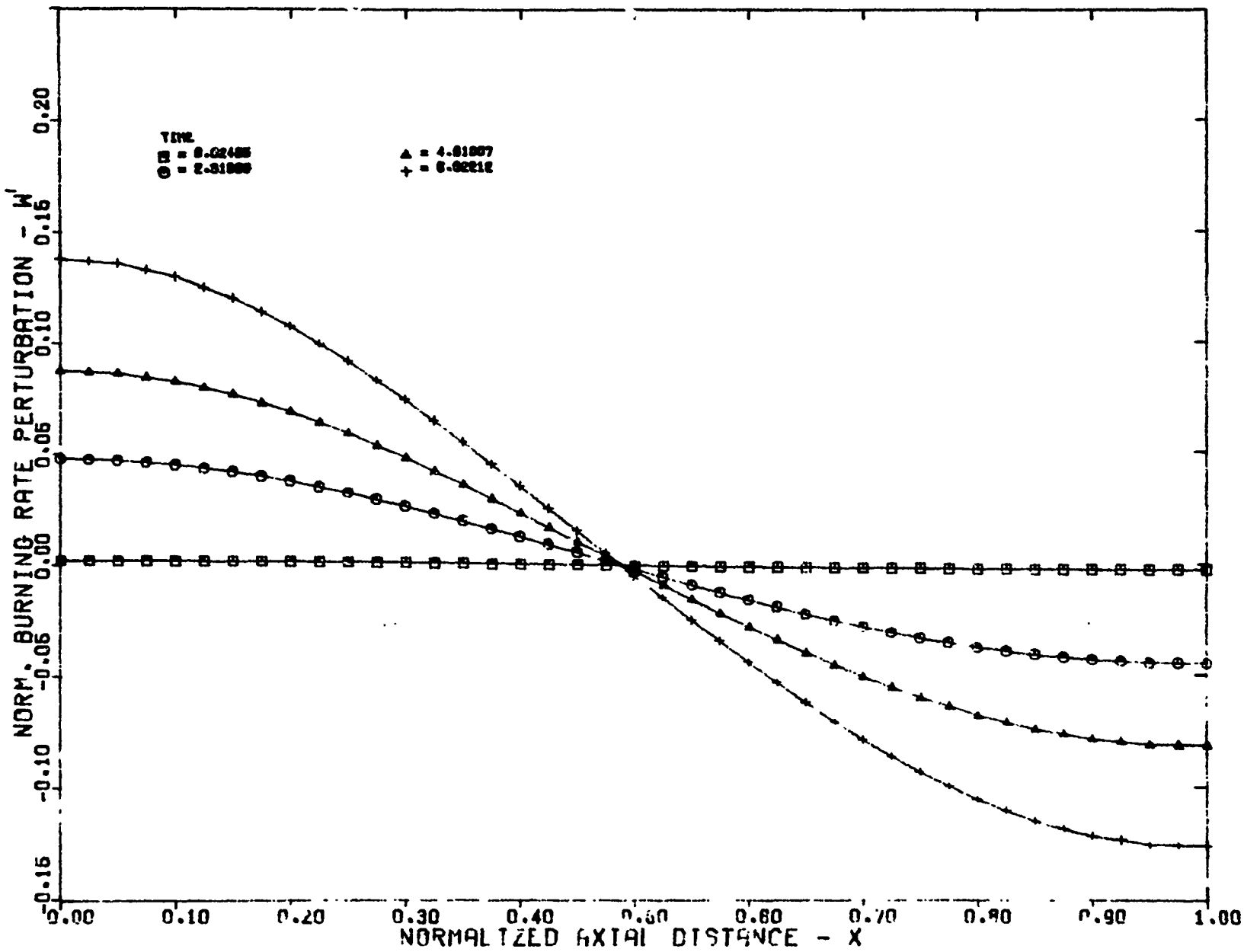

Figure 9-13. Burning Rate Waveform In The Chamber
$A = 11.5$, $B = .64$, $P_0' = .1 \cos(\pi x)$, 2 μ Particles

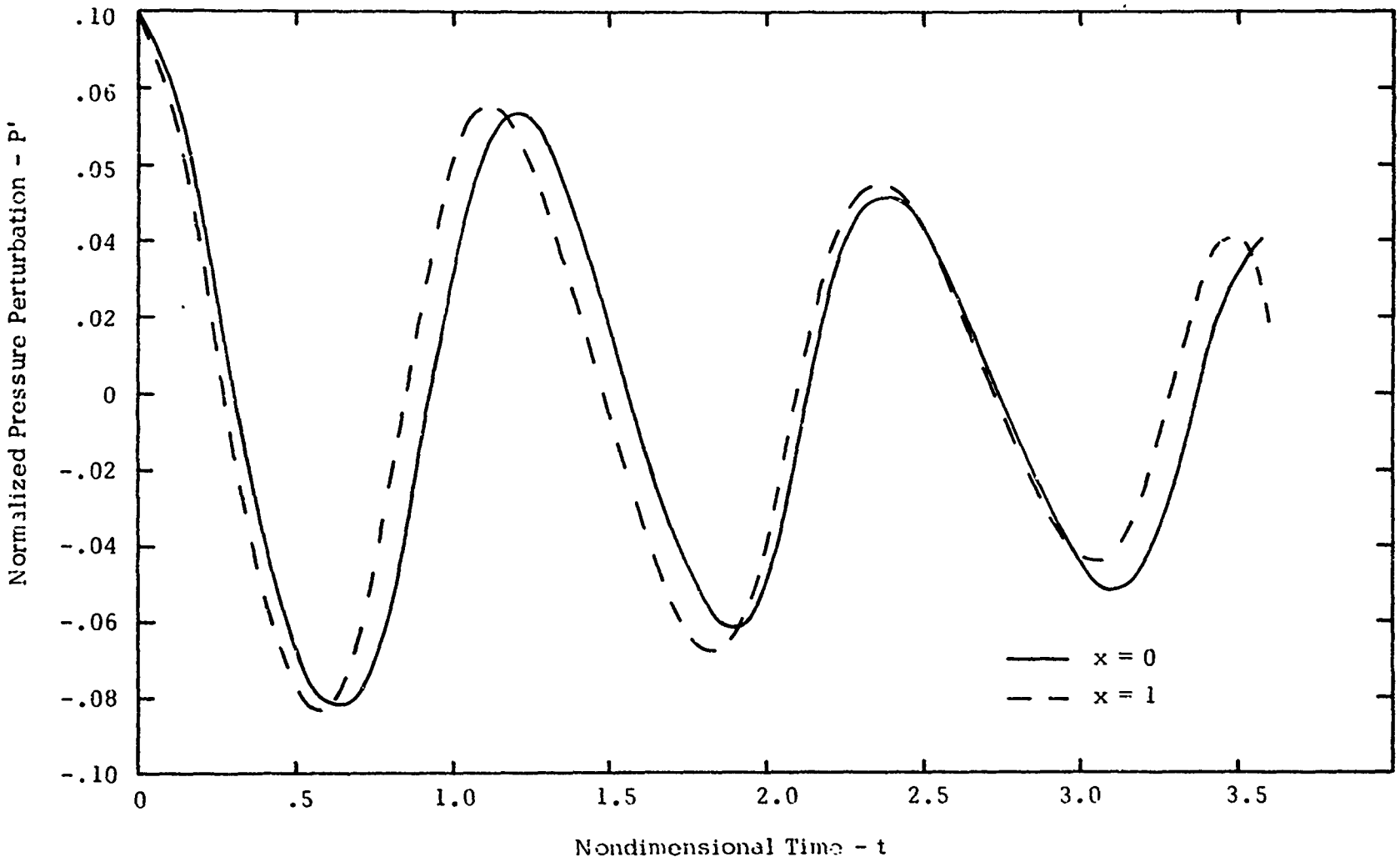

Figure 9-14. Pressure History At Head and Aft Ends of Grain
$A = 11.5$, $B = .64$, $P'_0 = .1 \cos(2\pi x)$, 2 μ Particles

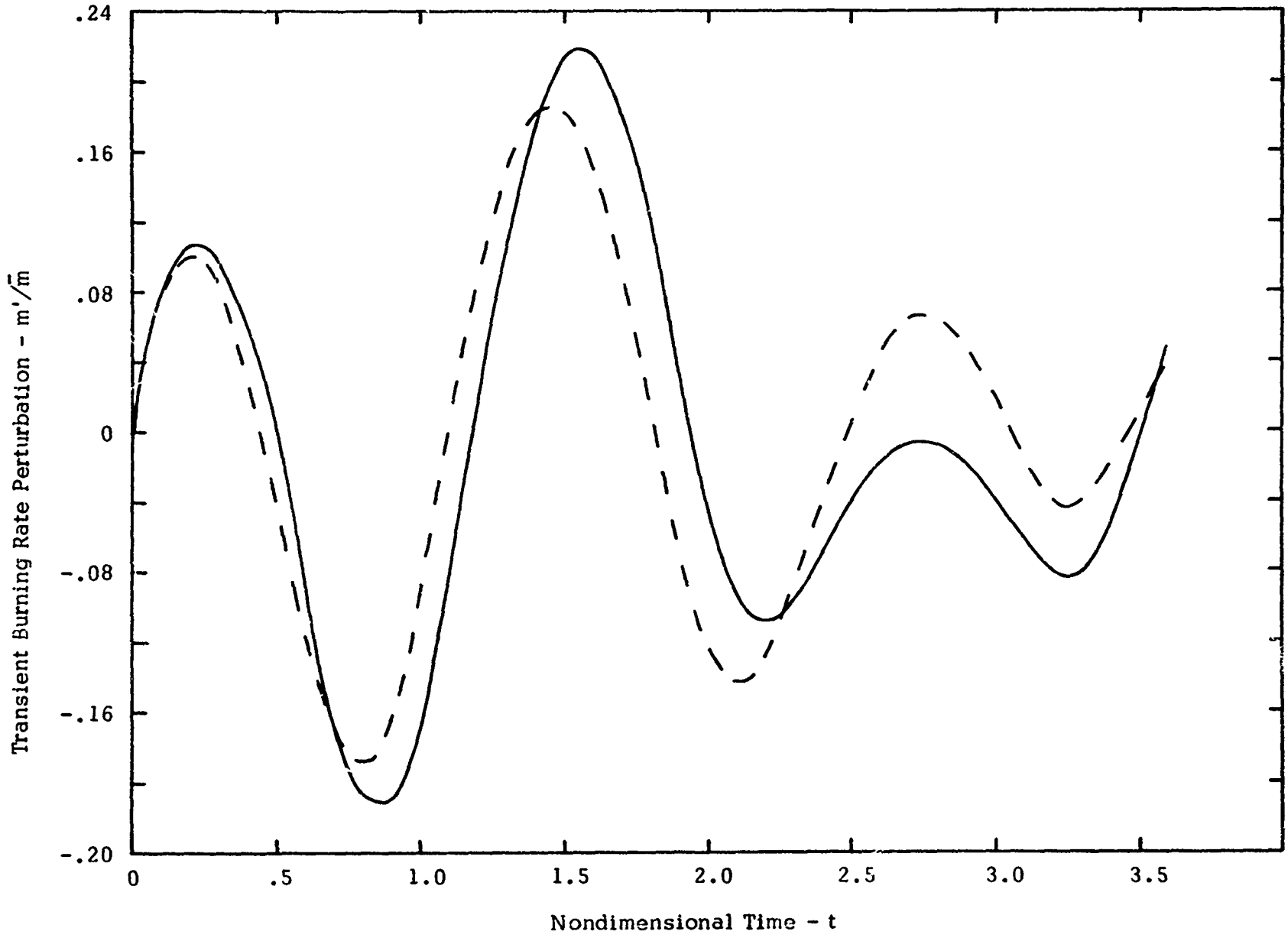

Figure 9-15. Transient Burning Rate History At Head and Aft Ends of Grain
$A = 11.5$, $B = .64$, $P_0' = .1 \cos(2\pi x)$, 2 μ Particles

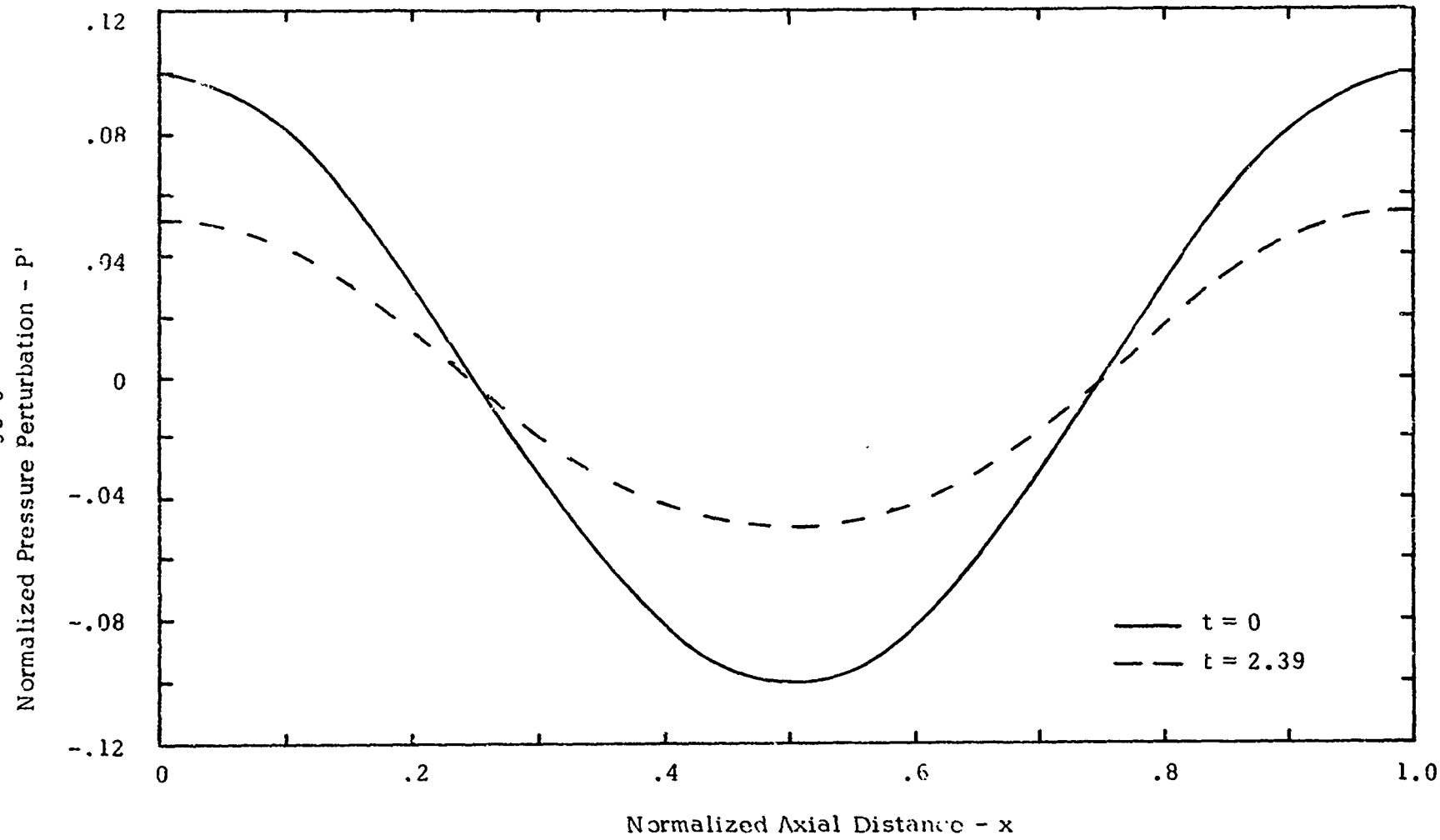

Figure 9-16. Pressure Waveform In The Chamber
$\Lambda = 11.5$, $B = .64$, $P'_0 = .1 \cos(2\pi x)$, 2 μ Particles

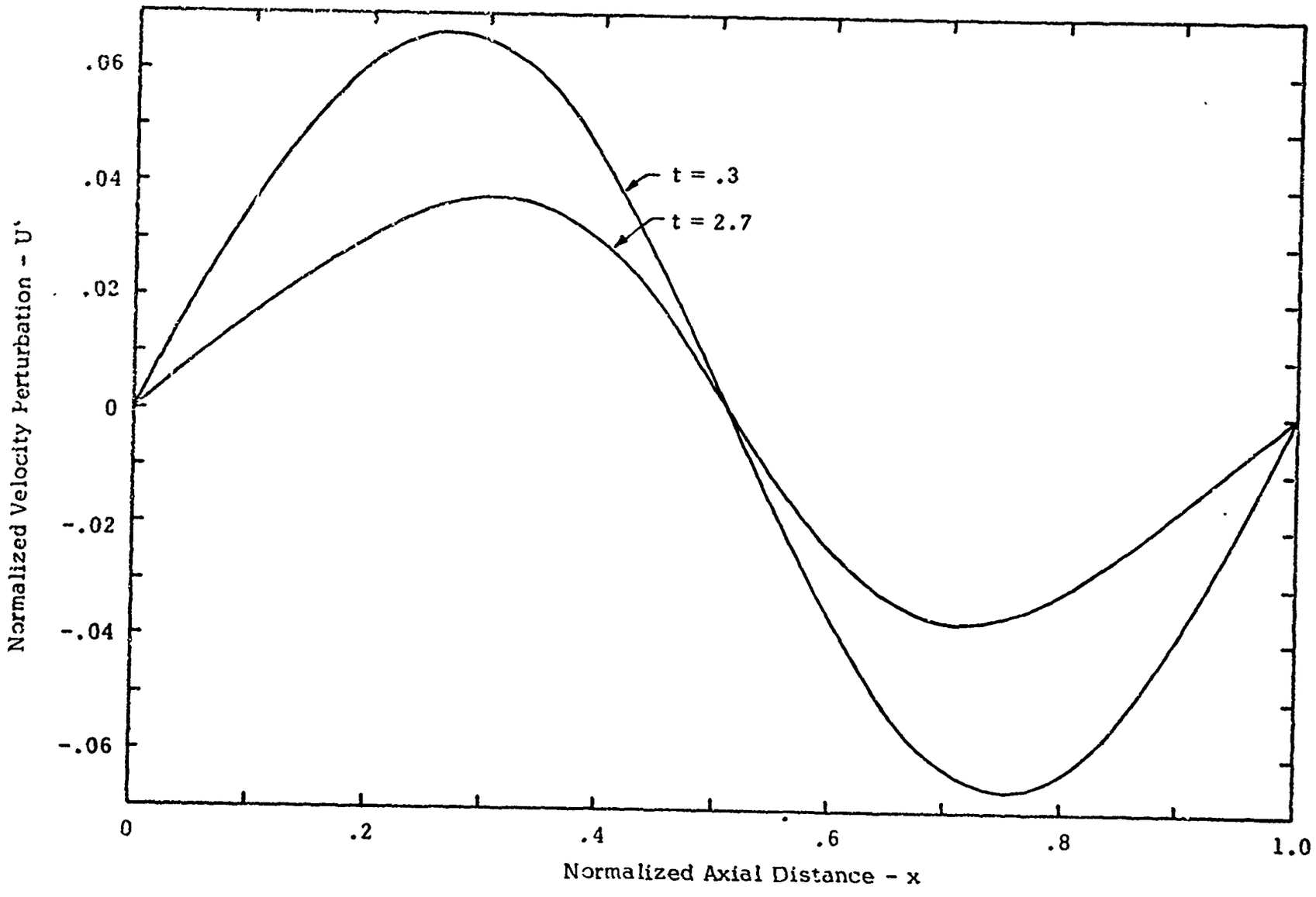

Figure 9-17. Velocity Waveform In The Chamber
$A = 11.5$, $B = .64$, $P_0' = .1 \cos(2\pi x)$, $2\ \mu$ Particles

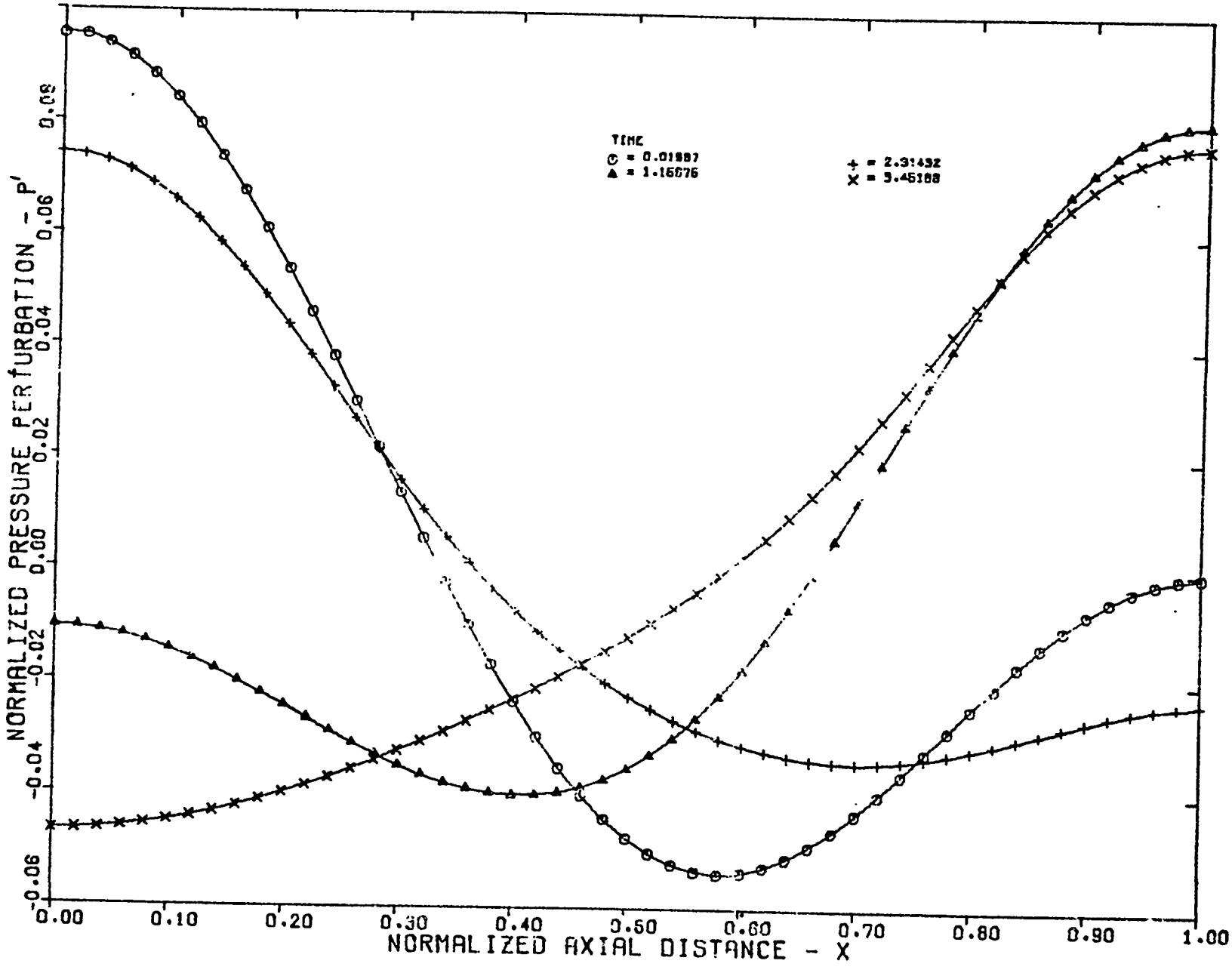

Figure 9-18a. Pressure Waveform In The Chamber
$A = 11.5$, $B = .64$, $P_0' = .05\ [\cos(\pi x) + \cos(2\pi x)]$, 2 μ Particles

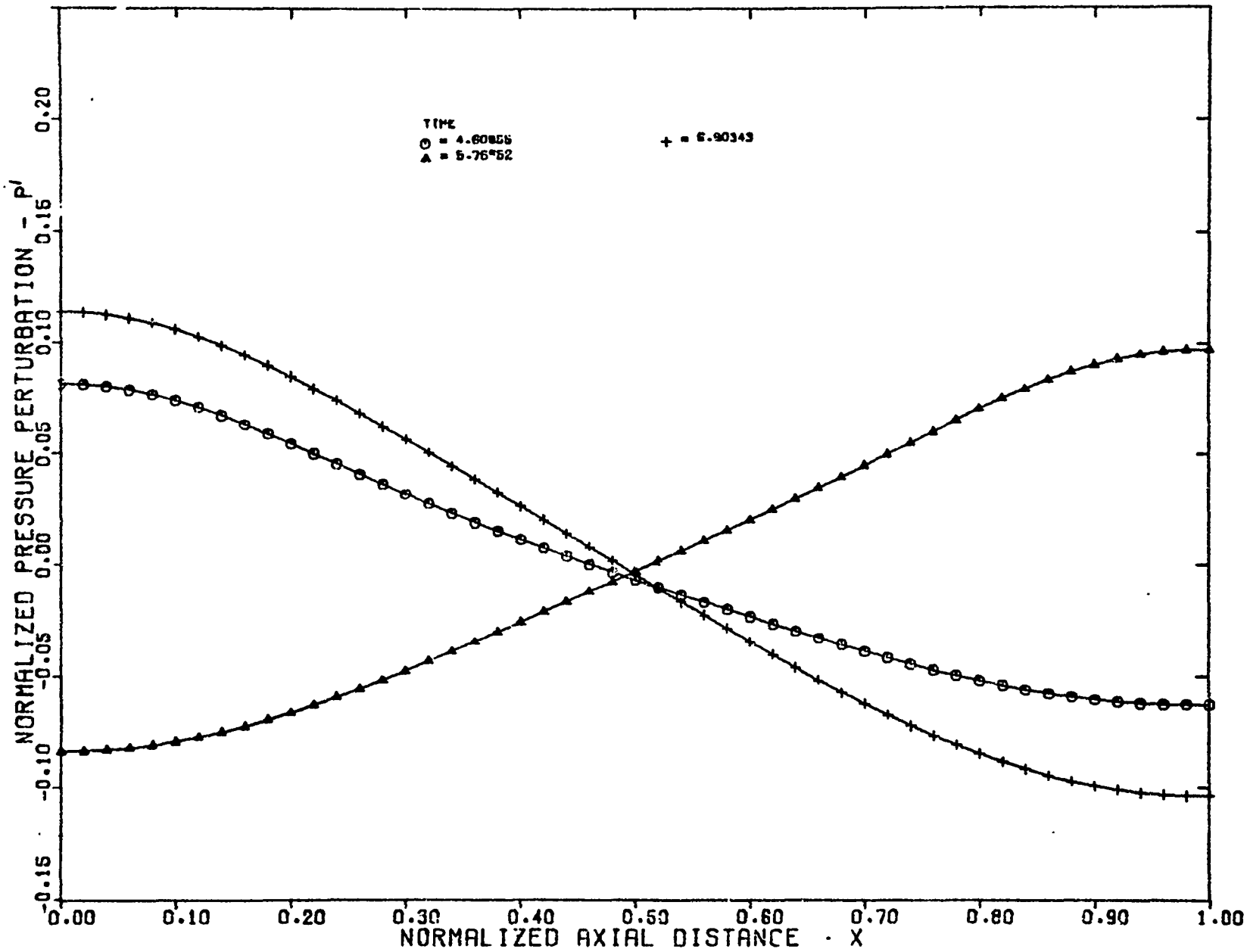

Figure 9-18b. Pressure Waveform In The Chamber
$A = 11.5$, $B = .64$, $P_0' = .05\ [\cos(\pi x) + \cos(2\pi x)]$, 2 μ Particles

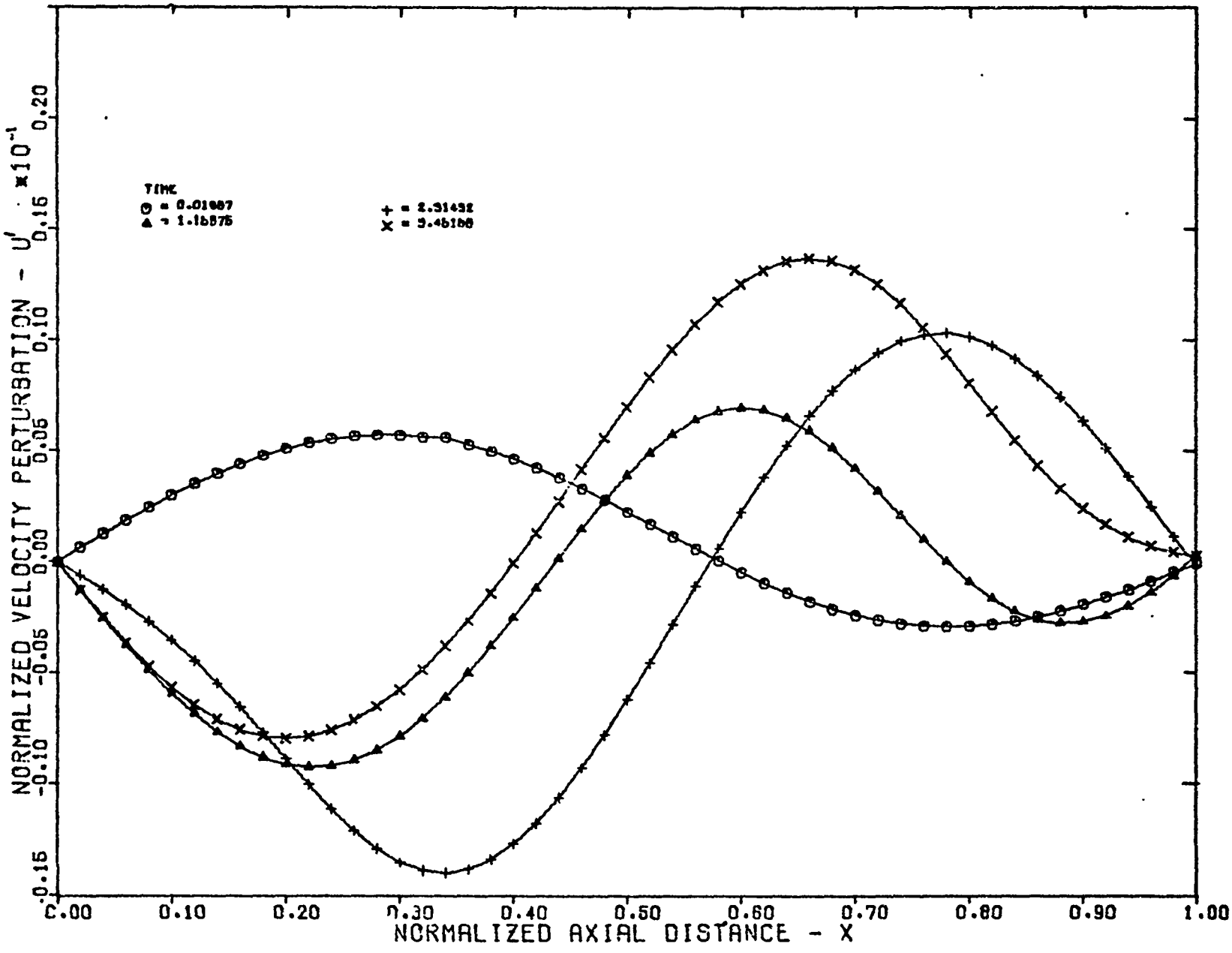

Figure 9-19a. Velocity Waveform In The Chamber
$A = 11.5$, $B = .64$, $P_0' = .05\,[\cos(\pi x) + \cos(2\pi x)]$, 2 μ Particles

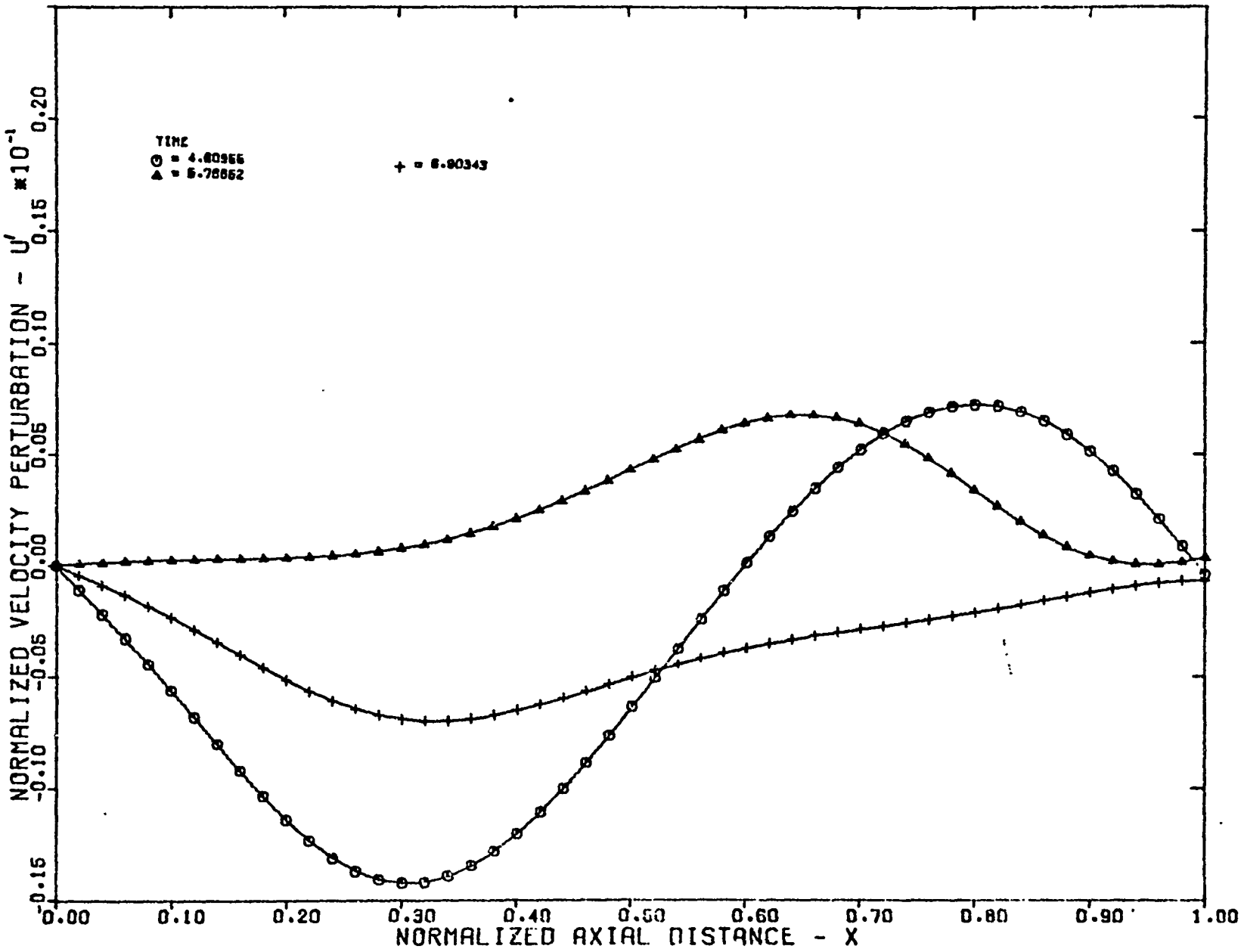

Figure 9-19b. Velocity Waveform In The Chamber
$A = 11.5$, $B = .64$, $P_0' = .05\,[\cos(\pi x) + \cos(2\pi x)]$, 2 μ Particles

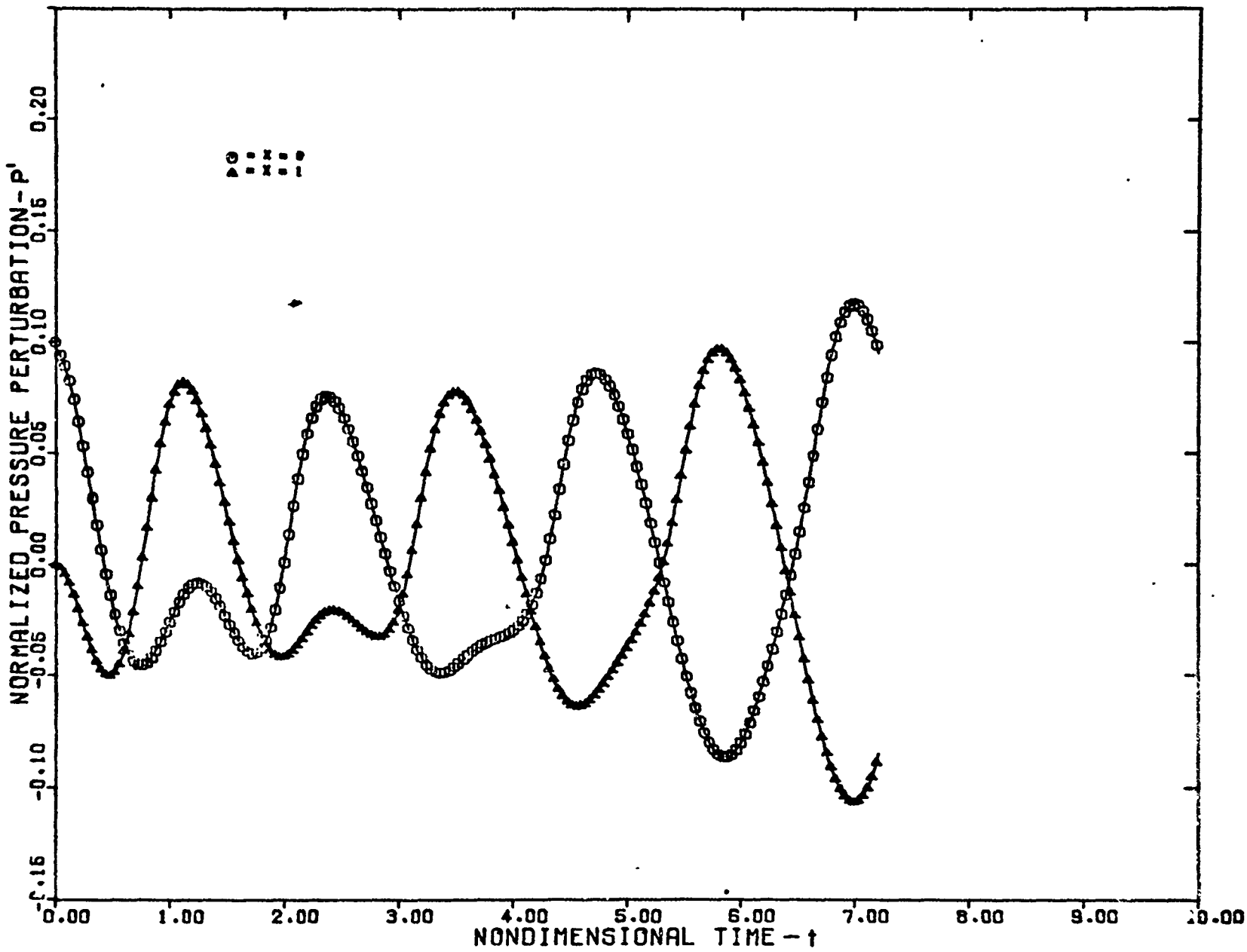

Figure 9-20. Pressure History At Head and Aft Ends of Grain
$A = 11.5$, $B = .64$, $P_0' = .05\ [\cos(\pi x) + \cos(2\pi x)]$, 2 μ Particles

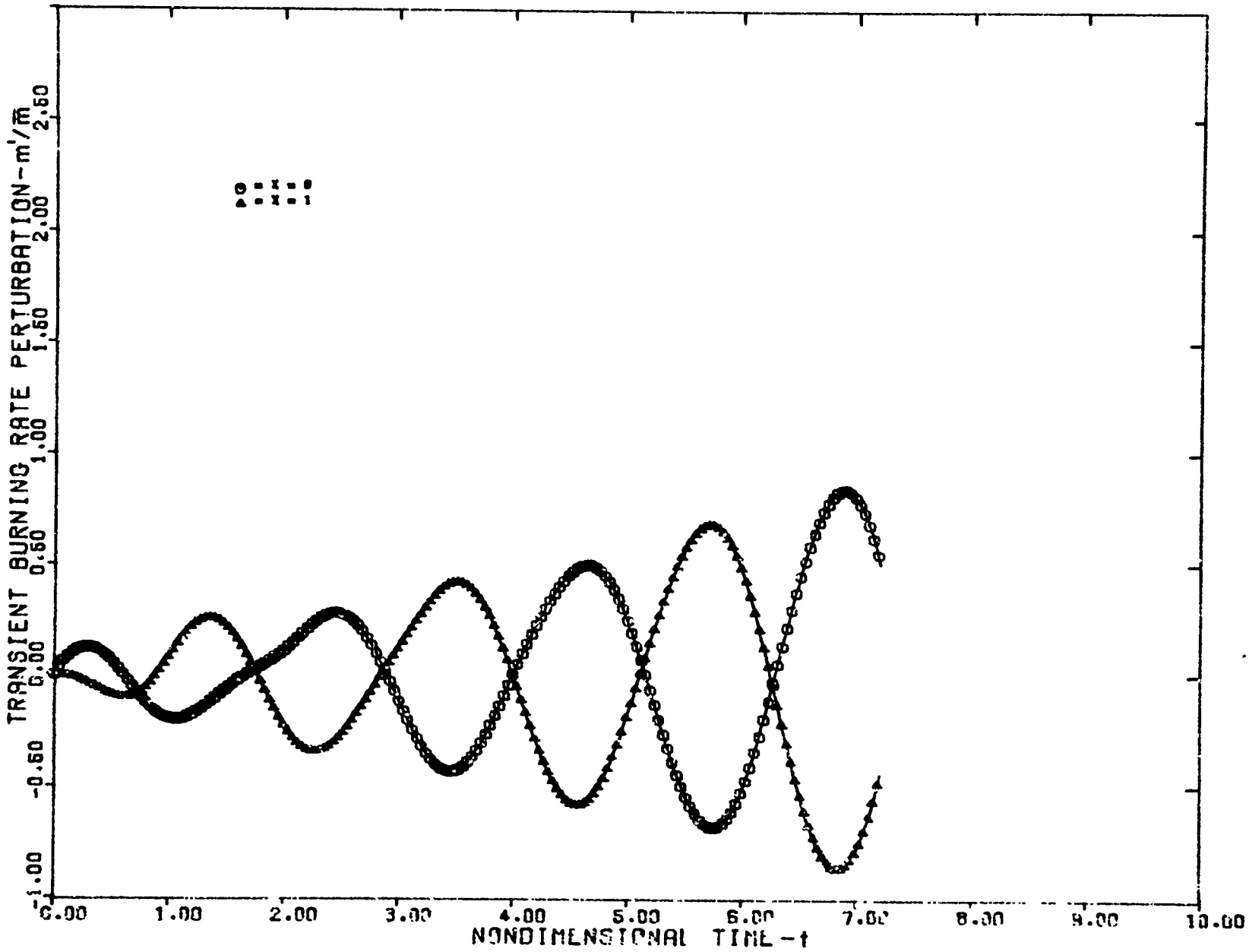

Figure 9-21. Transient Burning Rate History At Head and Aft Ends of Grain
$A = 11.5$, $B = .64$, $P_0' = .05\ [\cos(\pi x) + \cos(2\pi x)]$, 2 μ Particles

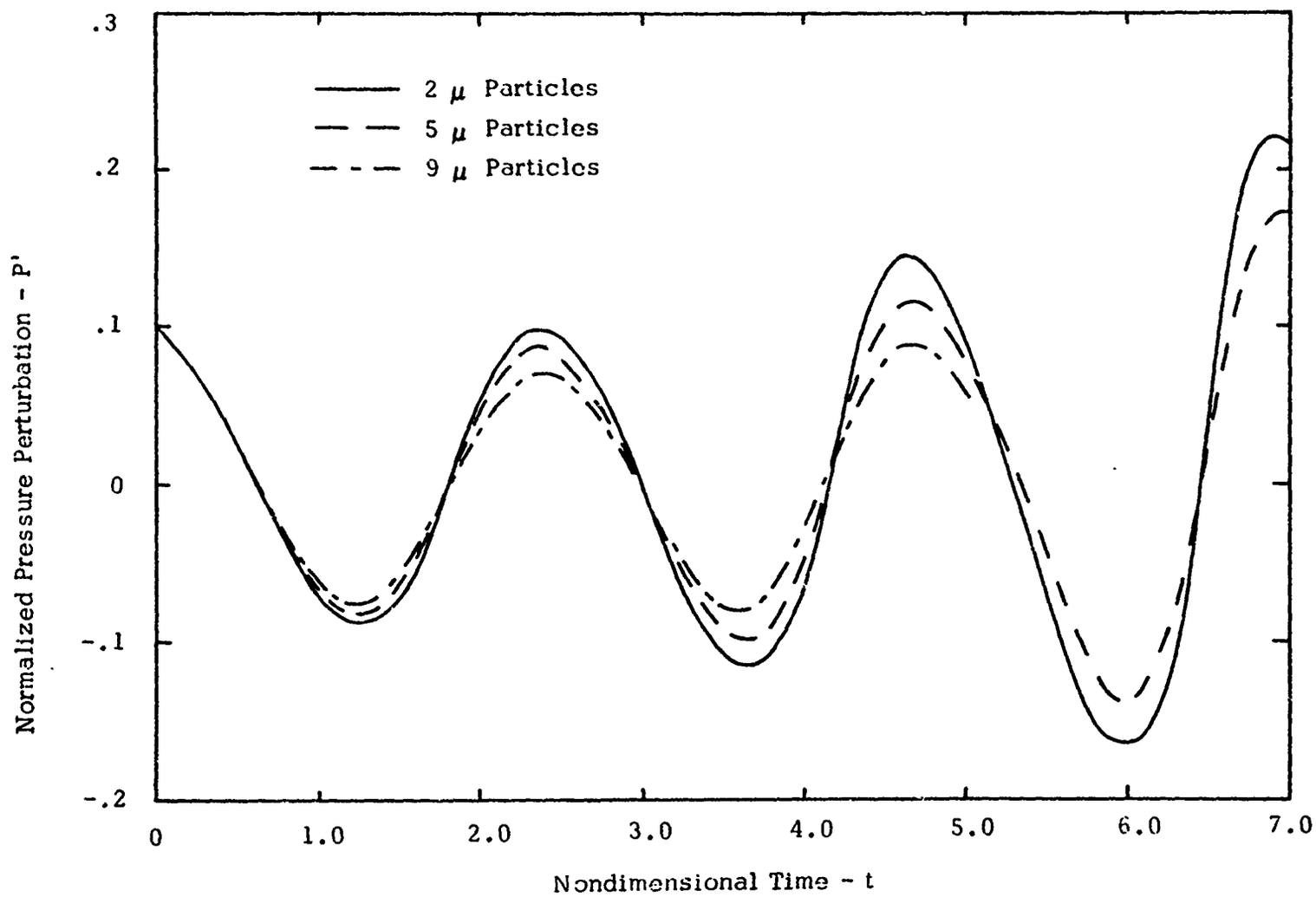

Figure 9-22. Effect Of Particle Size On Pressure History
At $x = 0$. $A = 11.5$, $B = .64$, $P'_0 = .1 \cos(\pi x)$

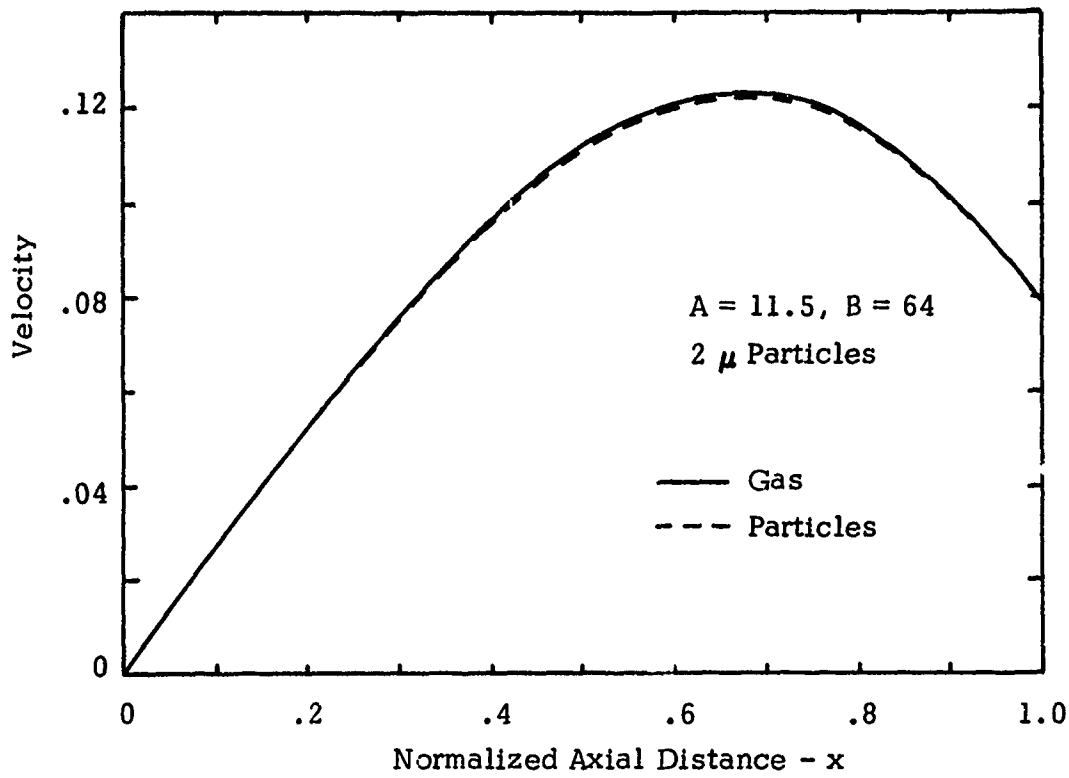

Figure 9-23. Comparison Between Particle and Gas Velocity, t = 2.9

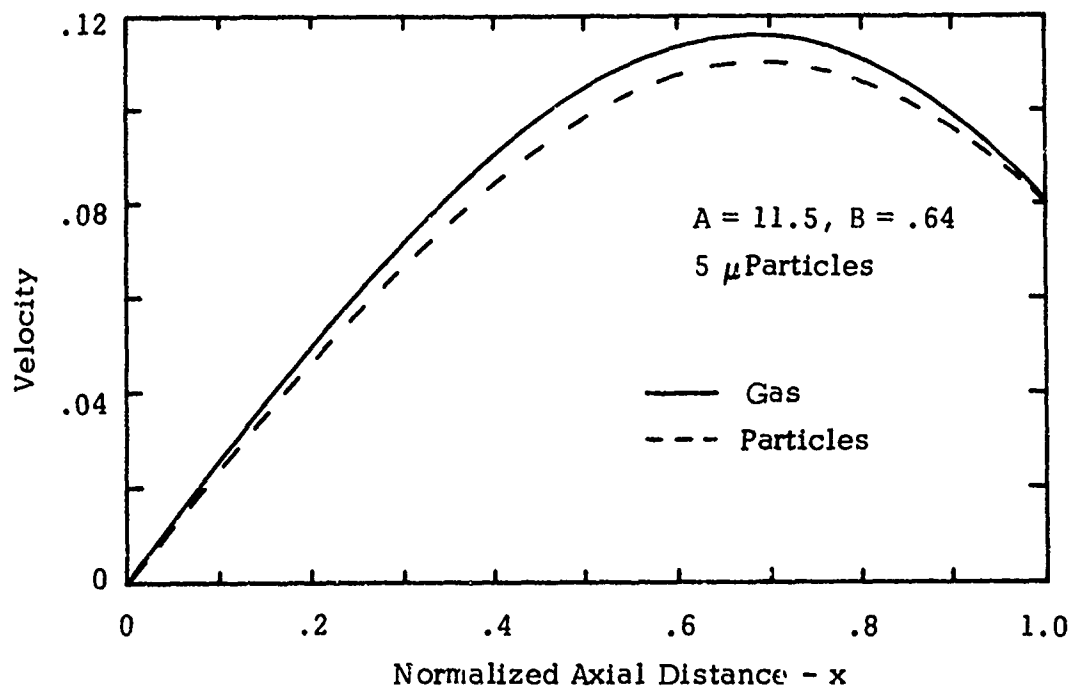

Figure 9-24. Comparison Between Particle and Gas Velocity, t = 2.9

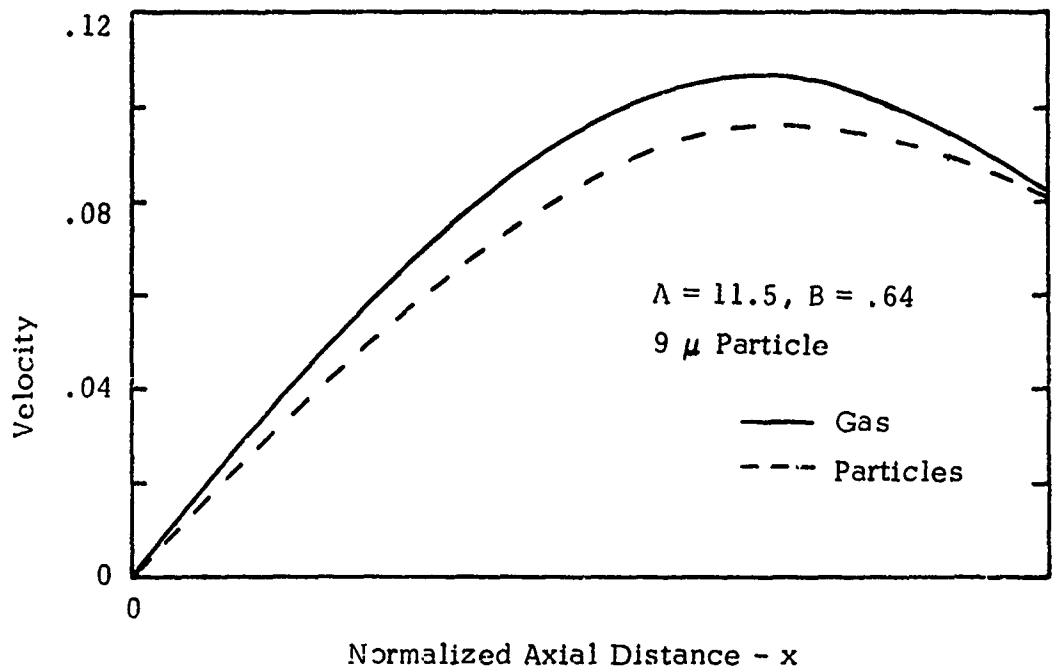

Figure 9-25. Comparison Between Particle and Gas Velocity, t = 2.9

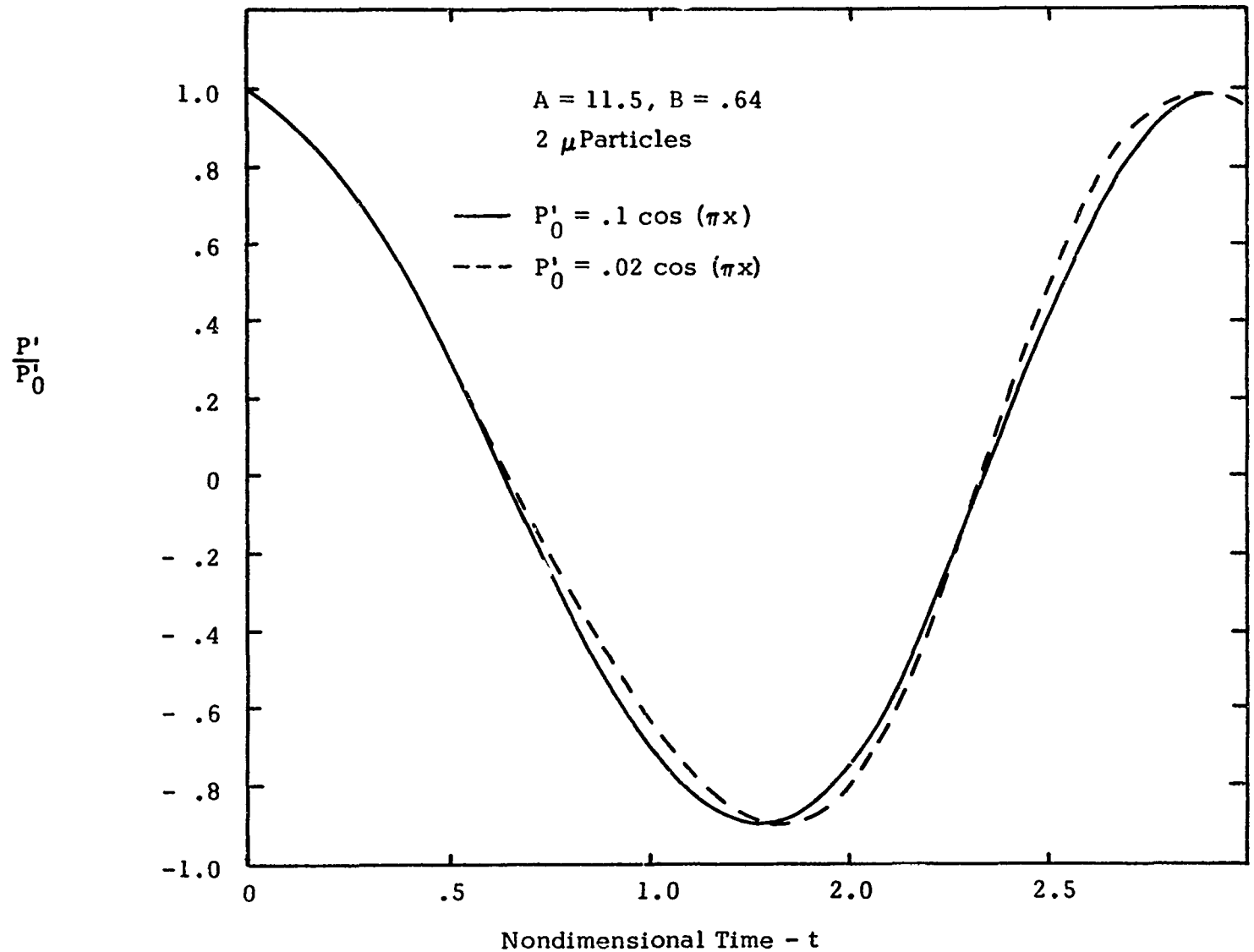

Figure 9-26. Effect of Amplitude On Pressure History At x = 0

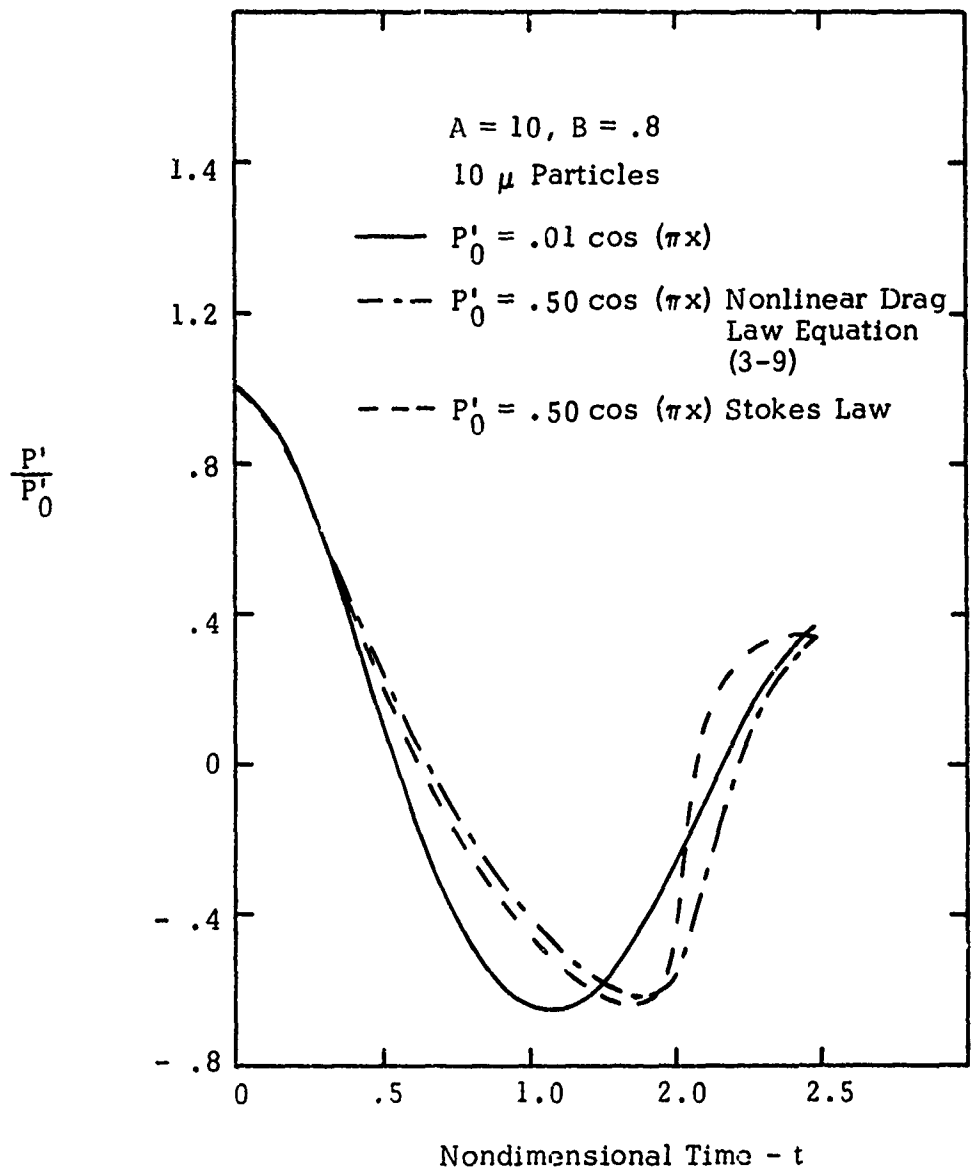

Figure 9-27. Effect of Amplitude and Drag Law On The Pressure History at x = 0

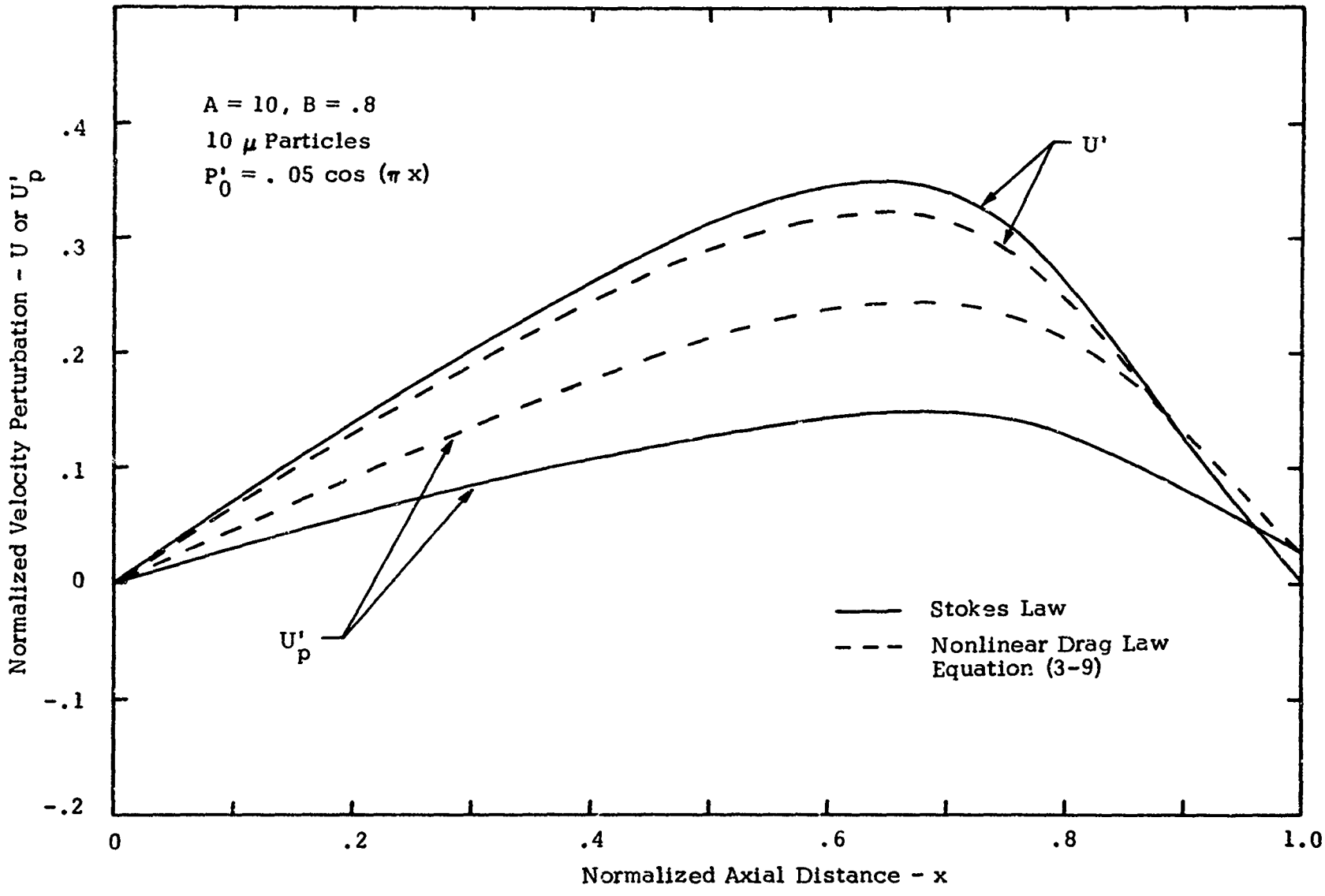

Figure 9-28. Effect of Drag Law On Particle Lag

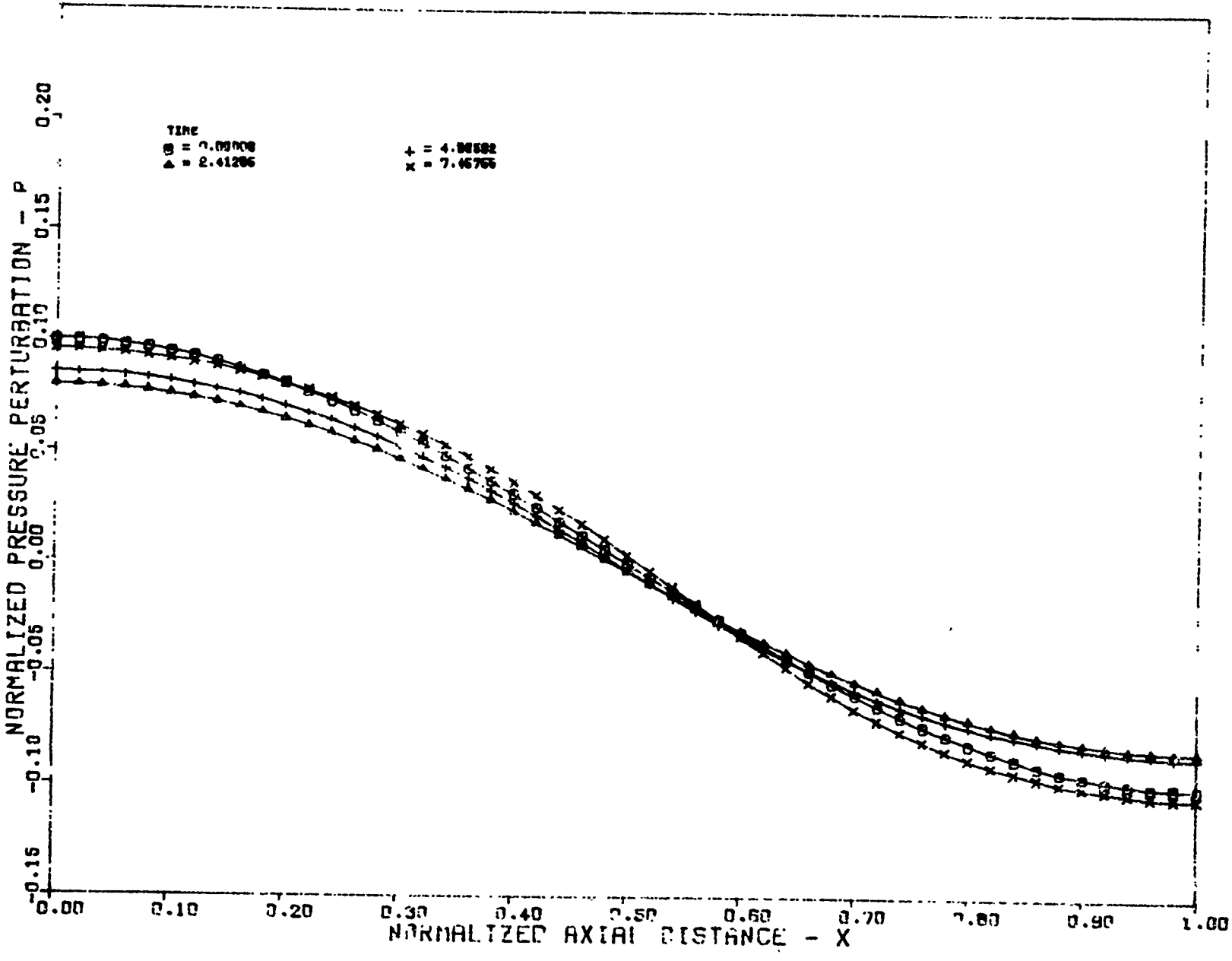

Figure 9-29. Pressure Waveform in the Chamber, Pressure and Velocity Coupling, $u_{th} = .04$
$A = 11.5$, $B = .64$, $P_0' = .1 \cos(\pi x)$, 2μ Particles

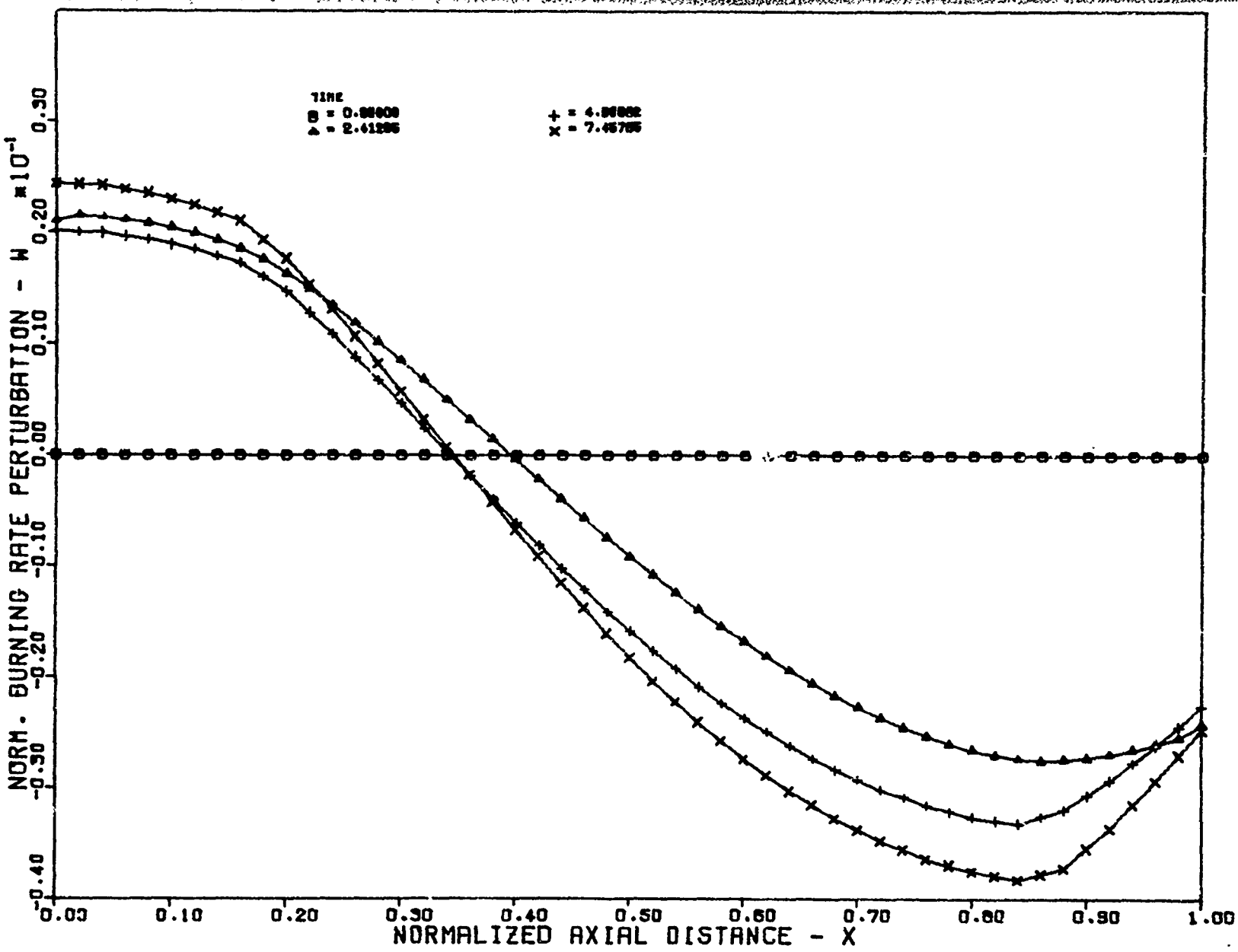

Figure 9-30. Burning Rate Waveform in the Chamber, Pressure and Velocity Coupling, $v_{th} = .04$
$A = 11.5$, $B = .64$, $P_0' = .1 \cos(\pi x)$, 2μ Particles

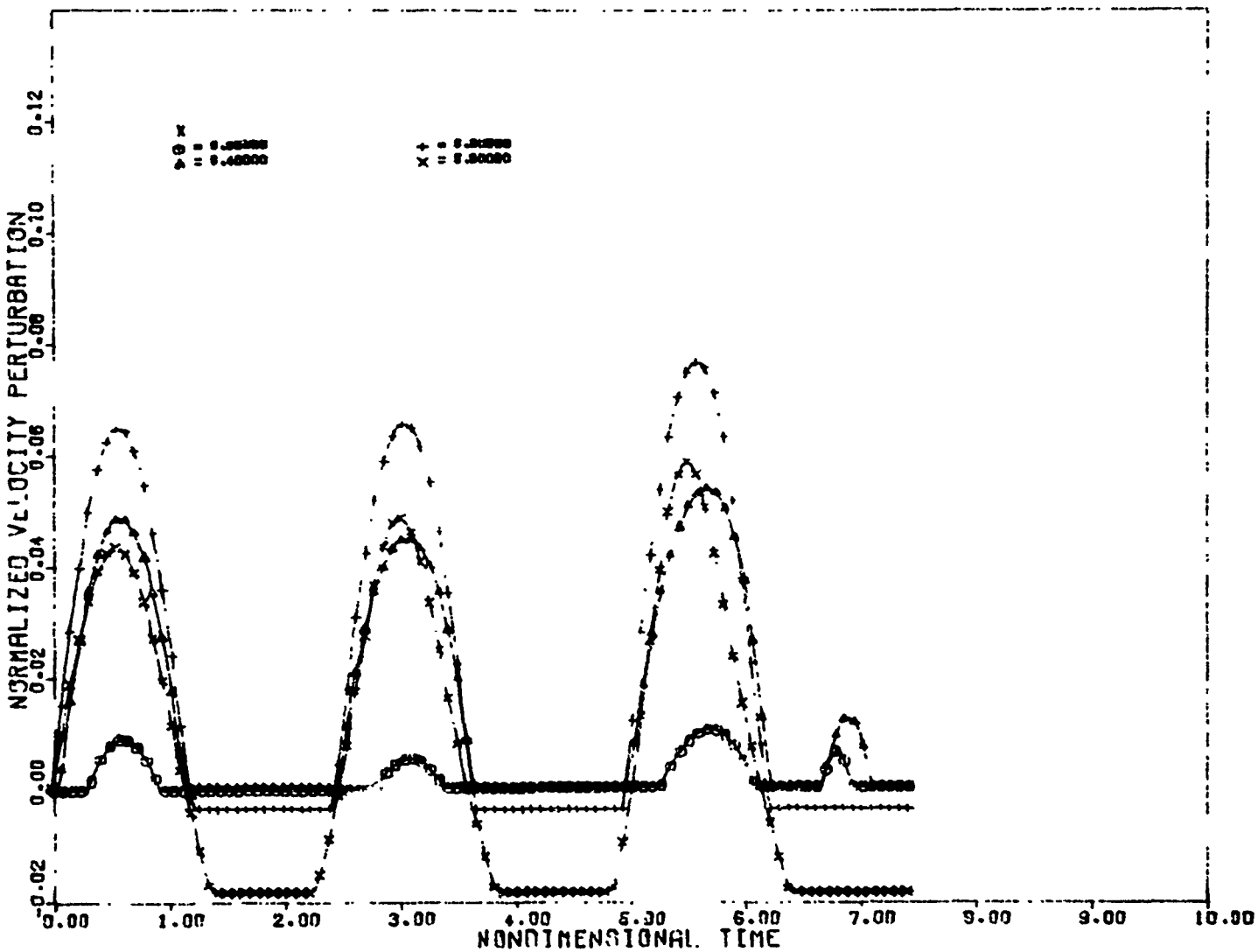

Figure 9-31. Velocity Perturbation History at Several Axial Locations, $u_{th} = .04$
$A = 11.5$, $B = .64$, $P_0' = .1 \cos(\pi x)$, 2_{11} Particles

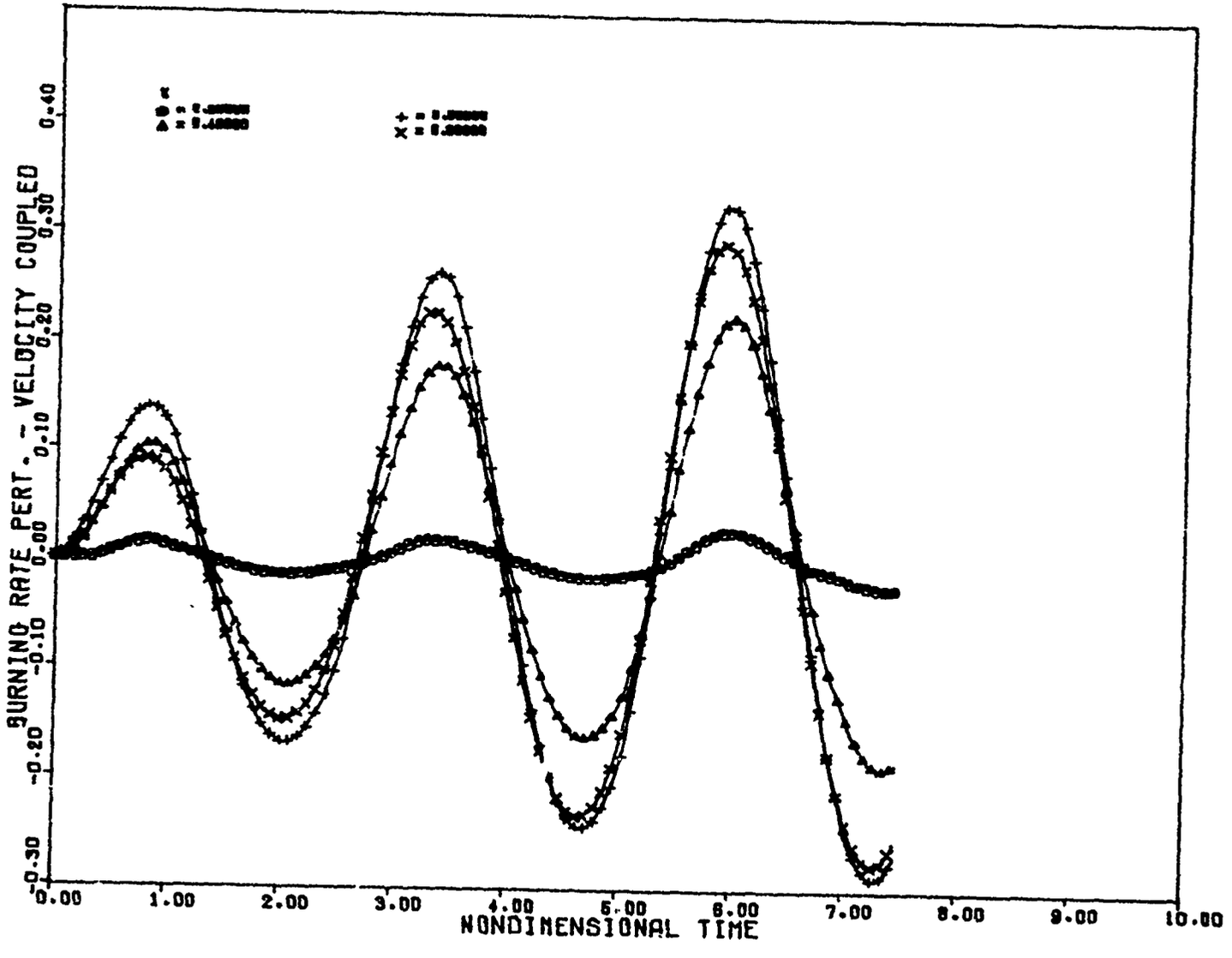

Figure 9-32. Velocity Coupled Burning Rate History at Several Axial Locations, $u_{th} = .04$
$A = 11.5$, $B = .64$, $P_0' = .1 \cos(\pi x)$, 2μ Particles

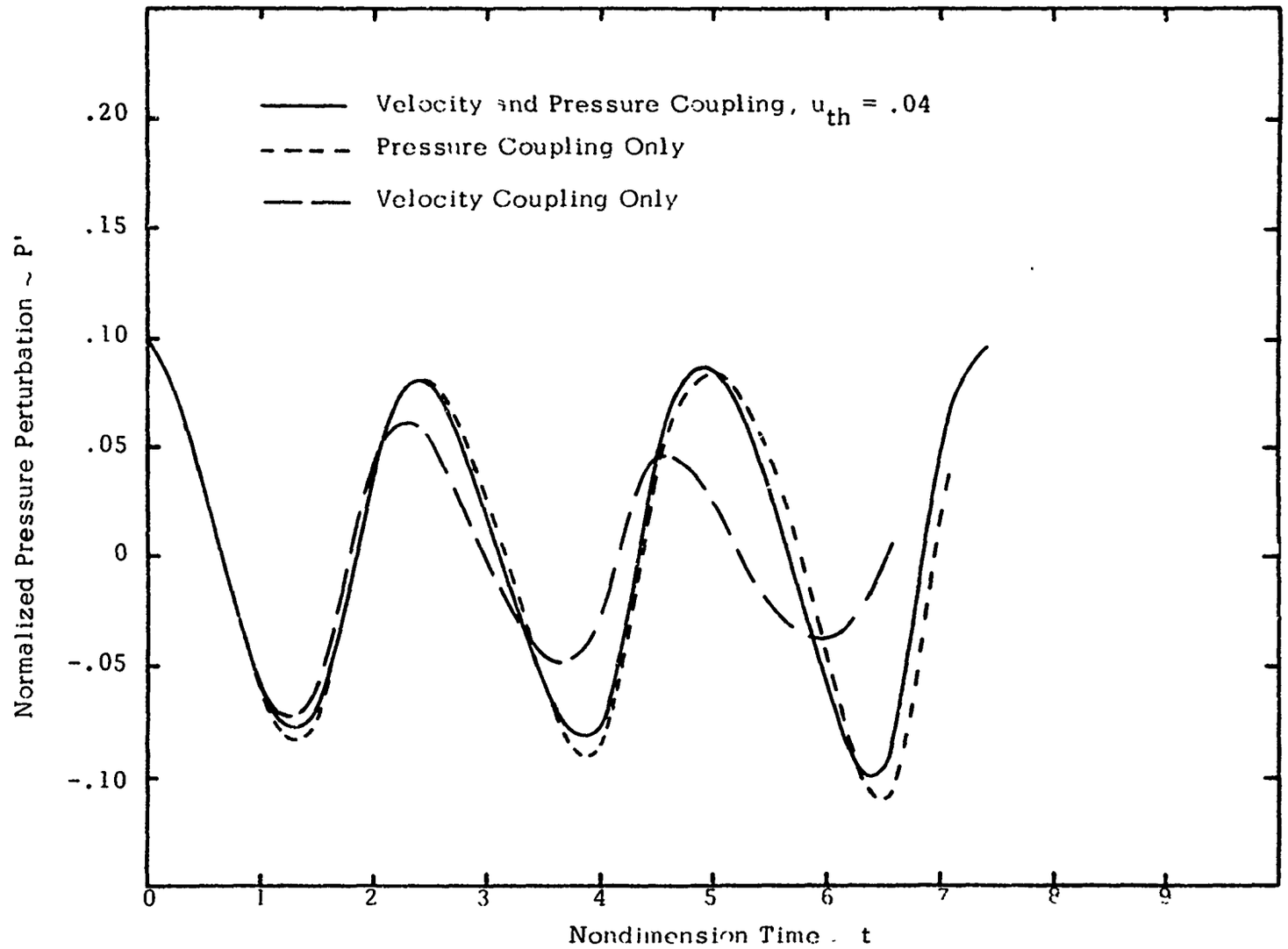

Figure 9-33. Effect of Coupling Mechanism on Pressure History at x = 0.
A = 11.5, B = .64, $P_0' = .1 \cos(\pi x)$, 2u Particles

10. SUMMARY, CONCLUSIONS AND RECOMMENDATIONS

10.1 Summary and Conclusions

After surveying the existing experimental and analytical solid rocket instability results, a new analytical instability model has been developed and solved. Unlike previous analytical solutions, the current longitudinal instability model is nonlinear and all of the various phenomena affecting the flow and stability of a motor can be treated in a coupled manner. (All of the possible flow and combustion processes are not yet included, but the model is general enough to allow for their future incorporation).

The two primary elements of the current instability analysis are a method of characteristics solution of the two phase flow in the combustion chamber of the motor, and a coupled calculation of a transient burning rate. The transient burning rate analysis presented, herein, is a unique and interesting development. It is based on an extension of the most popular, linear, harmonic combustion response model. The current method allows the calculation of propellant burning response to a pressure disturbance of arbitrary waveform, for all time, including the period immediately following the initiation of the disturbance. The analysis also includes a model for velocity coupled response. Therefore, for the first time, the nonlinear effects of velocity coupling on the growth of pressure waves in a combustion chamber can be computed.

The instability solution, itself, begins with the calculation of the steady state two-phase flow in the motor. The flow in the combustion chamber is calculated by numerically integrating the equations of motion, in conservative form. The nozzle flow and choked flow condition are found using the constant fractional lag approximation. The steady state conditions are then perturbed and the subsequent wave motion in the motor is calculated numerically, using the method of characteristics. The nature of the engine response is dependent upon the interaction the various gain and loss mechanisms in the engine; which are, in turn, a function of the propellant burning response, the size and amount of particulate matter present, the magnitude and shape of the initial disturbance and the geometrical configuration of the motor.

In order to proceed with the development and assessment of the current approach in the most rational manner, a number of simplifying assumptions were made. Only motors with cylindrically perforated grain were considered. The gasdynamic flow was assumed to be one-dimensional and the particles in the gas stream were taken to be of uniform size and inert; thereby ignoring the processes leading to the formation of the particulate matter. The nozzle flow was assumed to be quasi-steady.

A series of instability solutions have been calculated, wherein some of the main parameters such as particle size, burning rate constants, initial disturbance waveform and magnitude and type of response coupling have been varied, in an attempt to qualitatively assess the behavior and validity of the present model. The results obtained are quite encouraging. From all appearances, the qualitative behavior of the model is quite realistic and comparisons with one set of data tend to corroborate its efficacy.

When this effort was initiated it was hoped that it would lead to a greater understanding of longitudinal combustion instability, and, thereby to the realization of an improved predictive capability. It appears that these goals will be realized, since the limited number of instability solutions obtained to date have already provided some new insights, or confirmed what previously could only be hypothesized.

For instance, when test motors are pulsed, to initiate an instability, the initial disturbance is often observed to partially damp, before ultimately being amplified. Linear analysis cannot account for this behavior, however, as "necking" can, in all likelihood, be attributed to the existence of a time lag between the occurrence of a disturbance and the time at which the propellant burning rate can fully respond to it. During this initial period the surface combustion cannot supply energy to the wave at a rate fast enough to overcome the effect of the always present damping mechanisms. Given time, however, the propellant response builds up, in many cases, to the point where a net amount of energy is supplied to the wave, and it amplifies. The duration, or even existence, of such a response lag depends upon the values of the parameters appearing in the transient burning rate model. By varying these constants the initial response may be made to build up slowly, rapidly, or even overshoot, the response level it will attain at later times. Attempts to correlate the calculated and measured wave amplitudes immediately following pulsing should, therefore, provide some input towards the empirical

determination of the burning rate parameters. The selection of values for A and B, as these parameters are denoted, for quantitative use, must also be based on the ability of the calculated results to match measured growth rates and limiting amplitudes.

In many instances, experimental pressure traces, under unstable conditions, are observed to have relatively little harmonic content, even at relatively high amplitudes. This is in contrast to the results obtained for acoustic waves driven in closed resonant tubes, where significant wave steepening, and even weak shocks, are observed even at relatively low amplitudes. It has been felt that this difference in behavior must be attributable to some characteristic of the surface combustion response which allows the higher harmonics to be attenuated while simultaneously amplifying the primary acoustic mode. Such a cause and effect relationship has, however, never been previously demonstrated analytically. It was, therefore, quite gratifying to observe such an effect in the present instability solutions. The results presented earlier conclusively demonstrate that the current transient burning rate model is capable of producing a response which discriminates between the various harmonics contained in a general pressure wave; amplifying one, while attenuating several or all of the remaining harmonics. These results, therefore, appear to confirm the hypothesis that the low harmonic content exhibited by many instability traces is due to the attenuated response of the propellant to the higher frequency elements of a disturbance.

To date, instability solutions have not been continued out to a large number of cycles, therefore, the ability of the current model to predict a limiting amplitude has not been demonstrated. The present results do, however, exhibit a nonlinear feature which while not guaranteeing that a limiting smplitude will be reached, must be present if such limiting is to occur. Thei feature is the amplitude dependence of both of the gain and damping mechanisms.

It has also been concluded from the results that calculated particle damping effects do not appear to be sensitive to the exact form of the drag coefficient relationship. While based on only limited results, this circumstance, if corroborated by further study, is a welcome one, since

there is still some disagreement about the proper variation of C_D with Reynolds number.

10.2 Recommendations

Based on results achieved to date, the method of analyzing longitudinal combustion instability developed, herein, certainly merits further investigation; including quantitative comparison with experimental data. In order to achieve such quantitative agreement it may be necessary to eliminate some of the simplifying assumptions made during this initial effort. It may also be desirable to relax some of the other restrictions, currently imposed, in order to widen the applicability of the method. Some of the possible refinements or extensions of the present work are discussed below.

In order to fully assess the current instability model, or any further modifications to it, solutions must be carried out for many more cycles than have been computed to date. Only in this way can it be determined if the model is capable of predicting realistic growth rates and limiting amplitudes. When such solutions are sought, any improvements that could be made in computational efficiency would be quite significant from an economic standpoint. In this regard, it appears that replacement of the method of characteristics solution of the fluid dynamic equations of motion with a straight finite difference solution of the Lax-Wendroff type (see Ref. 68, for example) would be in order.

When the method of characteristics was selected as the numerical technique to be used in solving the flow equations, the nature of the transient burning rate analysis was, as yet, unknown. As it turned out, the need for pressure histories at fixed axial locations was satisfied by interpolation, and rectification of the characteristics mesh at every other time step. These steps could be eliminated if the computations were performed in a rectilinear mesh to begin with. The difference solution of the equations of motion is also somewhat simpler and more straightforward with the finite difference approach. It is estimated that a change to a Lax-Wendroff scheme of the type discussed in Reference 68 could reduce the computational time by 30% or more, from the current level of about 2 minutes per cycle (on a CDC 6600 computer).

The development of an alternative, or improved method for calculating transient burning response should also be considered, since the relatively large amount of computer storage currently required is not a desirable feature. Consideration should also be given to the development of a nonlinear transient response model for pressure coupling. Further investigation of the velocity coupling phenomena should also be considered, as the existing model may not prove to be adequate. A transient response model based on the nonlinear solution of the heat conduction equation may be able to provide a framework within which all of the aforementioned items can be accomplished.

It may also be possible to reduce the number of axial locations at which the transient burning response need be calculated. Currently, linear interpolation is used to calculate burning rate at locations between those at which it is directly computed. Replacing the linear interpolation with a higher order spline interpolation procedure should allow equivalent accuracy to be achieved with larger spacing between the locations at which transient burning response is calculated.

Other refinements, or extensions, that would be worthwhile, and not too difficult to incorporate into the solution are the ability to handle more complex motor geometries, and the adoption of a more realistic particle size distribution. The additional geometries that could still be considered on a one-dimensional basis include more general grain perforations, and motor cases having gaps in the grain, end grain, or a grain that does not extend the full length of the chamber. It would be possible to incorporate a particle size distribution function into the analysis, however, it is recommended that the next step in this direction should be the extension to two discrete particle sizes groups. Such an extension would be relatively simple, yet it would be a significant step towards realistically matching the bimodal type particle size distributions typically found in solid rocket motors.

The development of a model for metal particle formation and burning is not recommended at this time. The whole mechanism of particle formation is still subject to wide uncertainties, and the relative significance of particle burning as a determinant of motor stability has yet to be established. If these processes can be realistically modeled and are shown to be important, at some later time, there is no intrinsic reason why they cannot be incorporated into the instability model.

11. REFERENCES

1. Saenger, R. A., and Hudson, G. E., "Periodic Shock Waves in Resonating Gas Columns," J. Acoust. Soc. of America, V. 32, No. 8 (Aug. 1960).

2. Betchov, R., "Nonlinear Oscillations of a Column of Gas," Physics of Fluids, V. 1, No. 3 (May-June, 1958) pp. 205-212.

3. Chester, W., "Resonant Oscillations in Closed Tubes," J. Fluid Mechanics, V. 18, Part 1 (1964) pp. 44-64.

4. Coppens, A. B., and Sanders, J. V., "Finite-Amplitude Standing Waves in Rigid-Walled Tubes," J. Acoust. Soc. of Am. V. 43, No. 3 (Mar. 1968) pp. 516-529.

5. Weiss, N. O., "The Development of a Shock From Standing Waves of Finite Amplitude in an Isentropic Fluid," Proc. Comb. Phil. Soc. V. 60 (1964) pp. 129-135.

6. Fowler, J. R. and Rosenthal, J. S., "Missile Vibration Environment for Solid Propellant Oscillatory Burning," AIAA Paper 71-756 (June 1971).

7. Bergman, G. H. and Jessen, E. C., "Evaluation of Conventional Rocket Motor Instrumentation for Analysis of Oscillatory Combustion," AIAA Paper 71-755 (June 1971).

8. Browning, S. C., Kraskin, M., and Thacker, J. H., "Application of Combustion Instability Technology to Solid-Propellant Motor Problems," AIAA Paper 71-758.

9. Dickinson, L. A., Brownlee, W. G., and Jackson, F., "CARDE Investigations of Finite Wave Axial Combustion Instability," Canadian Armament Research and Development Establishment, Valcartier, Quebec, Canada CARDE T. N. 1959/62 (1962).

10. Brownlee, W. G., "Nonlinear Axial Combustion Instability in Solid Propellant Motors," AIAA J. V. 2, No. 2 (Feb. 1964) pp. 205-284.

11. Brownlee, W. G., and Roberts, A. K., "Investigations of Nonlinear Axial Combustion Instability in Solid Propellant Rocket Motors," CARDE T.R. 474/64 (June 1964).

12. Brownlee, W. G., and Roberts, A. K., "Investigations of Nonlinear Axial Combustion Instability in Solid Propellant Rocket Motors," AIAA Paper 63-474 (Oct. 1963).

13. Brownlee, W. G., and Kimbell, G. H., "Shock Propagation in Solid-Propellant Rocket Combustors," AIAA J. V. 4, No. 6 (June 1966) pp. 1332-34.

14. Roberts, A. K., Bergman, W. A., and Brownlee, W. G., "Longitudinal Combustion Instability: Behavior of Propellants with High Solids Content," CARDE T.N. 1746/67 (Mar. 1967).

15. Kimbell, G. H., and Brownlee, W. G., "Flow Processes in a Solid Propellant Combustor During Unstable Combustion," CARDE T.N. 1783/68 (Mar. 1968).

16. Kimbell, G. H., and Brownlee, W. G., "Status Report on Optical Studies of Combustion Instability at CARDE", CARDE T.N. 1784/68 (Mar. 1968).

17. Roberts, A. K., Brownlee, W. G., and Jackson, F., "Combustion Instability and the Design of Solid Propellant Rocket Motors," Canadian Aeronautics and Space Journal, V. 16, No. 1 (Jan. 1970) pp. 21-27.

18. Roberts, A. K., and Brownlee, W. G., "Nonlinear Longitudinal Combustion Instability: Influence of Propellant Composition," AIAA J. V. 9, No. 1 (Jan. 1971) pp. 140-147.

19. Dickinson, L. A., "Command Initiation of Finite Wave Axial Combustion Instability in Solid Propellant Rocket Motors," ARS J. V. 32 (April 1962) pp. 643-644.

20. Dickinson, L. A., and Jackson, F., "Combustion in Solid Propellant Rocket Engines," 5th AGARD Colloquium on Combustion and Propulsion (The Macmillan Co., N. Y.,1963) pp. 531-550.

21. Capener, E. L., Dickinson, L. A., and Kier, R. J., "Driving Processes of Finite Amplitude Axial Mode Instability in Solid-Propellant Rockets," AIAA J. V. 5, No. 5.

22. Marxman, G. A., and Wooldridge, C. E., "Finite-Amplitude Axial Instability in Solid-Rocket Combustion" Twelfth Symposium (International) on Combustion (The Combustion Institute, Pittsburgh, Pa., 1969) pp. 115-127.

23. Micheli, P. L., Private Communication.

24. Price, E. W., "Axial Mode, Intermediate Frequency Combustion Instability in Solid Propellant Rocket Motors," AIAA Preprint No. 64-146 (Jan. 1964).

25. Angelus, T. A., "Unstable Burning Phenomenon in Double-Base Propellants," Progress in Astronautics and Rocketry, V. 1, Solid Propellant Rocket Research (Academic Press, 1960) pp. 527-559.

26. Watermeier, L. A., Aungst, W. P., and Pfaff, S. P., "An Experimental Study of the Aluminum Additive Role in Unstable Combustion of Solid Rocket Propellants," Ninth Symposium (International) on Combustion (1963) pp. 316-325.

27. Hart., R. W., Bird, J. F., and McClure, F. T., "The Influence of Erosive Burning on Acoustic Instability in Solid Propellant Rocket Motors," Progress in Astronautics and Rocketry, V. 1, Solid Propellant Rocket Research (Academic Press, N. Y., 1960) pp. 423-499.

28. McClure, F. T., Bird, J. R., and Hart, R. W., "Erosive Mechanism for Nonlinear Instability in the Axial Mode of Solid Propellant Rocket Motors," ARS J., V. 32, No. 3 (Mar 1962) pp. 374-378.

29. Bird, J. F., Hart, R. W., and McClure, F. T., "Finite Acoustic Oscillations and Erosive Burning in Solid Fuel Rockets," AIAA J., V. 3, No. 12 (Dec. 1965) pp. 2248-2256.

30. Price, E. W., and Dehority, G. L., "Velocity Coupled Axial Mode Combustion Instability in Solid Propellant Rocket Motors," Proceedings of the 2nd ICRPG/AIAA Solid Propulsion Meeting, Anaheim, California (1967) pp. 213-227.

31. Culick, F. E. C., "Stability of Longitudinal Oscillations With Pressure and Velocity Coupling in a Solid Propellant Rocket," Combustion Science and Technology, V. 2, No. 4 (1970), pp. 179-201.

32. Sirignano, W. A., and Crocco. L., "A Shock Wave Model of Unstable Rocket Combustors," AIAA J. Vo. 2, No. 7 (July 1964) pp. 1285-1296.

33. Mitchell, C. E., Crocco, L., and Sirignano, W. A., "Nonlinear Longitudinal Instability in Rocket Motors with Concentrated Combustion," Combustion Science and Technology, V. 1, No. 1 (July 1969) pp. 35-64.

34. Crocco, L., and Mitchell, C. E., "Nonlinear Periodic Oscillations in Rocket Motors with Distributed Combustion," Combustion Science and Technology, V. 1, No. 2 (Sept. 1969) pp. 147-169.

35. Sirignano, W. A., "A Theory of Axial-Mode Shock-Wave Oscillations in a Solid-Rocket Combustor," Twelfth Symposium (International) on Combustion (The Combustion Institute, Pittsburgh, Pa., 1969) pp. 129-137.

36. Powell, E.A., and Zinn, B. T., "A Single Mode Approximation in the Solution of Nonlinear Combustion Instability Problems," AIAA preprint 71-208 (Jan. 1971).

37. Powell, E. A., "Nonlinear Combustion Instability in Liquid Propellant Rocket Engines," Georgia Institute of Technology, Report GITAER 70-6 (1970).

38. Culick, F. E. C., "Nonlinear Growth and Limiting Amplitude of Acoustic Oscillations in Combustion Chambers," Combustion Science and Technology, V. 3 (1971) pp. 1-16.

39. Culick, F. E. C., "Nonlinear Behavior of Acoustic Waves in Combustion Chambers," Work in progress, supported by Hercules, Inc.

40. Priem, R. J., and Guentert, D. C., "Combustion Instability Limits Determined by a Nonlinear Theory and a One-Dimensional Model," NASA TND-1409 (1962).

41. Weiss, R. R., and Osborn, J. R., "Combustion Characteristics of Bi-Phase Rockets," AFOSR 70-0768 TR (1970).

42. Hoffman, R. J., Beltran, M. R., Breen, B. P., and Wright, R. D., "Extension of the Priem-Guentert Annular Combustion Instability Model to a Bipropellant System," 3rd ICRPG Combustion Conference, CPIA Publ. No. 138 (1967).

43. Beltran, M. R., et al, "Liquid Rocket Engine Combustion Instability Studies," Dynamic Science Final Report AFRPL-TR-66-25 (1966).

44. Beltran, M. R., Breen, B. P., and Gerstein, M., "Liquid Rocket Combustion Instability Studies," Dynamic Science Final Report No. SN-68-S1 (1965).

45. Priem, R. J., and Heidmann, M. F., "Propellant Vaporization as a Design Criteria for Rocket-Engine Combustion Chambers," NASA TR R-67 (1960).

46. Hoffman, R. J., Wright, R. O., and Breen, B. P., "Combustion Instability Prediction Using a Nonlinear Bipropellant Vaporization Model," NASA CR-920 (1968).

47. Campbell, D. T., and Chadwick, W. D., "Combustion Instability Analysis at High Chamber Pressures," AFRPL-TR-67-222, Rocketdyne, a Division of North American Rockwell Corporation, Canoga Park, Calif. (1967).

48. Berstein, S. Z., and Schechter, H., "Study of High Frequency Nonlinear Combustion Instability with Baffled Annular Liquid Propellant Rocket Motors," Final Report MR-7009 (1970).

49. Agosta, V. D., "Nonlinear Combustion Instability: Longitudinal Mode," 6th ICRPG Combustion Conference, CPIA Publ. No. 192 (1969).

50. Seamans, T. F., Vanipie, M., and Agosta, V. D., "A Fundamental Model of Hypergolic Ignition in Space Ambient Engines," AIAA J., 5, pp. 1216 (1967).

51. Zinn, B. T., "A Theoretical Study of Nonlinear Traverse Combustion Instability in Liquid Propellant Rocket Motors," Princeton University AMS Tech. Report No. 732 (1966).

52. Culick, F. E. C., "Interactions Between the Flow Field, Combustion, and Wave Motions in Rocket Motors," To be published, Naval Weapons Center, China Lake, Calif. (1972).

53. Dobbins, R. A., and Temkin, S., "Attenuation and Dispersion of Sound by Particulate-Relaxation Processes," J. Acoust. Soc. of Am., V. 40, No. 2 (Feb. 1966) pp. 317-324.

54. Dehority, G. L., "A Parametric Study of Particulate Damping Based on The Model of Temkin and Dobbins Naval Weapons Center, China Lake, California NWC TP5002 Sept. 1970.

55. Friedly, J. C., and Peterson, E. E., "Influence of Combustion Parameters on Instability in Solid Propellant Motors. Part II, Nonlinear Analysis," AIAA J. V. 4, No. 11 (Nov. 1966) pp. 1932-1937.

56. Brown, R. H., and Muzzy, R. J., "Linear and Nonlinear Pressure Coupled Combustion Instability of Solid Propellants," AIAA J. V. 8, No. 8 (August 1970) pp. 1492-1500.

57. Novozhilov, B. V.,"Nonlinear Oscillations of Combustion Velocity of Powder," Soviet Journal of Applied Mechanics and Technical Physics, V. 7, No. 5, (May 1966) pp. 31-41.

58. Krier, H., et al, "Nonsteady Burning Phenomenon of Solid Propellants: Theory and Experiment," AIAA J. V. 6, No. 2 (Feb. 1968) pp. 278-285.

59. Culick, F. E. C., "A Review of Calculations for the Unsteady Burning of a Solid Propellant," AIAA J.,V. 6, No. 12 (Dec. 1968) pp. 2241-2255.

60. Culick, F. E. C., "Some Problems in the Unsteady Burning of Solid Propellants," Naval Weapons Center, China Lake, California, NWC TP 4668 (Feb. 1969).

61. Price, E. W. "Comments on Role of Aluminum in Suppressing Instability in Solid Propellant Rocket Motors", AIAA J., Vol. 9, No. 5, (May 1971), pp. 987-990.

62. Marble, F. E., "Dynamics of Dusty Gases" Annual Review of Fluid Mechanics, Vol. 2, pp. 397-446 (1970).

63. Rudinger, G., "Effective Drag Coefficients for Gas-Particle Flow In Shock Tubes" Project Squid Technical Report CAL-07-PU, March 1969.

64. Carlson, D. J. and Hoglund, R. F., "Particle Drag and Heat Transfer in Rocket Nozzles," AIAA J., Vol. 2, Nov. 1964, pp. 1980-84.

65. Kliegel, J. R. "Gas Particle Nozzle Flows" Ninth International Symposium on Combustion, The Combustion Institute, Pittsburg, Pa. pp. 811-826 (1963).

66. Kliegel, J.R., "One Dimensional Flow of a Gas Particle System, Paper No. 60-S, IAS 28th Meeting, New York, January 1960.

67. Frey, H.M., Nickerson, G.R. and Tyson, T.J., "One Dimensional Kinetic Nozzle Analysis Reference Computer Program, Dynamic Science Report No. CS-1-9/70, September 1970.

68. Rubin, E.L., and Burstein, S.Z. Journal of Computational Physics, Vol. 2, (1967), pp. 178-96.

69. Korman, H.F., "An Analysis of Nonlinear Particle Damping". unpublished.

70. Abramowitz, M., and Stegun, I.A., (Editors). Handbook of Mathematical Functions with Formulas Graphs, and Mathematical Tables, Dover Publications, Inc.

APPENDIX A

THE TRANSIENT BURNING RESPONSE--SOME SPECIAL CASES

The final form of the current transient burning rate model (Equation (4-65), or the approximation to it, Equation (4-68)) is not an explicit formula for $m'/\bar{m}$, and is not very useful for formal analysis. For example, it is not possible to deduce from (4-65) closed form results for the transient burning rate behavior at all times $\tau > 0$. It is relatively easy, however, to obtain short time approximations and the long time steady-state behavior, valid after all initial transients have died out. This latter property may be used to advantage by comparing the long time "steady-state" results obtained from Equation (4-65) to the known response for two special cases. Such a comparison serves as, at least, a partial consistency check on the current formulation.

1. <u>Response to a Harmonic Pressure Oscillation for $\tau \to \infty$</u>

For this case,

$$\frac{p'}{\bar{p}}(\tau) = e^{i\omega t} = e^{4i\Omega\tau} \tag{A-1}$$

After a long time, the fluctuation of mass flux also varies harmonically, but with phase shift Φ, and amplitude $|R_b|$

$$\frac{m'}{\bar{m}}(\tau) = |R_b|\, e^{i(4\Omega\tau + \varphi)} \tag{A-2}$$

Substitution of (A-1) and (A-2) into (4-65) should lead to the result that $|R_b| \exp(i\varphi)$ is the original response function R_b given by (4-34) with

$n_w = 0$. After the substitution, one has

$$|R_b| e^{i\varphi} = |R_b| e^{i} \left[\frac{\sigma_1 + \sigma_2}{\sqrt{\pi}} \int_0^{\tau} e^{-p\xi} \frac{d\xi}{\sqrt{\xi}} - \sigma_1 \sigma_2 e^{-p\tau} \int_0^{\tau} e^{p\xi} d\xi \right]$$

$$+ 2nAB \left[\frac{1}{\sqrt{\pi}} \int_0^{\tau} e^{-p\xi} \frac{d\xi}{\sqrt{\xi}} + e^{-p\tau} \int_0^{\tau} e^{p\xi} d\xi \right] \tag{A-3}$$

The integrals may be simply evaluated, in the limit as $\tau \to \infty$, as follows:

$$\frac{1}{\sqrt{\pi}} \int_0^{\tau} e^{-p\xi} \frac{d\xi}{\sqrt{\xi}} = \frac{1}{\sqrt{p}} \frac{2}{\sqrt{\pi}} \int_0^{\sqrt{p\tau}} e^{-\zeta^2} d\zeta \underset{\tau \to \infty}{=} \frac{1}{\sqrt{p}}$$

$$e^{-p\tau} \int_0^{\tau} e^{p\xi} d\xi = \frac{1}{p} \left[1 - e^{-p\tau} \right] \underset{\tau \to \infty}{=} \frac{1}{p} \tag{A-4}$$

where $p = 1 + i4\Omega$. With the result (A-4) Equation (A-3) becomes

$$|R_b| e^{i\varphi} = |R_b| e^{i\varphi} \left[\frac{\sigma_1 + \sigma_2}{\sqrt{p}} - \frac{\sigma_1 \sigma_2}{p} \right] + 2nAB \left(\frac{1}{\sqrt{p}} + \frac{1}{p} \right)$$

which can be solved and rearranged to give

$$|R_b| e^{i\varphi} = 2nAB \frac{1 + \sqrt{p}}{p - (\sigma_1 + \sigma_2)\sqrt{p} + \sigma_1 \sigma_2}$$

$$= 2nAB \frac{1 + \sqrt{p}}{(\sqrt{p} - \sigma_1)(\sqrt{p} - \sigma_2)} \tag{A-5}$$

as required.

2. Response to a Step Change of Pressure for $\tau \to \infty$

Now set

$$\frac{p'}{\bar{p}} = \Delta \quad (\tau > 0) \tag{A-6}$$

After a long time, $m'/\bar{m}$ should approach a constant μ, equal to $n\Delta$. As above, the contributions for τ small, from $m'/\bar{m}$ different from μ, are supposed negligible. Hence, (4-65) becomes

$$\mu = \mu \left\{ \frac{\sigma_1 + \sigma_2}{\sqrt{\pi}} \int_0^\tau e^{-\xi} \frac{d\xi}{\sqrt{\xi}} - \sigma_1 \sigma_2 e^{-\tau} \int_0^\tau e^{\xi} d\xi \right\}$$

$$+ 2nAB \left\{ \frac{\Delta}{\sqrt{\pi}} \int_0^\tau e^{-\xi} \frac{d\xi}{\sqrt{\xi}} + e^{-\tau} \int_0^\tau e^{\xi} d\xi \right\} \tag{A-7}$$

By a simple transformation,

$$\frac{1}{\sqrt{\pi}} \int_0^\tau e^{-\xi} \frac{d\xi}{\sqrt{\xi}} = \operatorname{erf}(\sqrt{\tau}) \underset{\tau = \infty}{\to} 1 \tag{A-8}$$

and (A-7) becomes, for large τ:

$$\mu = \mu \left\{ \sigma_1 + \sigma_2 - \sigma_1 \sigma_2 \right\} + 4nAB\Delta \tag{A-9}$$

From the definitions (4-62), it follows that

$$\sigma_1 + \sigma_2 - \sigma_1 \sigma_2 = 1 - 4AB$$

and

$$\mu = \mu (1 - 4AB) + 4nAB\Delta \tag{A-10}$$

which produces the correct result, $\mu = n\Delta$.

3. Exact Solution of Equation (4-61) for Step and Exponential Changes of Pressure

In addition to checking that the numerical solution for the transient burning rate approached the proper long time limits, indicated in Sections A.1 and A.2 above, for harmonic and step pressure disturbances, a further accuracy check has been made. The numerical results have been compared with exact results deduced from Equation (4-61), for the response to step and exponential changes of pressure. All of these comparisons corroborated the numerical calculations. Exact solutions for step and exponential pressure changes may be found as follows.

An exponential pressure change which approaches the finite value Δ for long times is represented by

$$\frac{p'}{\bar{p}} = \Delta(1-e^{-\beta\tau}) \tag{A-11}$$

The Laplace transform in the variable p is

$$\begin{aligned} \frac{p'}{\bar{p}}(p) &= \int_0^\infty 4e^{\tau}\,\Delta(1-e^{\beta\tau})\,e^{-p\tau}\,d\tau \\ &= \frac{4\Delta}{p-1} - \frac{4\Delta}{p-\sigma_3^2} \end{aligned} \tag{A-12}$$

where

$$\sigma_3^2 = 1-\beta \tag{A-13}$$

Equation (4-61) becomes

$$\frac{1}{2nAB\Delta}\left[e^{\tau}\frac{m'}{\bar{m}}(\tau)\right] = \frac{1}{2\pi i}\int \frac{1+\sqrt{p}}{(\sqrt{p}-\sigma_1)(\sqrt{p}-\sigma_2)}\left[\frac{1}{p-1} - \frac{1}{p-\sigma_3^2}\right]e^{p\tau}\,dp$$

Inversion is accomplished by using standard tables, after the integrand has been expanded in partial fractions. The result is

$$\frac{1}{2nAB\Delta}\ \frac{m'}{\bar{m}}(\tau) = (D_1 - C_1)\sigma_1 e^{(\sigma_1^2 - 1)\tau}\ \mathrm{erfc}(-\sigma_1\sqrt{\tau})$$

$$+ (D_2 - C_2)\sigma_2 e^{(\sigma_2^2 - 1)}\ \mathrm{erfc}(-\sigma_2\sqrt{\tau})$$

$$+ D_3\ \mathrm{erfc}(-\sqrt{\tau}) \qquad \text{(A-14)}$$

$$- \sigma_3 C_3 e^{(\sigma_3^2 - 1)\tau}\ \mathrm{erfc}(-\sigma_3\sqrt{\tau})$$

$$+ \sigma_3 C_4 e^{(\sigma_3^2 - 1)\tau}\ \mathrm{erfc}(\sigma_3\sqrt{\tau}$$

where $\sigma_3 = \sqrt{1-\beta}$ and the constants are:

$$C_1 = \frac{1+\sigma_1}{(\sigma_1-\sigma_2)(\sigma_1^2-\sigma_3^2)} \qquad D_2 = \frac{1}{(\sigma_2-\sigma_1)(\sigma_2-1)}$$

$$C_2 = \frac{1+\sigma_2}{(\sigma_2-\sigma_1)(\sigma_2^2-\sigma_3^2)} \qquad D_3 = \frac{1}{(1-\sigma_1)(1-\sigma_2)} = \frac{1}{4AB}$$

$$C_3 = \frac{1+\sigma_3}{2\sigma_3(\sigma_3-\sigma_2)(\sigma_3-\sigma_1)} \qquad \text{(A-15)}$$

$$C_4 = \frac{-(1-\sigma_3)}{2\sigma_3(\sigma_3+\sigma_1)(\sigma_3+\sigma_2)}$$

$$D_1 = \frac{1}{(\sigma_1-\sigma_2)(\sigma_1-1)}$$

These constants have the following useful properties which can be verified by direct computation.

$$\sum_{i=1}^{4} C_i = 0 \qquad \sum_{i=1}^{3} D_i = 0$$

$$\sum_{i=1}^{4} \sigma_i C_i = 0 \qquad \sum_{i=1}^{3} \sigma_i D_i = 0 \tag{A-16}$$

$$\sum_{i=1}^{4} \sigma_i^2 C_i = 1 \qquad \sum_{i=1}^{3} \sigma_i^2 D_i = 1$$

Also, C_2 is the complex conjugate of C_1 and D_2 is the complex conjugate of D_1.

The exact solution for a step change in pressure may be simply obtained from Equation (A-14) by setting C_1, C_2, C_3 and C_4 all equal to zero. Equation (A-14) is not in the form best suited to obtaining numerical values for m'/m, for, while all of the quantities on the r.h.s. of the equation are complex numbers, $m'/\bar{m}$ is real.

The real form of $m'/\bar{m}$ may be found as follows. The definitions given by Equation (4-62) are written as

$$\sigma_1 = x + iy$$

$$\sigma_2 = x - iy \tag{A-17}$$

and the following identities are used :

$$\mathrm{erfc}(-z) = 1 - \mathrm{erfc}(-z) = 1 + \mathrm{erf}(z) \tag{A-18}$$

The error function, itself, can be expressed in series form as

$$\mathrm{erf}(z) = \frac{2}{\sqrt{\pi}} \sum_{n=0}^{\infty} \frac{(-1)^n z^{2n+1}}{n!(2n+1)} \tag{A-19}$$

Using Equations (A-17 to A-19), Equation (A-14), with the $C_i = 0$, can then be expressed, after much algebra, as

$$\frac{1}{2nAB\Delta}\,\frac{m'}{\bar{m}} = 2R + \frac{1}{4AB}\left[1 + \frac{2}{\sqrt{\pi}}\sum_{n=0}^{\infty}\frac{(-1)^n\,\tau^{(n+\frac{1}{2})}}{n!(2n+1)}\right] \tag{A-20}$$

$$+\frac{4}{\sqrt{\pi}}\sum_{n=0}^{\infty}\frac{(-1)^n}{n!(2n+1)}\,r^{(2n+1)}\left[R\cos(2n+1)\theta - S\sin(2n+1)\theta\right]$$

where;

$$R = -e^{u\tau}(\zeta\cos v\tau - \eta\sin v\tau)$$

$$S = -e^{u\tau}(\eta\cos v\tau + \zeta\sin v\tau)$$

$$u = x^2 - y^2 - 1$$

$$v = 2xy$$

$$\zeta = \alpha x - \beta y = \frac{1}{8AB} = \alpha \tag{A-21}$$

$$\eta = \beta x + \alpha y$$

$$\alpha = \frac{1}{8AB}$$

$$\beta = \frac{(x-1)}{8yAB}$$

$$r = [(x^2+y^2)]^{\frac{1}{2}} = (\tau c_1\sigma_2)^{\frac{1}{2}}$$

$$\theta = \tan^{-1} y/x$$

The real part of Equation (A-14) with the $C_i \neq 0$ (corresponding to the solution for an exponential pressure change) may be established in a similar manner.

4. Transient Response to Harmonic Pressure Disturbances

The value of the response function obtained from Equation (4-34) actually corresponds to that which would be attained after many cycles of a harmonic disturbance. During the period immediately following the initiation of a disturbance the value of the response function may be quite different as a result of transient phenomena. The portion of the response resulting from the start up process following initiation of the disturbance damps out exponentially, and the limiting value given by Equation (4-34) is asymptotically approached as time increases. The number of wave cycles required for these initial transients to damp out in response to a harmonic disturbance varies quite significantly as a function of A and B. The response may also initially overshoot, or undershoot, the asymptotic value.

Examples of the transient burning rate response to a pressure disturbance of the form $\Delta P = .1 \cos \pi t$ are presented in Figures A-1 to A-3, for three sets of A and B values:

A = 15,	B = .7
A = 11.5	B = .64
A = 20	B = .9

These examples illustrate the significant effect of A and B on the initial characteristics of the response, as well as the effect on the ultimate magnitude of the response function.

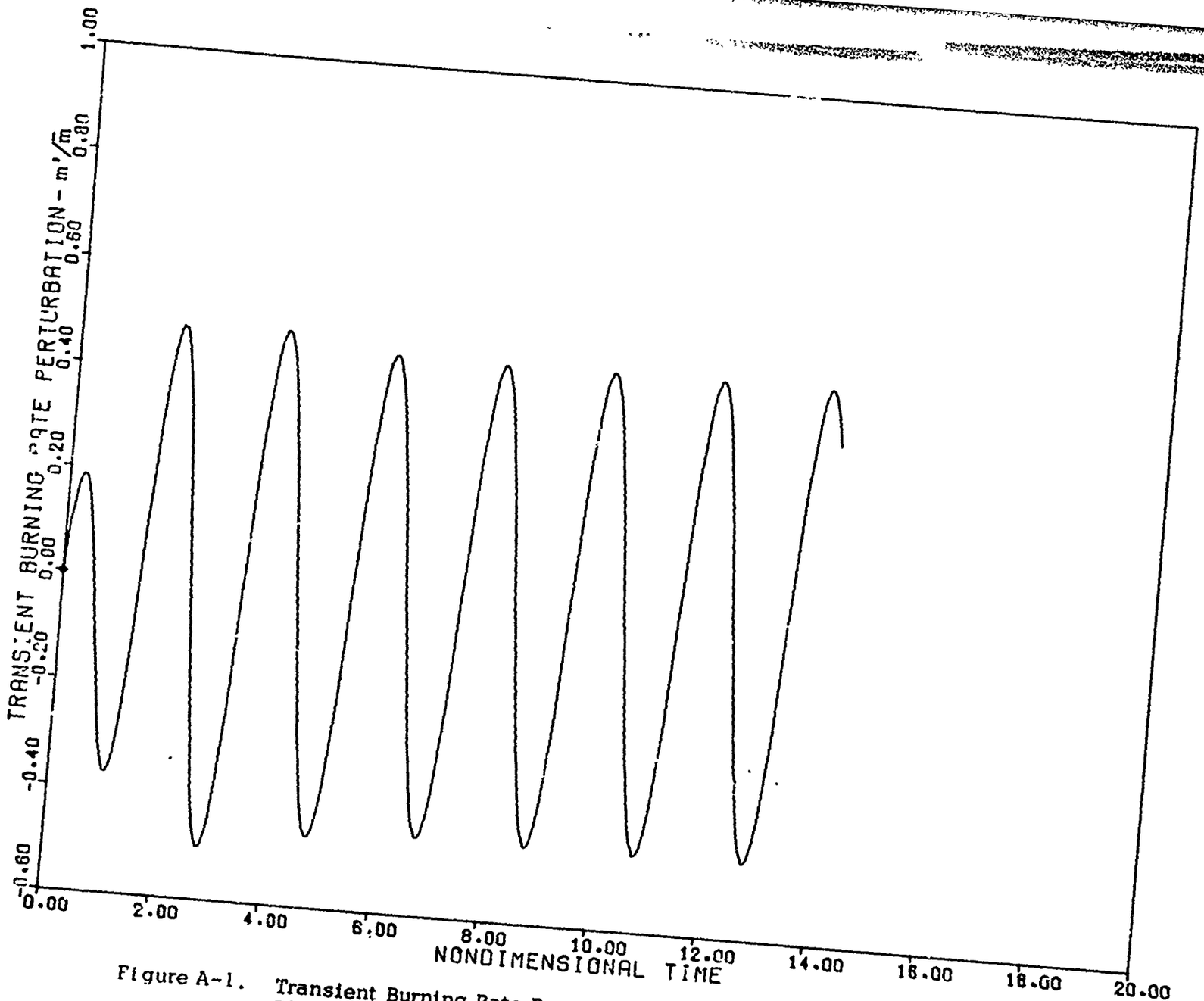

Figure A-1. Transient Burning Rate Response
$P' = .1 \cos(\pi t)$ A = 15, B = .7

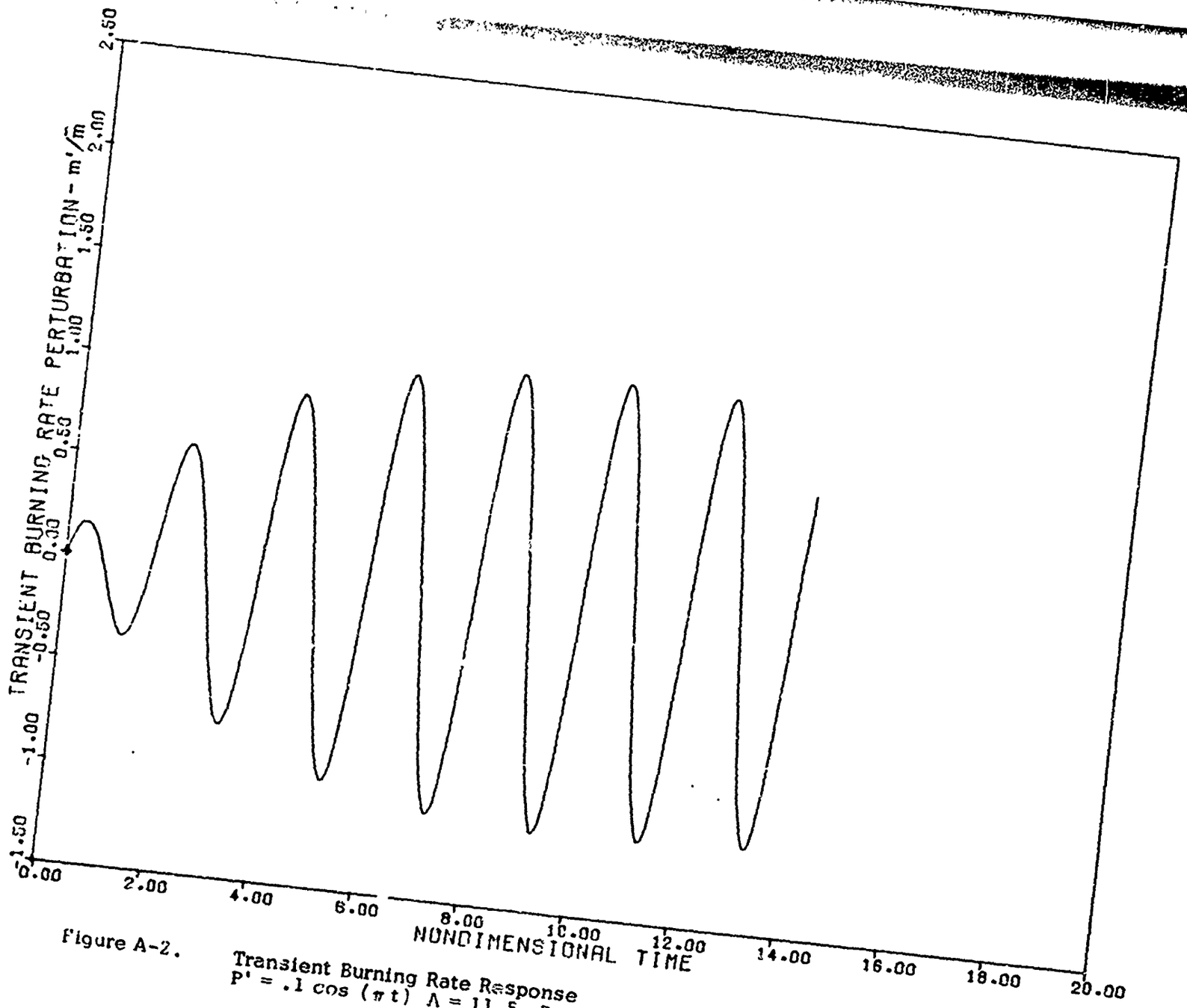

Figure A-2. Transient Burning Rate Response
$P' = .1 \cos(\pi t)$ $A = 11.5$, $B = .64$

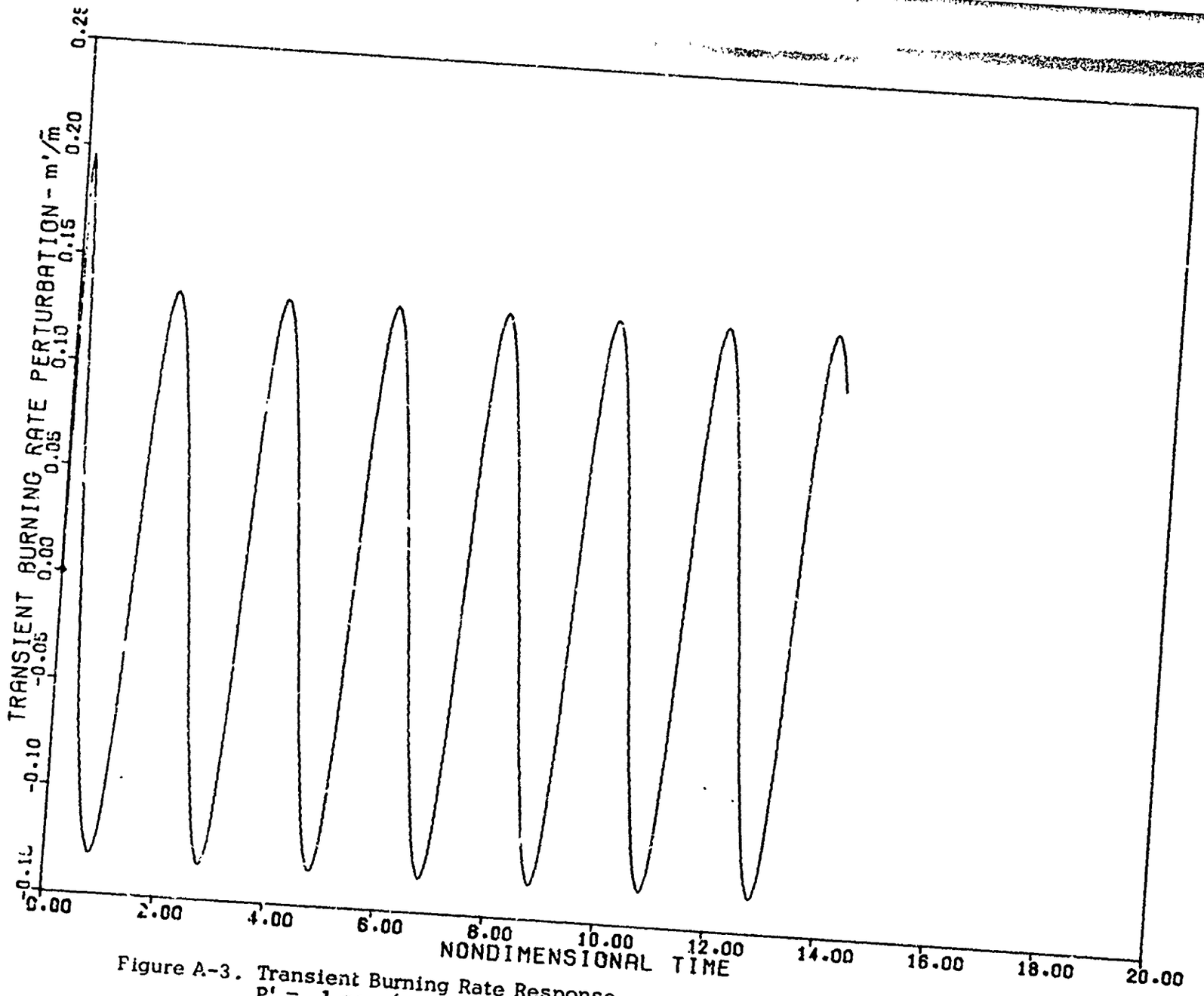

Figure A-3. Transient Burning Rate Response
$P' = .1 \cos(\pi t)$ $A = 20$, $B = .9$